2009-12-30

Equalization of Loudspeakers and Enclosed Sound Fields

Xi Chen
Brigham Young University - Provo

Equalization of Loudspeakers and Enclosed Sound Fields

Xi Chen

A dissertation submitted to the faculty of
Brigham Young University
in partial fulfillment of the requirements for the degree of

Doctor of Philosophy

Timothy W. Leishman
Scott D. Sommerfeldt
Jonathan D. Blotter
Kent L. Gee
David G. Long

Department of Physics and Astronomy

Brigham Young University

December 2009

ABSTRACT

Equalization of Loudspeakers and Enclosed Sound Fields

Xi Chen

Department of Physics and Astronomy
Doctor of Philosophy

Equalization of loudspeakers and enclosed sound fields has been a topic of considerable interest for decades. Confusion has often arisen among audio professionals regarding the feasibility of simultaneously equalizing a loudspeaker and the enclosed field (i.e., the "room") it excites. Because of frustrations encountered in such efforts, some have advocated abandoning simultaneous equalization altogether. This dissertation discusses the drawbacks of this approach as well as traditional in situ equalization methods. It demonstrates that many problems with traditional equalization stem from the use of measured acoustic pressure at a discrete point in a sound field as the system output. The dissertation presents analytical models and experiments involving the equalization of loudspeakers and both one-dimensional and three-dimensional sound fields. Equalization using total energy density at a point in either a one-dimensional or three-dimensional field produces better global equalization of the pressure field. In the one-dimensional case, it allows simultaneous correction of spectral loudspeaker and global sound-field response anomalies in a nearly optimal sense.

ACKNOWLEDGEMENTS

I express my immense gratitude to my research advisor Dr. Timothy W. Leishman for his guidance and patience through the span of this research work. His work ethic and strong sense of responsibility have left an influence upon me far beyond the academic field. I cannot enumerate the countless hours he spent with me in the research lab checking details of the procedures. Also being a wonderful lecturer, he truly taught me how to incorporate the knowledge gained from the text book into the research experience.

I would like to thank my advisor Dr. Scott D. Sommerfeldt for providing insightful research directions and all the "brainstorming" that provokes creativity. The unique way he presented his lectures leaves me a strong impression and stimulates my curiosity for knowledge.

I need to thank Dr. David G. Long, Dr. Jonathan Blotter and Dr. Kent L. Gee for providing me help and patience.

I want to dedicate this dissertation to Dr. Craig Smith who passed away. He had given me countless help in my research and he will be always remembered.

I'm grateful to my dear friends Ted and Cossette Morton and Wayne and Jenny Arballo who treat me as part of their families throughout these years. I could always fall back on them in times of difficulty. I also need to thank Wayne Arballo for his work in editing my dissertation.

I also want to thank my colleagues here at the acoustics research group who have provided me with a pleasant and encouraging research experience.

Lastly but most importantly, I want to thank my mom and dad who gave me life. I could have never made it this far without their support and the amount of faith they had in me.

TABLE OF CONTENTS

LIST OF TABLES

LIST OF FIGURES

Chapter 1

Introduction

1.1 Introduction

The research presented in this dissertation focuses on a unique approach to sound system equalization in enclosed sound fields, based on the measurement and control of total energy density. This new equalization scheme produces greater global equalization in defined listening areas, while significantly reducing the number of randomly sampled locations required for effective equalization filter design.

Two main factors contribute to the undesired spectral coloration of a signal in sound reproduction: (1) the frequency response of the audio system and (2) the in-situ acoustical response of the listening environment [1]. The audio signal is first filtered by the frequency response of the audio system, which normally includes an amplifier and one or more loudspeakers. The distorted signal radiates into a given listening environment with frequency-dependent coloration depending upon the angular direction relative to a defined principal radiation axis. Acoustic signals radiating inside a listening environment are also linearly distorted from frequency-dependent wall reflections, scattering, and interference. These artifacts can be characterized by the pressure impulse response at a certain listening position. The room impulse response is combined via convolution with the impulse response of the audio system to give the overall electroacoustic response of the sound reproduction system at this position. The original audio signal is inherently convolved with the composite impulse response in the time

domain to result in the signal received at the receiver location. The coloration produced by this impulse response is thus a function of both frequency and listening position.

One approach to equalization is to try to design an exact inverse filter of the pressure impulse response to deconvolve the composite impulse response [1] and thus remove its colorations. This filter is inserted between the source and the amplifier. The source signal is prefiltered by this equalization before being amplified and radiated from the loudspeakers into the listening environment.

1.2 Background

Audio professionals have long struggled to produce effective spectral equalization of loudspeakers in enclosed spaces. The process is intended to correct or adjust the composite frequency response function (transfer function) between the defined electronic input to the sound system and its acoustic pressure output to make it spectrally uniform or otherwise similar to a desired frequency-dependent function. (A variety of target "house curves" or other predetermined transfer function characteristics are possible.) While corrections are usually made electronically, they may also be made acoustically or electroacoustically. The latter are usually considered sound system or room "optimizations" that precede electronic equalization in the traditional sense. Because a transfer function is a complex frequency-domain function, equalization may address magnitude response, phase response, or both. It also affects the corresponding time response. However, the acoustic pressure output of an audio system typically depends strongly on receiver location. The transfer function and its equalization are then spatially dependent as well.

The spatial variation of an enclosed sound field imposes serious difficulties on the equalization process, leading many to conclude that loudspeakers cannot be equalized in rooms or that room filtering is uncorrectable, at least over extended listening areas. In recent years, some have abandoned steady-state and in situ equalization altogether, favoring only direct-sound or free-field equalization of loudspeakers as the best practical approach to the problem. Unfortunately, these practices neglect room filtering as a key and inseparable part of audio transmission that invariably impacts listeners with distinct audio signal colorations. A room is an integral part of the overall listening system that can produce dramatic spectral alterations to audio signals. Thus, to suggest that only the spectral response of a loudspeaker may be equalized via external electronic filters, while the spectral response of a room cannot be equalized, is to introduce something of a contradiction. To suggest that the spectral anomalies of a room can only be compensated through room-acoustics modifications is tantamount to suggesting that the spectral anomalies of a loudspeaker can only be compensated through internal physical loudspeaker modifications. While such optimization of both rooms and loudspeakers is obviously very important, the role of external electronic equalization is still essential.

Both the loudspeaker and the room are physical subsystems of the same audio transmission system. The loudspeaker has both spectral and spatial (angular) response characteristics. In free space, the on-axis frequency response will typically differ from an off-axis frequency response. The room likewise has spectral and spatial response characteristics. The frequency response at one point in a room will typically differ from the frequency response at another point. To successfully compensate for their spectral anomalies, one must understand the physical characteristics of these systems. In some cases, it is advantageous to separate the spectral and spatial effects. Traditional equalization of sound systems produces prefiltering of

electronic excitation signals with the focus of compensating the spectral part of the system response; it can do little if anything to compensate for the spatial filtering of the loudspeaker or room. This dissertation asserts that within a defined listening region, the global spectral anomalies of the loudspeaker/room response should be equalized to the extent possible, in accordance with their impact on the perception of audio signals.

The dissertation explores some of the problems of direct-sound and traditional in situ equalization methods, beginning with instructive one-dimensional models. The models are simple enough to bring clarity to the intertwined mechanisms involved in the equalization processes. They demonstrate that many problems with traditional equalization methods stem from the ubiquitous use of microphones to sense only acoustic pressure in sound fields. From an energetic standpoint, a typical microphone provides information only about the potential energy density of the field at its discrete position in space. Total energy density, which also involves kinetic energy density, has greater spatial uniformity, enhances observability, and provides a greater global view of enclosure filtering. Room resonances are examples of global phenomena that may or may not be observable by pressure receivers (including individual listener ears) at discrete field positions. Nevertheless, if a spectral anomaly is not readily detectable by traditional means at one position, it should still be corrected at the many other positions where it is detectable.

While room filtering effects are both spectral and spatial, typical electronic equalization of audio systems addresses only spectral aberrations through analog or digital filters. With this in mind, an improved approach to spectral equalization might be to simultaneously correct both loudspeaker and global spectral room responses. In other words, the approach would ignore spatial variation to the room responses. While such global equalization has been explored

through the use of numerous microphones and multichannel controllers, this paper proposes the use of total energy density as a practical approach to the problem because it accomplishes the task more efficiently through a single localized measurement. In one-dimensional systems, it inherently separates the equalizable loudspeaker spectral response and global spectral "room" response from the unequalizable spatial "room" response. Many of the benefits of energy density equalization also carry over to more complicated three-dimensional sound fields.

In the past, the design of equalization filters has been problematic. For example, one approach in industry is to sample the pressure response at a selected listening position or the "sweet spot." A minimum phase inverse pressure equalization filter is then calculated based on the overall frequency response at this sweet spot [2, 4]. Because the room response is dependent on the source and receiver positions [5, 6], an equalization filter based on the frequency response at one listening position may not be beneficial or may even worsen the coloration at other locations.

In order to achieve an optimal room equalization result for an extended listening area, the frequency responses at all listening locations must be considered. An inverse filter is then derived based on the average response to achieve a global equalization result. However, such effort becomes impractical as the area of listening environment increases, requiring a vast number of sample locations to cover the equalization region.

A practical approach is to select only a few random sample locations. The frequency responses at these locations are then averaged and an inverse filter is derived based on the average. Due to the random geometric variation of the listening environment, there is not a standard method to determine the optimal sample locations, whose average best represents the overall average response of the entire equalization region. Furthermore, studies have been done

to extend the target zone of the pressure equalization based on excited plane waves. The overall sound field is estimated based on the sensors placed only in a small equalization zone [6, 7]. However, a limited bandwidth is always associated with such methods.

Due to the spatially variant nature of the in situ acoustical response of a listening environment, some have suggested excluding its equalization from the overall audio transmission equalization [9]. Some recommend that only the direct sound of an audio system should be equalized and the room response ignored. Such suggestions fail to recognize the fact that even though each room response at a single location includes a spatially dependent coloration characteristic of its unique listening position, there is also a portion of the spectral coloration common to many or all listening positions. This common response is dependent upon the source, its position, and certain global sound field characteristics. An equalization filter typically compensates for spatially dependent coloration differently based on the listening position. Therefore, this part of the coloration cannot and should not be equalized in a broad listening area. However, an equalization filter can remove the coloration of the common fraction of the overall coloration—regardless of the listening position. In other words, the global spatial coloration should be the target of the equalization process.

Another problem the traditional equalization techniques encounter is the averaging method. As mentioned before, in order to cover the entire equalization region, a few random sample locations are selected and the pressure responses at these locations are sometimes summed by practitioners through a mixing device. Because of the random phase variation of the room responses, this pressure-based averaging will likely cause the response to cancel for certain frequencies and result in a loss of information for the equalization filter at such frequencies.

Currently there are no numerical standards to evaluate the uniformity of a sound field after it has been equalized. Thus, there is not a standard qualification to compare the efficiency of different equalization schemes. In this dissertation, methods of extracting the spatially independent global spectral coloration from the overall room coloration are suggested and implemented. A new averaging method is proposed, an energy-based equalization is proposed, and a global equalization figure of merit is used to compare the quality of different equalization schemes.

1.3 Objectives

A practical method of achieving global equalization using a minimum number of sample locations is desired. This dissertation will present a new equalization method based on total energy density and compare the benefits and limitations of the new method to traditional pressure-based equalization techniques.

To address the problems that traditional averaging techniques expose, the research explores an averaging method based on squared pressure or potential energy density. This energy-based averaging method prevents the cancellation of useful spectral information due to the phase differences of the pressure responses at different sampling positions. The complete average is shown to create the optimal global equalization results within the overall averaging area. However, in order to calculate this spatially averaged squared pressure in a practical sense, a vast number of sample locations are needed to cover the averaging area. In order to reduce the number of sample locations, a new quantity is sought that is more spatially uniform than the pressure field while representing the common spectral properties of the pressure field at all locations.

The total energy density field is shown to be less spatially variant than the pressure field itself. In certain one-dimensional fields, it is location independent and nearly identical to the spatially averaged squared pressure. Therefore, the latter can be estimated by a single point energy density measurement. Due to its uniform nature, total energy density successfully extracts the global spectral coloration of the field and the electroacoustic portion of the audio system. The resulting equalization filter then allows one to effectively equalize both the audio system and the spatially independent portion of the room response. Because of the increased uniformity of the total energy density field compared to the pressure field, fewer samples are required to generate an estimate of the average of all the field location responses. While total energy density is not uniform in three-dimensional fields, it is still more uniform than the pressure field.

Energy density is a zero phase quantity. As a result, its frequency response cannot be directly inverted to derive a causal and stable equalization filter [2, 4] [9, 10]. However, a minimum-phase version of the energy density frequency response can be efficiently inverted. This dissertation will discuss how to efficiently calculate the minimum phase portion of the energy density response using the Hilbert transform. A causal and stable equalization filter is thus derived based solely on the inversion of the minimum phase portion of the energy density response.

A statistical standard is proposed in this dissertation to quantitatively compare the uniformity of the equalized sound fields. The figure of merit is derived based on the standard deviation of both the spectral and spatial variations of the sound field. Ideally, the figure reaches its minimum value when the sound field is equalized by the spatially averaged squared pressure. This figure increases as the field becomes increasingly nonuniform, both spatially and spectrally.

An efficient equalization scheme will yield a small figure of merit. Because the figure is normalized, it does not depend on the maximum sound pressure level of the sound field. It can therefore be utilized generically for any equalized sound field.

1.4 Plan of development

Chapter 2 will present theoretical models of a one-dimensional acoustic field using analogous circuits for a loudspeaker at the end of a plane-wave tube. Pressure and energy density-based equalization filters are derived and used to equalize the sound field numerically. In Chapter 3, different inverse filtering schemes will be addressed. The pressure and energy density inverse filters are again derived and used for experimental equalization. A global listening area equalization coefficient (GLAEC) is derived and used to quantify the filter efficiency for the one-dimensional system. In Chapter 4, theoretical models of a one-dimensional field with the source on the side of the tube are derived and compared. Experimental results based on the theoretical filter designs are discussed and compared to the theoretical models. As before, equalization filters based on pressure and energy density are applied to equalize the pressure field. Chapter 5 presents a theoretical model of a practical source in a three-dimensional acoustic field. The theoretical pressure and energy density-based equalization filters are then derived and used as the basis for experimental equalizations. The qualities of the equalization schemes are compared and discussed. Finally, Chapter 6 provides the conclusions of the research and discusses its benefits and shortcomings. Future research topics are also suggested.

References

[1] Masato Miyoshi and Yutaka Kaneda, "Inverse filtering of room acoustics," IEEE Transaction on Acoustics, Speech, and Signal Processing , VOL. 36, NO. 2, February 1988.

[2] Sunil Bharitkar Philip Hilmes and Chris Kyriakakis, "Sensitivity of Multichannel Room Equalization to Listener Position," IEEE, Proceedings of the 2003 International Conference on Multimedia and Expo, VOL 2, (721-724).

[3] Arturo O. Santillan, "Spatially extended sound Equalization in rectangular rooms," J. Acoustical Soc. Am. Vol. 110, No. 4, Oct 2001.

[4] John C. Sarris and Finn Jacobsen, "Sound equalization in a large region of a rectangular enclosure," Acoustical Society of America Journal, Volume 116, Issue 6, pp. 3271-3274 (2004).

[5] R.M. Howe and Dr. M.O.J. Hawksford, "A methodological critique of local room equalization techniques," Digital Audio Signal Processing, IEE Colloquium on, 6/1-6/4, May 1991.

[6]S.T. Neely and J.B. Allen, "Invertibility of a room impulse response," J. Acoustic Society of America Vol 66. No. pp165-169 July 1979.

[7] J. Mourjopoulos, "On The Variation and Invertibility of Room Impulse Response Functions," Journal of Sound and Vibration (1985) 102 (2), 217-228.

[8] Masato Miyoshi and Yutaka Kaneda, " Inverse Filtering of Room Acoustics," IEEE Transactions on Acoustics, speech and signal processing, vol 36, No. 2 Feb 1988.

[9] J. Mourjopoulos, "Digital Equlization of Room Acoustics," J. Audio Eng. Soc. Vol. 42, pp. 884-900 (1994 Nov.).

[10] S.G. Norgross, G.A. Soullodre, and M.C. Lavoie, "Subjective Investigation of Inverse Filtering," J. Audio Eng. Soc., Vol 52, pp. 1003-1027 (2004, Oct.).

Chapter 2

Energy Density Equalization of Loudspeakers and Enclosed Spaces: Initial Developments for One-Dimensional Sound Fields

2.1 Equalization Methods

Several approaches to the equalization problem may be explained and compared, at least from an initial standpoint, using the frequency-domain block diagram in Fig. 2.1. A complex voltage $\hat{e}_g(f)$ from a signal generator drives a loudspeaker with the frequency response function $L(f)$, which in turn excites the sound field in a plane-wave tube. The frequency response function between the loudspeaker and an ideal acoustic sensor at the field position x_s is represented by the spatially dependent $H(x_s, f)$. The sensor observes the one-dimensional field at this position, producing either a pressure signal, a particle velocity signal, or another signal related to these quantities. The subscripts p and u on the frequency response function correspond to the pressure and particle velocity signals, respectively. An equalization (EQ) filter $A(x_s, f)$ specific to the sensor position may be inserted before the loudspeaker to compensate for spectral anomalies of a given sensor output signal.

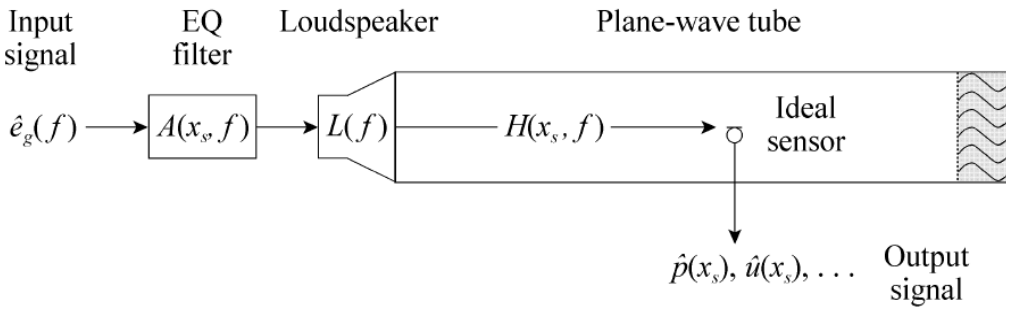

FIG. 2.1. One-dimensional sound system block diagram.

Without the equalization filter in place, the sensor produces a complex pressure signal

$$\hat{p}_a\ x_s, f\ = \hat{e}_g\ \ f\ \ L\ \ f\ \ H_p\ \ x_s, f \qquad \textbf{(2. 1)}$$

(the subscript *a* denotes an unequalized signal). Once the filter is inserted, it becomes

$$\hat{p}_b\ \ x_s, f\ \ = \hat{e}_g\ \ f\ \ A_p\ \ x_s, f\ \ L\ \ f\ \ H_p\ \ x_s, f \qquad \textbf{(2. 2)}$$

(the subscript *b* denotes an equalized signal). To make the acoustic pressure consistently proportional to $\hat{e}_g(f)$ at all frequencies, the filter must take on the inverse characteristic

$$A_p\ \ x_0, f\ \ \propto \frac{1}{L\ \ f\ \ H_p\ \ x_0, f} = \frac{\hat{e}_g\ \ f}{\hat{p}_a\ \ x_0, f}. \qquad \textbf{(2. 3}$$

At positions other than x_s, the filter may or may not improve equalization. The pressure over the entire field becomes

$$\hat{p}_b\ \ x, f\ \ = \hat{e}_g\ \ f\ \ A_p\ \ x_s, f\ \ L\ \ f\ \ H_p\ \ x, f\ \ . \qquad \textbf{(2. 4)}$$

If the sensor output signal is the frequency-dependent, time-averaged, potential energy density,

$$\begin{aligned}\left\langle w_{p,b}\ \ x_s, f, t\ \right\rangle_t &= \frac{1}{4\rho_0 c^2}\left|\hat{p}_b\ \ x_s, f\ \right|^2 \\ &= \frac{1}{2}\left|\hat{e}_g\ \ f\ \right|^2 \frac{1}{2\rho_0 c^2}\left|A_{wp}\ \ x_s, f\ \right|^2 \left|L\ \ f\ \right|^2 \left|H_p\ \ x_s, f\ \right|^2 \\ &= \left\langle e_g^2\ \ f, t\ \right\rangle_t \frac{1}{2\rho_0 c^2}\left|A_{wp}\ \ x_s, f\ \right|^2 \left|L\ \ f\ \right|^2 \left|H_p\ \ x_s, f\ \right|^2,\end{aligned} \tag{2. 5}$$

it will be consistently proportional to the frequency-dependent, mean-square input voltage $\left\langle e_g^2\ \ f, t\ \right\rangle_t$ at all frequencies as long as the filter has the form

$$\left|A_{wp}\ \ x_s, f\ \right| \propto \left[\frac{2\rho_0 c^2}{\left|L\ \ f\ \right|^2 \left|H_p\ \ x_s, f\ \right|^2}\right]^{\frac{1}{2}} = \left[\frac{\left\langle e_g^2\ \ f, t\ \right\rangle_t}{\left\langle w_{p,a}\ \ x_s, f, t\ \right\rangle_t}\right]^{\frac{1}{2}} \tag{2. 6}$$

(a magnitude only equalization specific to the field position x_s). The pressure over the field then becomes

$$\hat{p}_b\ \ x, f\ = \hat{e}_g\ \ f\ \left|A_{wp}\ \ x_s, f\ \right| L\ \ f\ \ H_p\ \ x, f\ . \tag{2. 7}$$

The lack of phase correction in the filter may or may not degrade the global equalization.

Similar results follow for the equalization of the complex particle velocity signal $\hat{u}\ \ x_s, f$ and the frequency-dependent, time-averaged, kinetic energy density $\left\langle w_{p,b}\ \ x_s, f, t\ \right\rangle_t$:

$$A_u\ \ x_s, f\ \propto \frac{1}{L\ \ f\ \ H_u\ \ x_s, f} = \frac{\hat{e}_g\ \ f}{\hat{u}_a\ \ x_s, f}, \tag{2. 8}$$

$$\left|A_{wp}\ \ x_s, f\ \right| \propto \left[\frac{2}{\rho_0 \left|L\ \ f\ \right|^2 \left|H_u\ \ x_s, f\ \right|^2}\right]^{\frac{1}{2}} = \left[\frac{\left\langle e_g^2\ \ f, t\ \right\rangle_t}{\left\langle w_{k,a}\ \ x_s, f, t\ \right\rangle_t}\right]^{\frac{1}{2}}. \tag{2. 9}$$

Another filter could be based on the total energy density at the field point x_s:

$$\left\langle w_{t,b}\ \ x_s, f, t\ \right\rangle_t = \left\langle e_g^2\ \ f, t\ \right\rangle_t \left|A_{wt}\ \ x_s, f\ \right|^2 \left|L\ \ f\ \right|^2 \left[\frac{1}{2\rho_0 c^2}\left|H_p\ \ x_s, f\ \right|^2 + \frac{\rho_0}{2}\left|H_u\ \ x_s, f\ \right|^2\right]. \tag{2. 10}$$

(As shown later, the total energy density is actually uniform over a one-dimensional sound field;

dependence upon x_s is shown here only for consistency with the previous expressions.) To assure a uniform proportionality to the frequency-dependent, mean-square voltage $\langle e_g^2 \ f,t \ \rangle_t$ at all frequencies, the filter must have the magnitude characteristic

$$|A_{wt} \ x_s, f \ | \propto \left[\frac{1}{|L \ f \ |^2 \left[\frac{1}{2\rho_0 c^2} |H_p \ x_s, f \ |^2 + \frac{\rho_0}{2} |H_u \ x_s, f \ |^2 \right]} \right]^{\frac{1}{2}} = \left[\frac{\langle e_g^2 \ f,t \ \rangle_t}{\langle w_{t,a} \ x_s, f,t \ \rangle_t} \right]^{\frac{1}{2}}. \quad \textbf{(2. 11)}$$

The sensor may also produce a signal that is a linear combination of the acoustic pressure and particle velocity, i.e.,

$$\langle w_{t,b} \ x_s, f,t \ \rangle_t = \langle e_g^2 \ f,t \ \rangle_t |A_{wt} \ x_s, f \ |^2 |L \ f \ |^2 \left[\frac{1}{2\rho_0 c^2} |H_p \ x_s, f \ |^2 + \frac{\rho_0}{2} |H_u \ x_s, f \ |^2 \right]. \quad \textbf{(2. 12)}$$

where C_1 and C_2 are arbitrary constants. After insertion of an equalization filter, this becomes

$$\hat{s}_b \ x_0, f \ = \hat{e}_g \ f \ A_s \ x_0, f \ L \ f \ \left[C_1 H_p \ x_0, f \ + C_2 H_u \ x_0, f \ \right]. \quad \textbf{(2. 13)}$$

To make the signal consistently proportional to $\hat{e}_g(f)$ at all frequencies, the filter takes on the form

$$\begin{aligned} A_s \ x_s, f \ &\propto \frac{1}{L \ f \ \left[C_1 H_p \ x_s, f \ + C_2 H_u \ x_s, f \ \right]} \\ &= \frac{\hat{e}_g \ f}{C_1 \hat{p}_a \ x_s, f \ + C_2 \hat{u}_a \ x_s, f} \\ &= \frac{\hat{e}_g \ f}{\hat{s}_a \ x_s, f}. \end{aligned} \quad \textbf{(2. 14)}$$

The magnitude of the filter may be written as

$$
\begin{aligned}
|A_s\ x_s, f\ | &\propto \left[\frac{1}{|L\ f\ |^2 |C_1 H_p\ x_s, f\ + C_2 H_u\ x_s, f\ |^2} \right]^{\frac{1}{2}} \\
&= \left[\frac{1}{|L\ f\ |^2\ C_1^2 |H_p\ x_s, f\ |^2 + 2C_1 C_2 \mathrm{Re}\left[H_p\ x_s, f\ H_u^*\ x_s, f\ \right] + C_2^2 |H_u\ x_s, f\ |^2} \right]^{\frac{1}{2}} \\
&= \left[\frac{\langle e_g^2\ f, t\ \rangle_t}{\langle s_a^2\ x_s, f, t\ \rangle_t} \right]^{\frac{1}{2}},
\end{aligned}
\tag{2. 15}
$$

which is similar in some respects to the total energy density filter described in Eq. (2.11). If the arbitrary constants are chosen to be $C_1 = \sqrt{1/2\rho_0 c^2}$ and $C_2 = \sqrt{\rho_0 / 2}$, the magnitude becomes

$$
|A_s\ x_s, f\ | \propto \left[\frac{\langle e_g^2\ f, t\ \rangle_t}{\langle w_{t,a}\ x_s, f, t\ \rangle_t + \frac{1}{c} \langle I_a\ x_s, f, t\ \rangle_t} \right]^{\frac{1}{2}}, \tag{2. 16}
$$

where

$$
\langle I_a\ x_s, f, t\ \rangle_t = \frac{1}{2} \mathrm{Re}\left[\hat{p}\ x_s, f\ \hat{u}^*\ x_s, f\ \right] \tag{2. 17}
$$

is the time-averaged acoustic intensity before the insertion of the filter. Interestingly, for an ideal one-dimensional standing-wave field, $\langle I_a\ x_s, f, t\ \rangle_t = 0$, so $|A_s\ x_s, f\ | = |A_{wt}\ x_s, f\ |$. For an ideal one-dimensional propagating wave field, $\langle I_a\ x_s, f, t\ \rangle_t = c \langle w_{t,a}\ x_s, f, t\ \rangle_t$, so $|A_s\ x_s, f\ | = |A_{wt}\ x_s, f\ | / \sqrt{2}$. Fields between these two extremes yield filters between the extremes.

2.2 Modeling of the One-dimensional System

The analytical model used to calculate responses and field quantities is based on the more detailed system depicted in Fig. 2.2. It consists of a plane-wave tube of length L_T and uniform cross-sectional area S_T, which is driven at one end by a moving-coil loudspeaker and terminated

at the other end by an arbitrary acoustic impedance Z_{ATT}. The loudspeaker is backed by a sealed box with length L_B, uniform cross-sectional area S_B, and a termination impedance Z_{ABT}. The effective radiating area S_D of the loudspeaker diaphragm is chosen such that $S_D \# S_B$ and $S_D \# S_T$. While the figure shows the cross-sectional area S_B to be greater than S_T, it could be less than or equal to S_T without affecting the general model characteristics. The sound field may be assessed at any position x. This includes but is not limited to the equalization sensor position x_s.

The complete multi-domain analogous circuit for the system is shown in Fig. 2.3. It represents the one-dimensional axial wave effects in the loudspeaker enclosure and tube while assuming spatially averaged or uniform acoustic pressures over their cross sections. Its solution in the form shown provides the complex spatially averaged acoustic pressure amplitude $\langle \hat{p}\ x \rangle_{S_T}$ and the complex volume velocity amplitude $\hat{U}(x)$ for any field position x. If the contributions of evanescent cross modes are negligible at a given position, the spatially averaged pressure may be replaced with the cross-sectionally uniform pressure and the axial particle velocity follows directly from the volume velocity as $\hat{u}\ x = \hat{U}\ x\ \vec{e}_x / S_T$, where $\vec{e}_x$ is the unit vector in the x direction. The circuit also accounts for long-wavelength effects produced by differences in the cross-sectional areas S_B, S_D, and S_T through area gyrators.

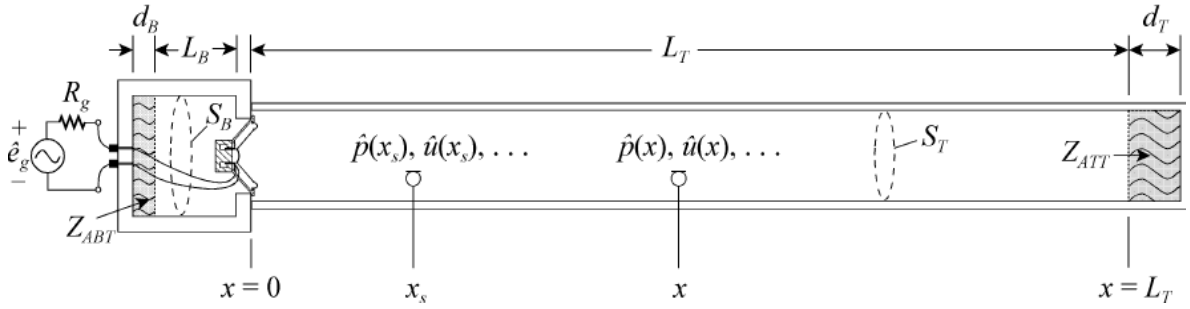

FIG. 2.2. Model of the one-dimensional tube.

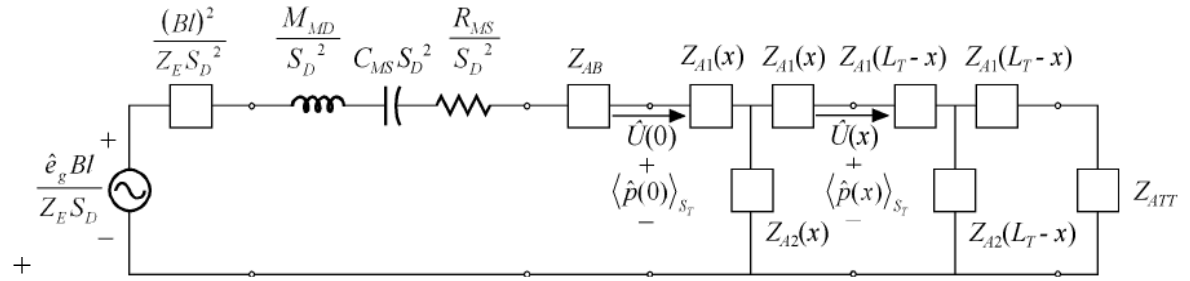

FIG. 2.3. Multi-domain analogous circuit of the one-dimensional tube.

Simplification of the circuit follows by implementing several substitutions and reductions. Working from left to right, the box termination impedance Z_{ABT} is first translated through the box *T*-network to load the back side of the driver with the box impedance

$$Z_{AB} = \frac{\rho_0 c}{S_B}\left(\frac{Z_{ABT} + j\frac{\rho_0 c}{S_B}\tan kL_B}{\frac{\rho_0 c}{S_B} + jZ_{ABT}\tan kL_B}\right). \qquad \textbf{(2. 18)}$$

The series combination of the three electric impedances may also be expressed as the single electric impedance

$$Z_E = R_g + R_E + j\omega L_E. \qquad \textbf{(2. 19)}$$

By pulling Z_{AB} through the area gyrator, Z_E and the electric source through the transformer, and performing a source conversion, one can represent all electric source elements, loudspeaker driver elements, and loudspeaker enclosure elements as a parallel combination in the mechanical mobility domain. These mobility elements are then pulled through the second area gyrator to the acoustic impedance domain of the tube to yield the simplified representation shown in Fig. 2.4.

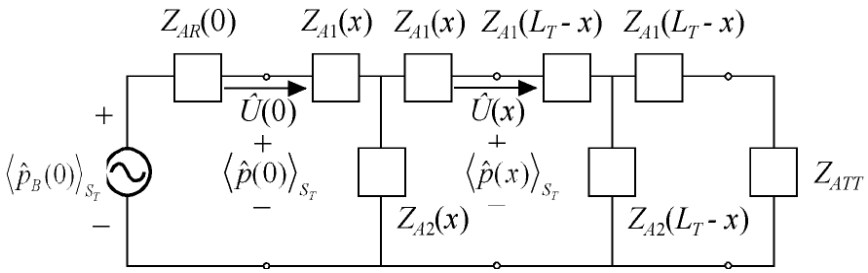

FIG. 2.4. Simplified equivalent circuit after the impedance translations.

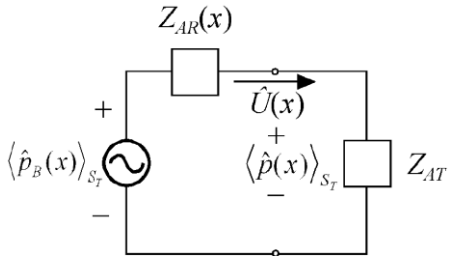

FIG. 2.5. Simplification using Thevenin equivalent circuit.

As shown in Fig. 2.5, further simplification results by using a Thevenin equivalent circuit for all elements to the left of $x = 0$. The Thevenin equivalent source is characterized by the spatially averaged blocked pressure amplitude

$$\langle p_B \ 0 \rangle_{S_T} = \frac{\hat{e}_g Bl}{Z_E S_D} \tag{2. 20}$$

and the series acoustic radiation impedance looking into the loudspeaker from the tube, after the

original source element is replaced by its internal impedance:

$$Z_{AR}\ 0\ = \frac{Bl^{\ 2}}{Z_E S_D^{\ 2}} + \frac{R_{MS}}{S_D^{\ 2}} + \frac{1}{j\omega C_{MS} S_D^{\ 2}} + j\omega \frac{M_{MD}}{S_D^{\ 2}} + Z_{ABT}. \tag{2. 21}$$

A final simplification follows by defining a different Thevenin equivalent source at position x and translating the tube termination impedance Z_{ATT} to x as shown in Fig. 6. In this case,

$$\left\langle p_B\ x \right\rangle_{S_T} = \left\langle p_B\ 0 \right\rangle_{S_T} \left[\frac{\frac{\rho_0 c}{S_T}}{\frac{\rho_0 c}{S_T} \cos kx + jZ_{AR}\ 0\ \sin kx} \right], \tag{2. 22}$$

$$Z_{AR}\ x\ = \frac{\rho_0 c}{S_T} \left(\frac{Z_{AR}\ 0\ + j\frac{\rho_0 c}{S_T} \tan kx}{\frac{\rho_0 c}{S_T} + jZ_{AR}\ 0\ \tan kx} \right), \tag{2. 23}$$

and

$$Z_{AT}\ x\ = \frac{\rho_0 c}{S_T} \left(\frac{Z_{ATT} + j\frac{\rho_0 c}{S_T} \tan k\ L - x}{\frac{\rho_0 c}{S_T} + jZ_{ATT} \tan k\ L - x} \right). \tag{2. 24}$$

From this simple circuit, one can readily determine the basic acoustic field quantities in the one-dimensional tube in terms of previously defined quantities:

$$\left\langle \hat{p}\ x \right\rangle_{S_T} = \left\langle \hat{p}_B\ x \right\rangle_{S_T} - \hat{U}\ x\ Z_{AR}\ x\ = \hat{U}\ x\ Z_{AT}\ x\ , \tag{2. 25}$$

$$\hat{U}\ x\ = \frac{\left\langle \hat{p}_B\ x \right\rangle_{S_T}}{Z_{AR}\ x\ + Z_{AT}\ x}. \tag{2. 26}$$

Again, if we assume x is truly in the plane-wave region of the tube (i.e., where the field is devoid of significant cross-mode contributions), we can assume cross-sectional uniformity $\hat{p}(x)$ and $\hat{u}(x)$, such that their spatial averages become unnecessary. In this case, the time-averaged potential, kinetic, and total energy densities may be written as

$$\left\langle w_p\ x \right\rangle_t = \frac{1}{4}\frac{\left|\hat{p}\ x\right|^2}{\rho_0 c^2}, \tag{2. 27}$$

$$\left\langle w_k\ x \right\rangle_t = \frac{1}{4}\rho_0 \hat{\vec{u}}\ x \cdot \hat{\vec{u}}^*\ x\ , \tag{2. 28}$$

and $\left\langle w_t\ x \right\rangle_t = \left\langle w_p\ x \right\rangle_t + \left\langle w_k\ x \right\rangle_t = \frac{1}{4}\frac{\left|\hat{p}\ x\right|^2}{\rho_0 c^2} + \frac{1}{4}\rho_0 \hat{\vec{u}}\ x \cdot \hat{\vec{u}}^*\ x\ .$ **(2. 29)**

The box and tube termination impedances Z_{ABT} and Z_{ATT} might be modeled as impedances associated with porous layers of material with depths d_B and d_T, respectively. The Rayleigh model for porous materials roughly characterizes their frequency-dependent behaviors [1]. For a given termination of depth d and cross-sectional area S, the acoustic impedance is approximately

$$Z_A = -j\frac{\rho_0 c}{\sigma S_T}\left(1 - j\frac{\Xi'}{\rho_0 \omega}\right)^{1/2} \cot \tilde{k}_m d, \tag{2. 30}$$

where Φ is the porosity (i.e., the ratio of open-to-closed area), Ξ' is the specific flow resistance, and

$$\tilde{k}_m = k\left(1 - j\frac{\Xi'}{\rho_0 \omega}\right)^{1/2} \tag{2. 31}$$

is the complex acoustic wave number within the material. The pressure-amplitude reflection coefficient looking into the termination is then

$$\left\langle w_t\ x \right\rangle_t = \left\langle w_p\ x \right\rangle_t + \left\langle w_k\ x \right\rangle_t = \frac{1}{4}\frac{\left|\hat{p}\ x\right|^2}{\rho_0 c^2} + \frac{1}{4}\rho_0 \hat{\vec{u}}\ x \cdot \hat{\vec{u}}^*\ x\ . \tag{2. 32}$$

and the absorption coefficient is

$$\alpha_T = 1 - \left|R_T\right|^2. \tag{2. 33}$$

(See Ref. [1]).

Propagation losses over the length of the tube or loudspeaker enclosure may also be addressed through the introduction of a complex wave number $\tilde{k} = k - j\alpha_p$, where α_p is the total propagation absorption coefficient [2]. However, for many practical tube an enclosure lengths, cross-sectional areas, and terminations, the effects of these propagation losses are negligible. For rigid terminations, $\tilde{k}$ helps maintain a bounded sound-field response.

2.3 Speaker Box modeling

When measuring the Thiele-Small parameters of a driver in free air, the acoustic loading on its diaphragm is typically considered to be that of a flat, thin, rigid, unbaffled, circular disk. One might consider the loading on the front side of the driver to be similar to that in this simple idealization, but the loading on the rear side, and the acoustic interactions between the front side and rear side are certainly quite different. Much depends on the presence, sizes, and additional properties of the cone, coil former (with possible venting), spider, frame (including locations and sizes of openings), magnet structure (with possible pole-piece venting), and other factors. The rear of the diaphragm is thus loaded with a relatively complicated acoustic filter, whose frequency-dependent properties are unlikely to be well-represented by those of the ideal disk vibrating in free air.

The various transmission paths behind the diaphragm introduce inertance, compliance, and resistance. Each aperture, constriction, and transition between the various regions likewise introduces additional inertance and resistance. Many of these effects are certainly present in the free-air measurements, but others may be introduced by the unique loading of the driver into an enclosure. In addition to the obvious properties of the enclosure, the constrictions and transitions

between the driver, the baffle opening, and the enclosure walls provide additional inertance and resistance that are peculiar to the distinct driver-enclosure combination. They may be particularly significant if the enclosure elements fit tightly around the driver. In any case, the acoustic impedance Z_{AB} presented to the driver by the enclosure cannot be wholly independent of the driver itself, as is usually assumed, but must depend upon its presence, specific construction, and mounting. Whether in free air or an enclosure, certain acoustic filtering effects of the rear driver elements are consistently present and are thus indirectly accounted for through conventional driver parameter measurements. However, the effects are usually considered to be removed from the parameters by subtracting the simple theoretical fluid mass loading of the ideal disk (i.e., to extract M_{MD} from M_{MS}). This is clearly inadequate. While some acoustical effects may be present in both the actual driver and the simplified theory, others remain and are incorporated into the measured parameters (e.g., M_{MD}, C_{MS}, R_{MS}, etc.). The best method for accurately incorporating the coefficients into the source models is to use the in-vacuo measurement of these parameters which are not subject to the coupling of the air loading.

2.4 Experimental Measurement of the box impedance

A new method of measuring the box impedance Z_{AB} is introduced in this section. In practice, box impedances are usually modeled with a few lumped elements. However, this approach is not sufficient to describe the complicated geometric structure inside the box behind the loudspeaker cone. The absorption produced by the enclosure is often not a single value, but dependent upon frequency. A method is introduced here to assess Z_{AB} by using the enclosed loudspeaker as a passive termination to an excited one-dimensional sound field (see Fig. 2.6).

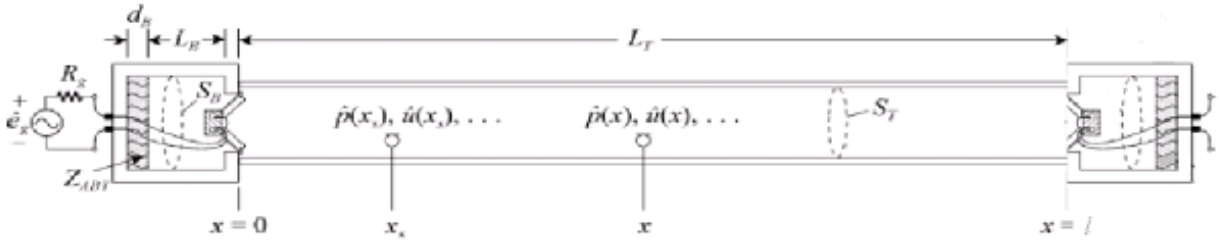

FIG. 2.6. Box impedance measurement setup.

The reflection coefficient at microphone positions 1 and 2 can each be calculated from the transfer function between the two microphones:

$$R_1 = -\frac{(H_{12} - e^{-jkl_{12}})}{H_{12} - e^{jkl_{12}}} e^{2jkl_{12}}, \tag{2. 34}$$

$$R_2 = -\frac{1/H_{12} - e^{-jkl_{12}}}{1/H_{12} - e^{jkl_{12}}} e^{2jkl_{12}}, \tag{2. 35}$$

where R_1 and R_2 are the reflection coefficients at microphone locations 1 and 2, H_{12} is the measured transfer function between the two microphones, k is the wave number, and l_{12} is the distance between the two microphones. This reflection coefficient can be translated to the position of the loudspeaker cone through the translation equation

$$R = R_2 e^{2jkl_2}, \tag{2. 36}$$

where l_2 is the distance between the second microphone and the equivalent speaker cone location. The impedance looking into the cone can be derived from the reflection coefficient at the location of the speaker cone as

$$Z_A = \frac{\rho_0 c}{S_T} \frac{1+R}{1-R} \tag{2. 37}$$

Once the transfer function is measured using the correct frequency resolution, the acoustic box impedance can be derived directly from Eq. (2.37) by subtracting the portion of the impedance associated with the in vacuo mechanical driver parameters M_{MD}, C_{MS}, and R_{MS}. Figure 2.7 shows the measured box impedance of the loudspeaker box used in this research.

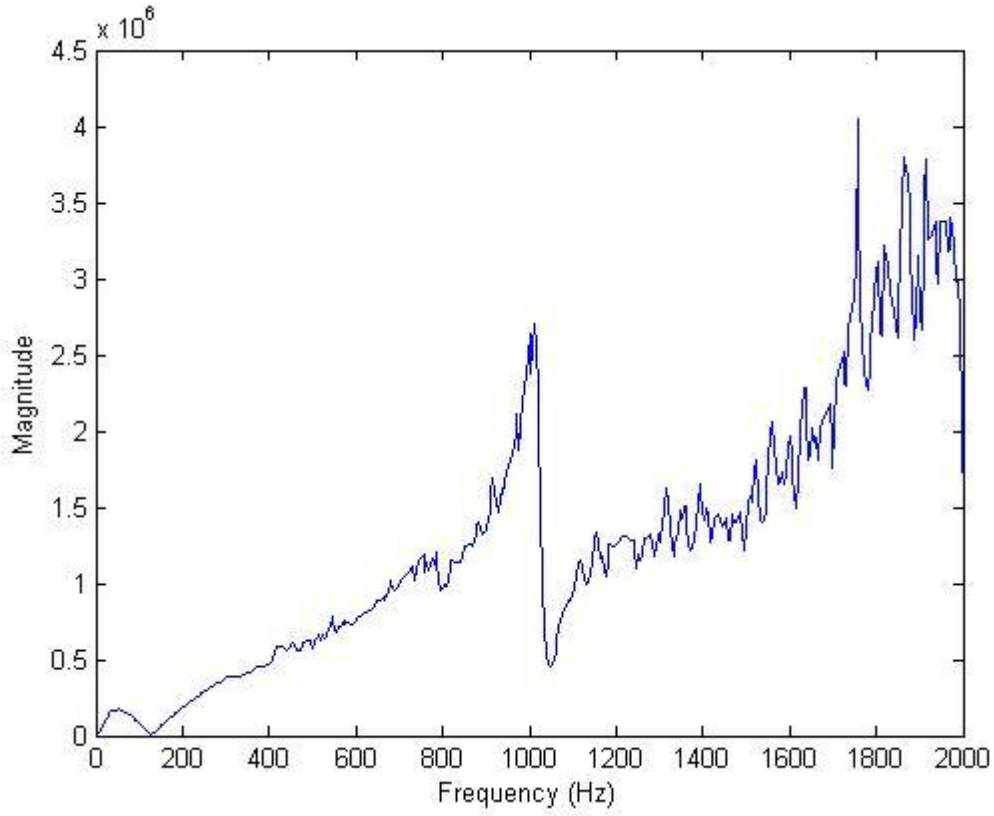

FIG. 2. 7. Measured speaker box impedance.

2.5 In vacuo speaker lumped element measurement

The three lumped element parameters M_{MD}, C_{MS}, and R_{MS} in Fig. 2.3 are transferred from the mechanical mobility domain to the acoustic impedance domain. They describe the mechanical characteristics of the loudspeaker driver without any fluid loading. Therefore, the parameters should be measured when the driver is placed in a vacuum chamber. In this research,

the pressure inside the vacuum chamber was lowered in steps and the speaker parameters were measured when each step of pressure equilibrium was reached. Table 2-1 and Fig. 2.8 show the values of the parameters under different pressures.

Table 2-1 Speaker parameters measured under different pressures.

Pressure (inHg)	M_{MD}	C_{MS}	R_{MS}
0.5	4.7055	641.3693	0.424865
2.5	4.71	647.098	0.448709
5	4.756	642.819	0.459693
7.5	4.784	627.138	0.518062
10	4.786	642.107	0.484825
15	4.904667	651.3273	0.445732
20	4.912	672.531	0.401912
22.5	4.990667	683.2793	0.386187
30	5.1405	688.072	0.327185

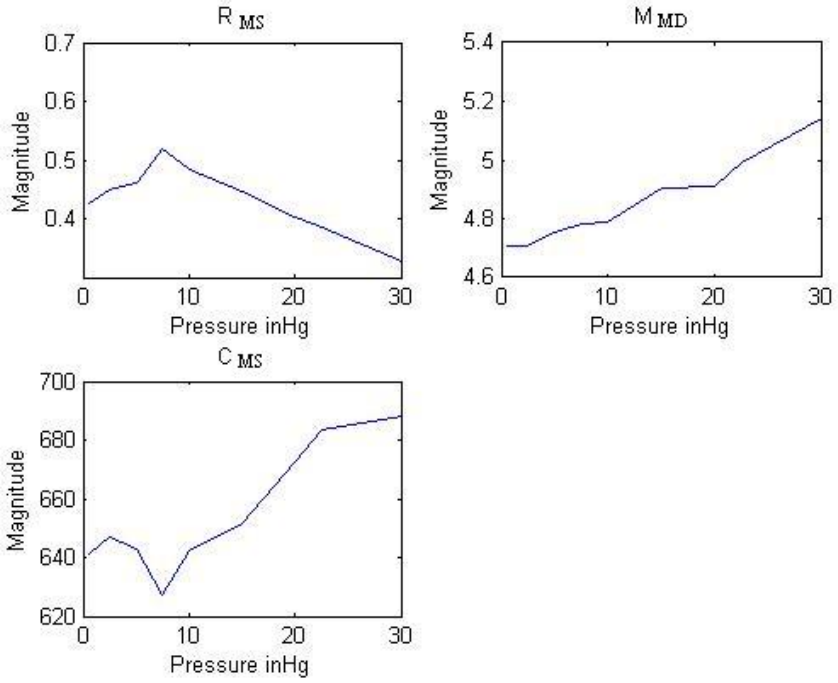

FIG. 2.8. Measured Speaker parameters under different pressures.

As the pressure decrease, the parameter M_{MD} decreases accordingly. However, there is a non-linear rise in the parameter C_{MS} from 8 in Hg down to 0.5 in Hg. The parameter R_{MS} increases as the pressure decreases and a similar anomaly occurs from 8 in Hg to 0.5 in Hg. The parameter values at 0.5 in Hg were incorporated as the in vacuo parameters in the equivalent circuit.

2.6 Numerical modeling and experimental measurement comparison

A 74.8 cm long one-dimensional tube was modeled using the equivalent circuit solutions derived previously. A loudspeaker box located at the left end of the tube functioned as the excitation source. A steel plate located at the right end to the tube functioned as the rigid boundary condition. The measured box impedance was used in the calculations. The modeled and measured pressures at a location 37.4 cm away from the source are compared in Fig 2.8. The two curves show a great degree of agreement.

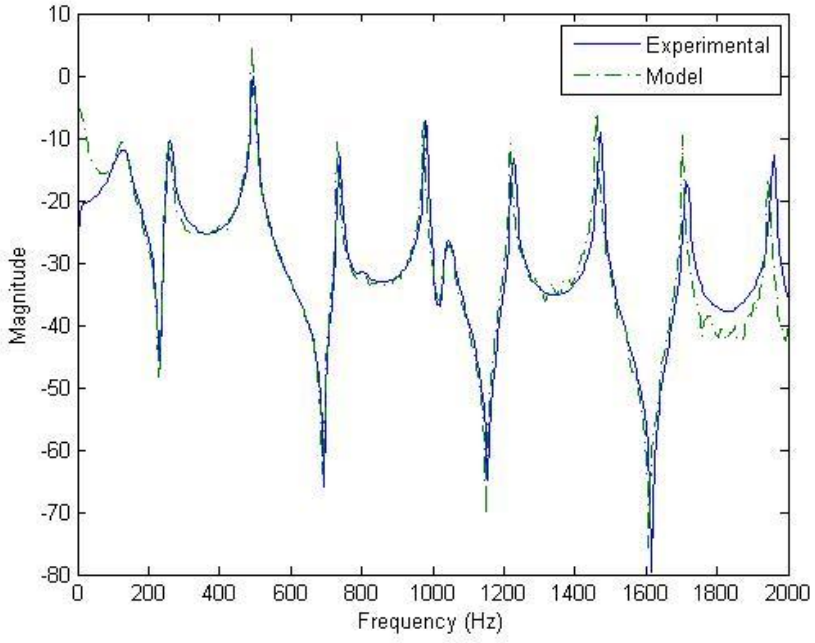

FIG. 2.9. Comparison of the model to the experimental measurements.

2.7 Conclusions

This chapter discussed the physical quantities that can be used as the basis of the inverse equalization filter. A theoretical equivalent circuit model was proposed to model the pressure field in a one-dimensional tube with a loudspeaker box on one end and a rigid boundary on the other end. A new method of measuring the speaker box impedance was introduced. The theoretical pressure field model has shown good agreement with experimental data.

References

[1] H, Kuttruff, *Room Acoustics* (Spon Press, London, 2000).

[2] A. D. Pierce, *Acoustics: An Introduction to Its Physical Principles and Applications* (Acoustical Society of America, New York, 1989).

[3] L. E. Kinsler, A. R. Frey, A. B. Coppens, and J. V. Sanders, *Fundamentals of Acoustics*, 4th ed. (Wiley, New York, 2000).

Chapter 3

Numerical Derivation of the Inverse Equalization Filter

The response of a room to an audio signal can be characterized by the impulse response functions at different locations within the listening area. The coloration of the room can then be simulated by linearly convolving the impulse response function with an original source signal in the time domain. Within the frequency domain, the colorations are usually complex. The magnitude variations of the frequency response function (FRF) result in spectral distortions. The phase of the frequency response function results in added artifacts of delay, reverberation, etc. The loudspeaker likewise color the original audio signal via convolution of its response.

One way to effectively remove room coloration is to convolve the original signal with an equalization filter that inverts the acoustic effects of the electroacoustic system. However, because loudspeaker and room responses are typically nonminimum phase, directly inverting a response filter does not always give a stable and causal inverse filter. For instance the inverse operator will be of infinite length even if the original impulse response is finite[1]. Early solutions to the problem utilized a homomorphic algorithm to derive the minimum phase portion of the FRF, and invert it in order to generate a finite causal inverse filter in the time domain [5]. The inversion process is done in the frequency domain that is associated with a circular convolution in the time domain. When such filters are used in the time domain to linearly deconvolve the system coloration, the inversion quality suffers and the deconvolution result often fails to converge to a single impulse. A weighted homomorphic method was introduced by

Mourjopoulos to yield better linear convolution results [1]. Further efforts have been made utilizing the Least-Squares Inversion to achieve better time domain linear deconvolution [2]. Later, a delayed version of the Least-Squares Inversion was introduced to enhance the linear deconvolution even further.

The various inversion research efforts mentioned here have only focused on the inversion based on a single point pressure. The spectral response varies greatly at different spatial positions. An inverse filter designed for one spatial location may not be beneficial for other locations; therefore complex smoothing methods were introduced in the past to lower the sensitivity of the spatial dependence in order to achieve a more global result. Nevertheless, while the method does smooth out the strong resonances and nulls associated with the specific spatial point of equalization, it also smoothes out the resonances and dips that are common to all field positions. (This includes loudspeaker spatial anomalies, spectral dips caused by the loudspeaker position and other global effects.) Often, the effects are less than adequate. A better way of achieving global equalization result is still needed.

This research will discuss the theories of implementing four different inversion algorithms (homomorphic inversion, weighted homomorphic inversion, least-squares inversion, and delayed least-squares inversion) applied to the single-point pressure equalization, spatially averaged pressure equalization, and finally single-point energy density equalization. Then a complex smoothing algorithm will also be explored and its spectral and spatial uniformity after equalization will be compared to that of the single-point pressure equalization without smoothing and energy density equalization. Finally, in order to quantify the uniformity of the equalized pressure field, both spectrally and spatially, a figure of merit, the global listening area

equalization coefficient (GLAEC) is introduced. This quantity assigns a single value to the equalized field to describe the spectral and spatial effectiveness of the equalization process..

3.1 Modeling the System Response

The system coloration at a desired location can be represented using the complex FRF.

$$H(\omega) = |H(\omega)| e^{j\phi(\omega)}, \tag{3. 1}$$

where $|H(\omega)|$ is the magnitude and $\phi(\omega)$ represents the phase of the FRF. Both variables are functions of the angular frequency ω. This FRF can be used to multiply the dry signal $X(\omega)$ in the frequency domain to obtain the colored signal:

$$Y(\omega) = H(\omega)X(\omega) = |H(\omega)||X(\omega)| e^{j\phi(\omega)+\phi_x(\omega)}, \tag{3. 2}$$

where $|X(\omega)|$ is the magnitude and $\phi_x(\omega)$ is the phase of the original signal response. The room-filtered signal can also be calculated in the time domain by convolving the original dry signal with the impulse response of the system:

$$y(t) = h(t) * x(t), \tag{3. 3}$$

where $h(t)$ is the impulse response of the room (FIG 3.1) and $x(t)$ is the original source signal in the time domain. Figure 3.1 shows the measured impulse response of a certain room.

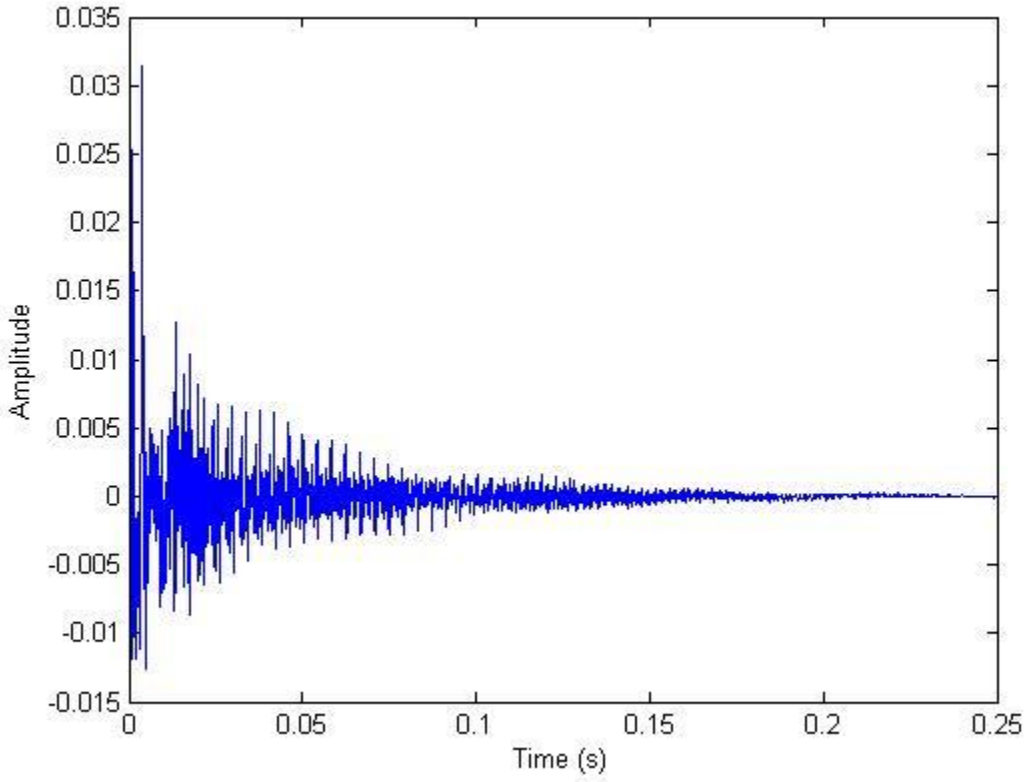

FIG. 3.1. Measured Impulse response of a room.

When the original signal $x(t)$ and $h(t)$ are of finite length, multiplication of their spectra in the frequency domain is not equivalent to the convolution of these two signals in the time domain. Rather, the signals in the time domain are repeated periodically in time from negative infinity to positive infinity and the linear convolution becomes a circular convolution [3]. Due to this difference a complete inversion performed in the frequency domain does not guarantee a complete deconvolution in the time domain.

3.2 Equalization Filter Design

3.2.1 Homomorphic Inverse Filter

Because a room response is typically nonminimum phase, an unstable inverse filter generally results from directly inverting this room response function. The stability of a filter can be best evaluated in the Z domain. For example, $H(z)$ is the Z transform of the mixed phase room response:

$$H(z) = \prod_{k=1}^{j}(1-a_k z^{-1}) \prod_{k=j+1}^{K}(1-b_k z^{-1}), \tag{3. 4}$$

where K is the filter length of the room response, $|a_k| < 1$ and $|b_k| > 1$. The factor involving $\prod_{k=1}^{j}(1-a_k z^{-1})$ represent the minimum phase portion of this mix phase room response while the factor involving $\prod_{k=j+1}^{N}(1-b_k z^{-1})$ represents the maximum phase portion. The direct inverse of this room response yields:

$$\begin{aligned} F(z) &= \frac{1}{\prod_{k=1}^{j}(1-a_k z^{-1}) \prod_{k=j+1}^{K}(1-b_k z^{-1})} \\ &= \prod_{k=1}^{j}(1+a_k z^{-1} + {a_k}^2 z^{-2} + \cdots) \times \prod_{k=j+1}^{K}(1+b_k z^{-1} + {b_k}^2 z^{-2} + \cdots) \end{aligned} \tag{3. 5}$$

The first term $\prod_{k=1}^{j}(1+a_k z^{-1}+{a_k}^2 z^{-2}+\cdots)$ converges because $|a_k|<1$; but the second term $\prod_{k=j+1}^{K}(1+b_k z^{-1}+{b_k}^2 z^{-2}+\cdots)$ diverges because $|b_k|>1$. The resulting inverse filter of this non-minimum phase response is acausal and unstable as illustrated in FIG 3.2.

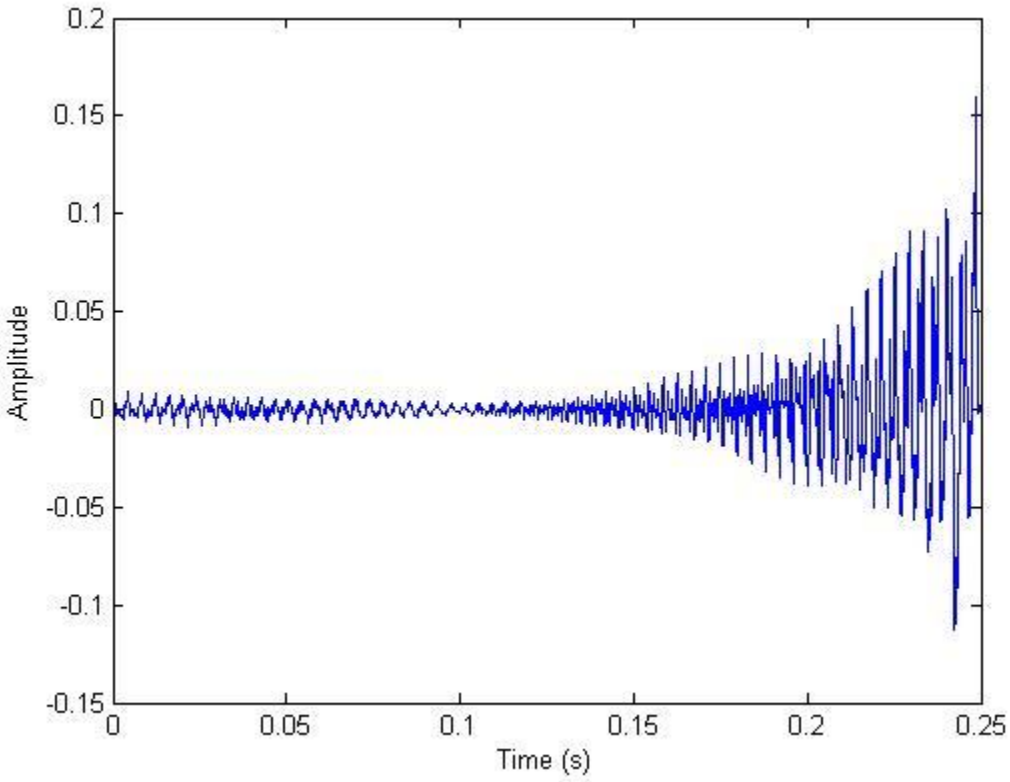

FIG. 3.2. Acausal inverse filter resulted from a non minimum phase response.

In addition, this inverse operator is infinite in length, even though the original room was finite in length. Furthermore, finite Discrete Fourier Transform will lead to aliasing from truncation [3].

One method to resolve the issues mentioned above is to invert the minimum phase portion of the room response only. A room frequency response function can be factored into the minimum phase response and the all-pass response:

$$H(\omega) = |H(\omega)| \exp[i\phi_m(\omega)] \exp[i\phi_a(\omega)], \tag{3. 6}$$

where $|H(\omega)| \exp[i\phi_m(\omega)]$ is the complex minimum phase response of the room and $\exp[i\phi_a(\omega)]$ is the non-minimum phase all-pass response . If the all-pass portion of does not simply represent a group delay, i.e.,

$$\tau = -[d\phi_a(\omega) / d\omega] \neq constant, \tag{3. 7}$$

the room frequency response can not be inverted directly to generate a causal and stable inverse filter. In order to derive a causal and stable inverse equalization filter, only the minimum phase part of the room frequency response should be inverted. For a given room FRF $H(\omega)$, the Hilbert Transform can be used to factor out the minimum phase portion from the total room response according to the following steps.

First, the discrete FRF $H(f)$ is computed by performing the discrete Fourier transform on the original discrete impulse response function $h(n)$. The cepstrum of the FRF is then calculated from the discrete frequency response function:

$$H(k) = DFT[h(n)] = \sum_{n=0}^{N-1} h(n) \exp(-\frac{2\pi i kn}{N}), \tag{3. 8}$$

$$C_p(n) = DFT^{-1}[\log|H(k)|] = \sum_{n=0}^{N-1} \log|H(k)| \exp(\frac{2\pi i k n}{N}), \quad \textbf{(3. 9)}$$

where $C_p(n)$ is the discrete cepstrum function of $h(n)$ and N is the total number of samples. The variable k is the discrete frequency variable, while DFT and DFT^{-1} represent the Discrete Fourier Transform and the Inverse Discrete Fourier Transform, respectively. This cepstrum is only a single sided function and needs to be turned into a two-sided cepstrum $\hat{m}(n)$.

$$m(n) = \begin{Bmatrix} C_p(n), n = 0, N/2 \\ 2C_p(n), 1 \le n < N/2 \\ 0, N/2 < n \le N-1 \end{Bmatrix} \quad \textbf{(3. 10)}$$

The minimum phase response can then be found by taking the exponential of the discrete Fourier transform of this double-sided ceptrum:

$$\begin{aligned} \theta(k) &= DFT[m(n)], \\ M(k) &= \exp[\theta(k)]. \end{aligned} \quad \textbf{(3. 11)}$$

An inverse equalization filter can then be found by inverting the non-zero data points of the minimum phase response:

$$\begin{aligned} H_{EQ}(k) &= \frac{1}{M(k)}, \\ h_{EQ}(n) &= DFT^{-1}[H_{EQ}(k)], \end{aligned} \quad \textbf{(3. 12)}$$

where $H_{EQ}(k)$ is the complex frequency response of the equalization filter, and $h_{EQ}(n)$ is the discrete impulse response function of the equalization filter, which should be purely real and causal.

Inaccuracies arise when zeros of $H(z)$ are too close to the unit circle in the Z domain; the Hilbert transform cannot give an accurate factorization to separate the minimum phase part and

non-minimum phase part of the function. Deconvolution in the time domain will thus deviate further from the ideal delta function impulse. A phase shift is needed to move these zeros farther away from the unit circle to achieve better results.

3.2.2 Exponential Weighting

Ambient noise in the measurement of the transfer function usually moves the zeros of $H(z)$ closer to the unit circle and factorization of the mixed phase response into the minimum phase portion and maximum phase portion becomes less accurate. An exponential weighting of the original impulse response can move these zeros further away from the unit circle:

$$h_w(n) = \alpha^n h(n), \tag{3. 13}$$

where $h_w(n)$ is the weighted response of the original impulse response $h(n)$ and α is a positive real number with magnitude less than 1. The resulting Z transform can be written as

$$H_w(z) = H(\alpha^{-1} z), \tag{3. 14}$$

As this equation indicates, the poles and zeros of the original response $H(z)$ are shifted radially by a factor of α^{-1}. If $H(z)$ has zeros close to the unit circle at a radius of $|z| = 1+\delta$, α can be defined as $e^{-\lambda}$ where $\lambda = \ln(1+\delta)$. The exponentially weighted impulse response then becomes

$$h_w(n) = e^{-\lambda n} h(n). \tag{3. 15}$$

The zeros between $1 < |z| < 1+\delta$ will be then fall inside the unit circle. The discrete frequency response function $H_w(k)$ of this weighted impulse response can follows the discrete Fourier transform:

$$H_w(k) = DFT[h_w(n)]. \quad \textbf{(3. 16)}$$

The minimum-phase portion of this weighted frequency response can be inverted to derive the equalization filter:

$$H_{wEQ}(k) = \frac{1}{M_w(k)} \quad \textbf{(3. 17)}$$

$$h_{wEQ}(n) = DFT^{-1}[H_{EQ}(k)] \quad \textbf{(3. 18)}$$

where $\hat{M}_w$ is the minimum phase portion of the frequency response $H_w(k)$, $\hat{H}_{wEQ}(k)$ is the frequency response of the equalization filter, and $h_{wEQ}(n)$ is the impulse response of the equalization filter. The convolution of this equalization filter and the original impulse response gives the deconvolution:

$$y(n) = h_{wEQ}(n) * h(n). \quad \textbf{(3. 19)}$$

The squared error between this deconvolved signal and a delta function reflects the "dryness" of the deconvolution.

$$I = \sum_n e^2(n) = \sum_n [\delta(n) - y(n)]^2 \quad \textbf{(3. 20)}$$

The smaller this error energy is, the closer the deconvolved signal is to the ideal delta function. A proper weighting factor λ can be chosen to minimize this error function. A weighted homomorphic equalization is performed based on the steps discussed above. Figure 3.3 shows the original impulse response that is to be equalized and the deconvolution result based on the homomorphic exponential weighting ($\lambda = 0.007$).

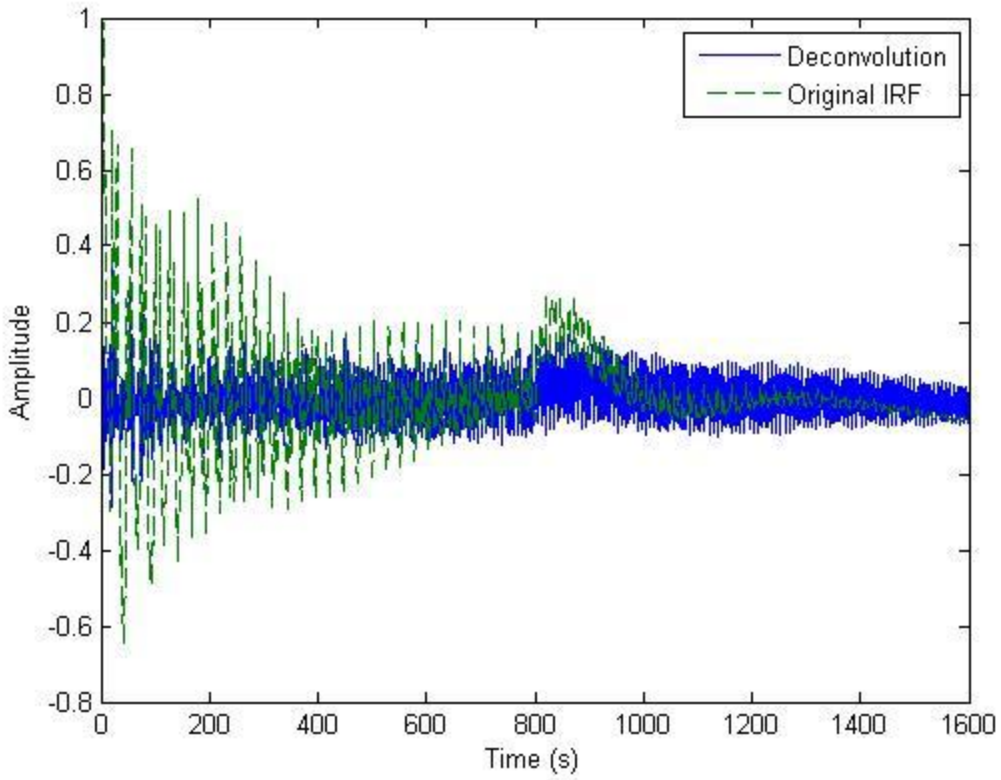

FIG. 3.3. Weighted Homomorphic Deconvolution.

The exact choice of λ depends on the number and locations of zeros near the unit circle. Figure 3.4 shows the error energy as a function of λ for this specific impulse response. This function is minimized at $\lambda = .007$. Compared to the non-weighted homomorphic inversion, this weighting reduces the error by a factor of 235.

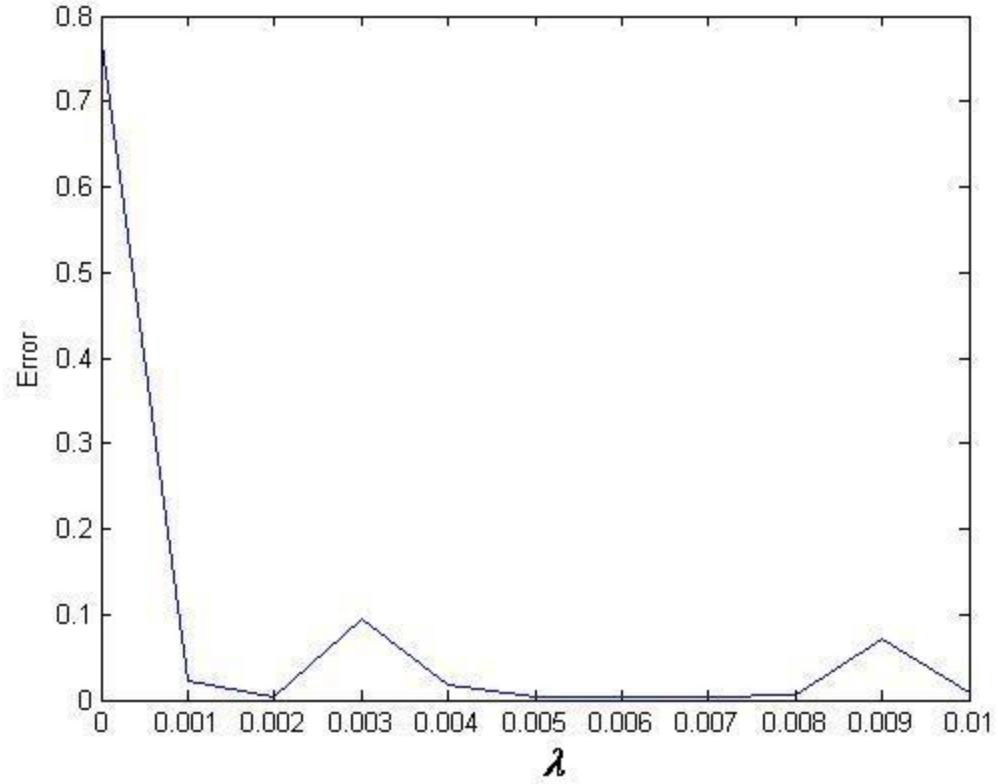

FIG. 3.4. Error energy as a function of the exponential weighting factor.

3.2.3 Least-Squares Inversion

While the homomorphic inversion is a frequency domain inversion, and in order to generate the best time domain deconvolution, an inverse filter can be found in the time domain directly from the original impulse response. The filter is designed to minimize the squared error in Eq. (3.17)., where $y(n)$ is the deconvolved signal:

$$y(n) = \sum_{i=0}^{N} f(i)h(n-i), \tag{3. 21}$$

$f(i)$ is the inverse filter, and $h(n)$ is the original discrete impulse response. An optimum set of coefficients $f(n)$ can be chosen to minimize the error function I. The solution of the N coefficients can be obtained from a set of $N+1$ linear equations,

$$Rf = g, \tag{3. 22}$$

where R is the autocorrelation matrix of the input signal $h(n)$, f is the coefficient array that is to be solved and g is the cross-correlation array between the input and the desired signal:

$$g(n) = \sum_{i=0}^{N} \delta(i)h(n+i), \tag{3. 23}$$

The solution to the coefficient array f can be solved using the matrix operation:

$$f = R^{-1}g \tag{3. 24}$$

The resulting filter f will always be a minimum phase filter but the performance of the inverse filter will be increased if the input filter h is of minimum phase. This matrix operation can also be solved more efficiently using the Levinson recursion algorithm [6].

3.2. 4 Delayed Least-Squares Inversion

Treitel and Robinson have shown that the performance of the least-squares inversion improves when a delay is introduced between the input signal and desired signal [3]. The error signal becomes

$$I_k = \sum_n [\delta(n-k) - y(n)]^2 \tag{3. 25}$$

when a sample delay k is introduced. The deconvolved signal becomes

$$y(n) = \sum_{i=0}^{N} f_k(i)h(n-i), \tag{3. 26}$$

where f_k is the delayed least-squares inverse filter. Coefficients $f_k(i)$ can be solved using the matrix operation

$$f_k = \frac{g_k}{R}, \tag{3. 27}$$

where R is the autocorrelation matrix of the input signal $h(n)$ and g_k is the cross-correlation array between the input and the delayed output:

$$g_k^T = [h(k), h(k-1)..h(0), 0, \ldots, 0]. \tag{3. 28}$$

The error function I_k should be a monotonically decreasing function of the delay k. The exact amount of delay k depends on the input signal h that is to be inverted. This delay can be determined using the Simpson sideward recursion [4]. The error function is determined at each of the delays k, and the recursion will be stopped when this error falls below the predetermined value,

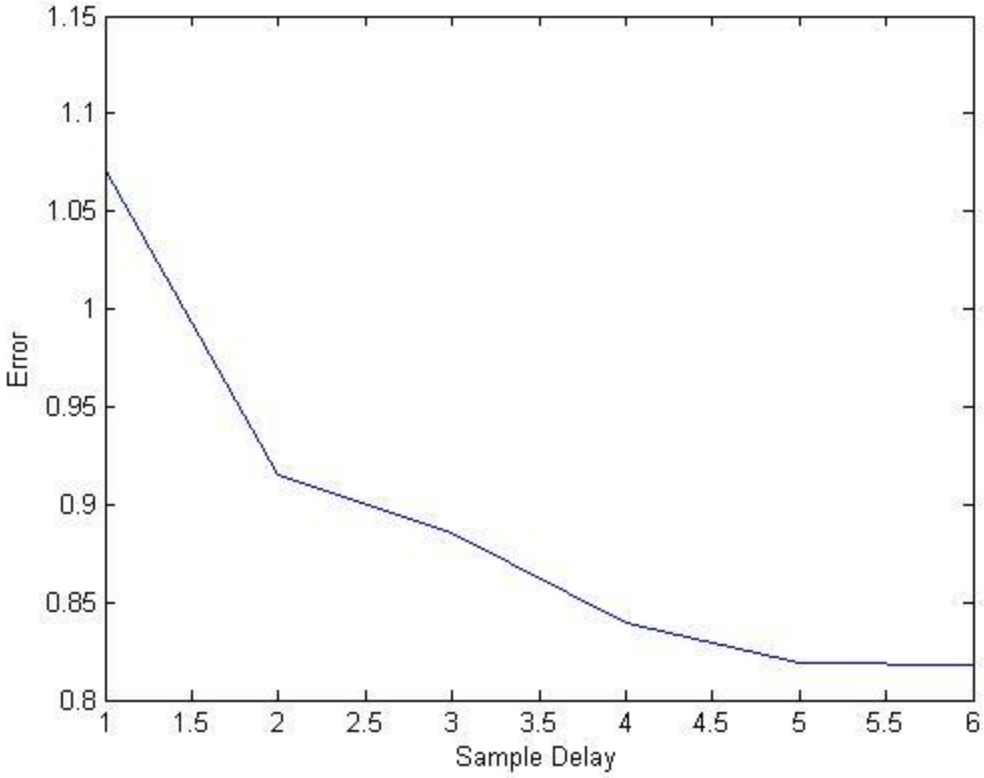

FIG. 3.5. Error Signal as a function of sample delay for least-square inversion.

Figure 3.5 shows the error as a function of sample delay. The error function drops to 80% of the initial value when 6 samples of delay are introduced between the input signal and the desired signal.

3.2.5 Complex Smoothing

The four algorithms discussed in the previous section can be applied to both single point pressure equalization and energy density equalization. For single point equalization, the input signal $h(n)$ is highly dependent upon the sensor location. In order to achieve more global

equalization results, complex smoothing can be applied on the measured input $h(n)$ signal before the inversion.

In the audio industry, it is has been considered acceptable to modify the measured impulse responses to match the perceived response of the human auditory system. Even though this processed response function differs from the measured response physically and mathematically, the psycho-acoustical corrections are accounted for by these modifications. Studies have shown that the frequency resolution sensitivity of the auditory system decreases as the frequency increases. Fractional-octave smoothing can be applied to the original frequency response to simulate this perception. Such a practice has been tested initially with the stochastic signals and later utilized on deterministic signals.

Another aim of complex smoothing is to achieve a more global result with inverse equalization. A challenging problem for room equalization is the spatial sensitivity of the inverse filter. An inverse equalization filter based on the spectrum at the "point of interest" may not yield a satisfactory result at other locations due to the spatial variations of the sound field. This variation is especially dramatic in the three-dimensional field. Smoothing of the spectrum can be applied to the original frequency response function at the point of interest. Then, the inverse equalization filter is then derived from this smoothed version. This smoothing decreases the sound level differences between the dips and peaks of the spectrum at different locations. This will in turn reduce the differences of the frequency response spectra at different locations. The resulting inverse filter will have lower position sensitivity and yield a more global response.

In most applications, the smoothing operation should retain the spectral properties of the original spectrum in each fractional-octave band. This corresponds to the magnitude properties of the power spectra before and after smoothing. It is equally important that the smoothing

operation not bring in any perceptible "time smearing" effects which correspond to changes in the phase response of the original spectrum. Traditionally, analog equipment like the one-third-octave filter-bank analyzer only allowed smoothing of the power spectrum. With contemporary digital processing technologies, algorithms can be developed to achieve complex smoothing that will simultaneously modify both magnitude and phase.

Performing a moving average over frequency will produce a smoothed version of the frequency response function. This frequency domain convolution corresponds to the time domain multiplication:

$$h_{cs}(n) = h(n) \cdot N \cdot w_{sm}(n); \quad o \le n < N, \tag{3. 29}$$

$$H_{cs}(k) = H(k) \otimes W_{sm}(k); \quad 0 \le k < N, \tag{3. 30}$$

where $h(n)$ is the discrete impulse response function of the room, $H(k)$ is the corresponding discrete frequency response function of the room, N is the total number of samples, $w_{sm}(n)$ is the smoothing window in the time domain, and $W_{sm}(k)$ is the smoothing function in the frequency domain. The symbol $\otimes$ denotes a circular convolution, $h_{cs}(n)$ is the smoothed impulse response, and $H_{cs}(k)$ is the smoothed frequency response function. Fractional octave complex smoothing can be computed similarly [8][9]:

$$\begin{aligned} H_{cs}(m,k) &= H(k) \otimes W_{sm}(m,k) \\ &= \sum_{i=0}^{N-1} W_{sm}(m,i) \quad H[(k-i) \bmod N], \end{aligned} \tag{3. 31}$$

where m is the smoothing index that represents the length of the frequency band, $W_{sm}(m,k)$ is the smoothing function for that particular band,

$$W_{sm}(m,k)=\begin{cases}\dfrac{b-(b-1)\cos[(\pi/m)k]}{2b(m+1)-1}; & k=0,1,\ldots,m,\\ \dfrac{b-(b-1)\cos[(\pi/m)(k-N)]}{2b(m+1)-1}; & k=N-m,N-(m-1),..N-1,\\ 0 & k=m+1,\ldots,N-(m+1),\end{cases} \quad \textbf{(3. 32)}$$

and where b is an arbitrary constant. As the DFT yields a symmetric half-window spectrum, this smoothing function is also symmetric around $N/2$, with the 2 half-windows located at $k=0..m$ and $k=N-m..N-1$, where $m\in 1,\ldots,M$ is the length of the half-window and where $M\le N/2$. The smoothing function W_{sm} can also be presented in a matrix form:

$$W_{sm}(m,k)=\begin{bmatrix} W_{sm}(1,0) & W_{sm}(1,1) & \cdots & W_{sm}(1,N-1)\\ W_{sm}(1,1) & W_{sm}(2,1) & \cdots & W_{sm}(2,N-1)\\ \vdots & \vdots & \ddots & \vdots\\ W_{sm}(M,0) & W_{sm}(M,1) & \cdots & W_{sm}(M,N-1)\end{bmatrix} \quad \textbf{(3. 33)}$$

For fractional octave band smoothing, m should be a function of k. The discrete function of the bandwidth for the fractional octave band is

$$P_d(k)=f_U-f_L, \quad \textbf{(3. 34)}$$

where,

$$f_U=2^{\frac{1}{2Q}}\frac{kf_s}{N} \quad \textbf{(3. 35)}$$

$$f_L=2^{-\frac{1}{2Q}}\frac{kf_s}{N} \quad \textbf{(3. 36)}$$

are the upper and lower frequencies of the 1/Q th fractional octave band and f_s is the sampling frequency. Therefore, the smoothing index can be represented as

$$m(k)=\begin{cases}\dfrac{1}{2}\dfrac{P_d(k)}{f_s}; & 0\le k\le \dfrac{N}{2}\\ \dfrac{1}{2}\dfrac{P_d(k)N}{f_s}; & \dfrac{N}{2}+1\le k\le N-1\end{cases}, \tag{3. 37}$$

Fractional-octave band complex smoothing can be performed in the time domain:

$$h_{cs}(n)=2\sum_{k=0}^{N/2} IFFT\left[FFT(h(n)\cdot w[m(k),n])\cdot FFT(c^k)\right] \tag{3. 38}$$

where $c^k=\cos[(2\pi/N)nk]$ and $w[m(k),n]$ can be calculated from $W_{sm}(m(k),k)$ using the DFT:

$$w[m(k),n]=DFT^{-1}[W_{sm}(m,k)] \tag{3. 39}$$

As shown in Fig. 3.6, the smoothed signal $h_{cs}(n)$ decays much faster than the original signal $h(n)$ in the time domain. The variations between the resonances and dips of the frequency domain response H_{cs} are also much less than those of the original response $H(k)$ (see FIG. 3.7).

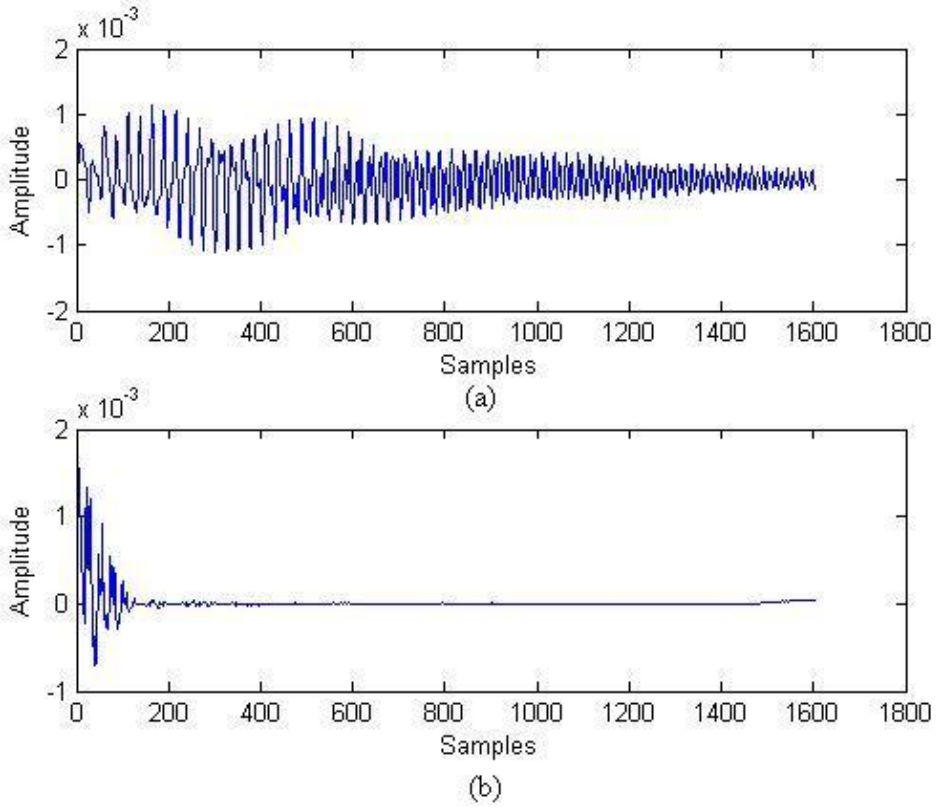

FIG. 3. 6. a) Original Impulse Response b) The smoothed impulse response.

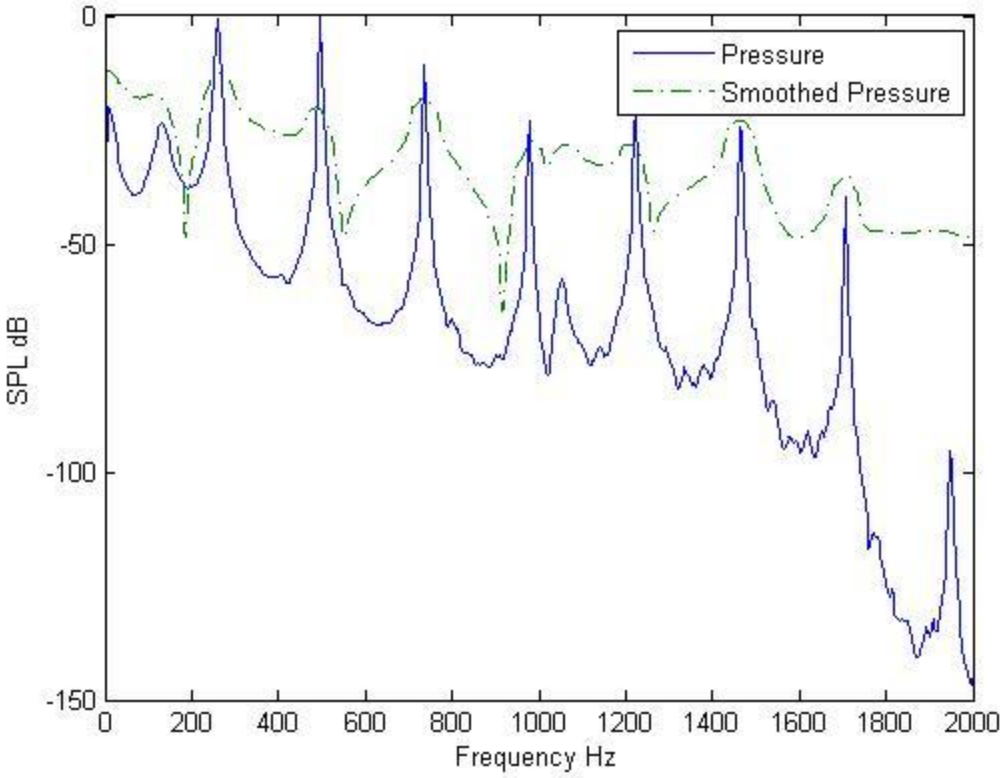

FIG. 3.7. Smoothed response v.s. original frequency response.

3.3 Deconvolution Using the Equalization Filter

3.3.1 Basic Theory

Before the original source signal is transmitted into the listening environment through the amplification and loudspeakers, the dry signal $x(t)$ is linearly convolved with the equalization filter $h_{EQ}(t)$.

$$x_{EQ}(t) = x(t) * h_{EQ}(t), \tag{3. 40}$$

where $x_{EQ}(t)$ is the equalized source signal. This equalized signal is then transmitted into the listening environment, which is equivalent to convolving the equalized signal with the room response $h(t)$:

$$y(t) = x_{EQ}(t) * h(t) = x(t) * h_{EQ}(t) * h(t). \quad \textbf{(3. 41)}$$

To ideally remove the room coloration, the equalization filter should deconvolve the room impulse response:

$$h_{EQ}(t) * h(t) = \delta(t - t_0), \quad \textbf{(3. 42)}$$

where t_0 is the delay that results from the deconvolution process. This inverse filter can be derived based on a single point pressure or a single point energy density.

3.3. 2 Experimental Implementation

3.3.2.1 Frequency Domain Equalization

Equalization filters can be applied to a signal theoretically in the frequency domain. This is equivalent to the circular convolution of the inverse filter with the signal in the time domain. The purpose of this practice is to compare the quality of the inverse filters spectrally over the listening area. For the experimental implementation, a one dimensional duct with the length 74.7 cm is used. Fourteen sample locations were evenly spaced along the tube at 5 cm intervals. A loudspeaker was located at one end of the tube (at x=0) which was rigidly terminated. The first microphone position was 3.2 cm away from the loudspeaker.

Homomorpic and weighted homomorphic inverse filters share the same magnitude but different phases in the frequency domain. For the frequency domain inversion (or circular convolution in the time domain), these two filters yield the flattest magnitude response. Each of

the three quantities of interest (single point pressure, spatially averaged pressure, and single point energy density) were inverted using the homomorphic method. First the one dimensional pressure field along the duct was equalized based on the point pressure at location 5 (22.35 cm from the source).

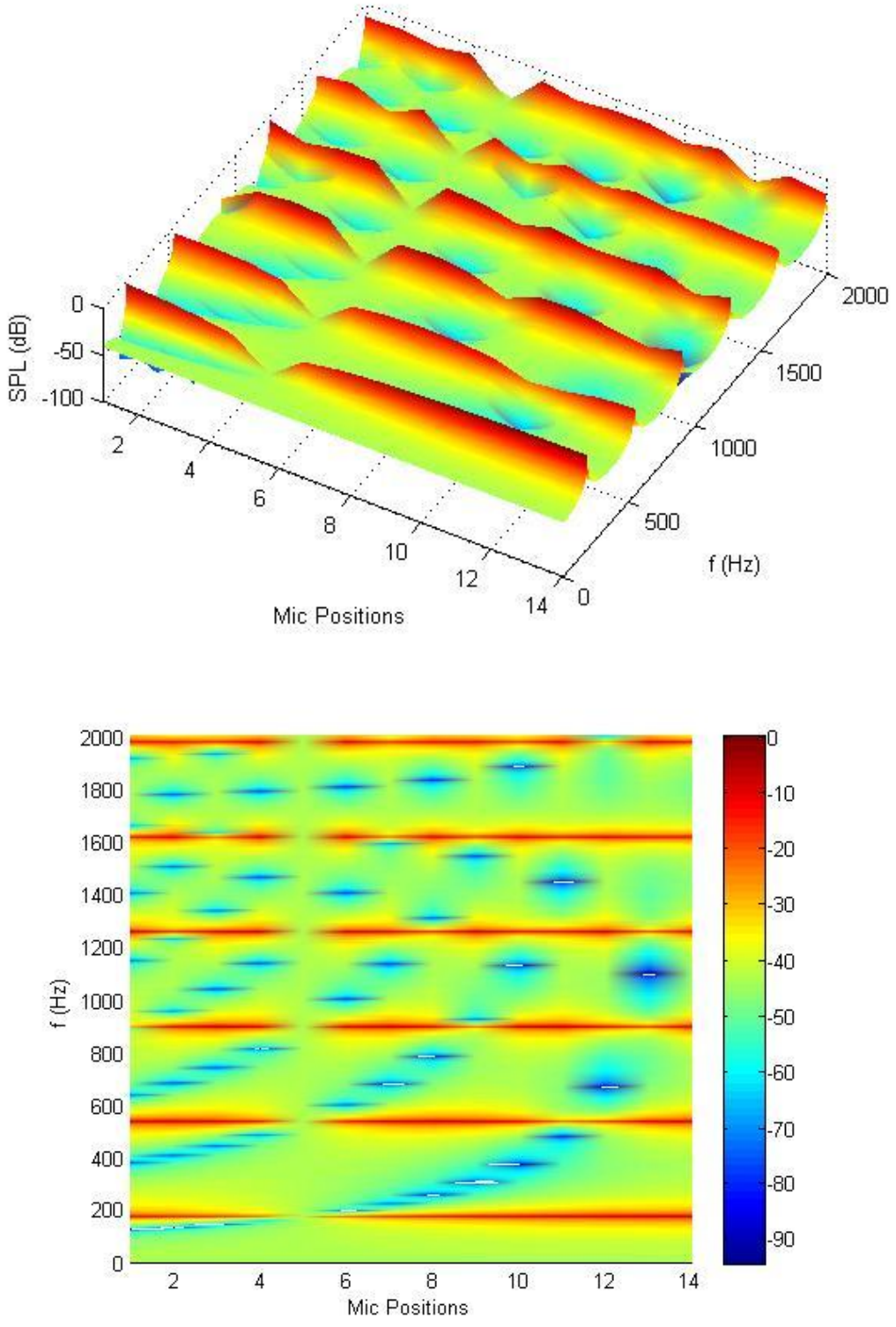

FIG. 3.8. Single-point pressure equalization.

In Fig. 3.8, the x axis shows the spatial locations of the sensors, the y axis shows the frequency and the z axis shows the normalized pressure level on a log scale. Because of the strong dependence of the field over space, single point pressure equalization yielded a flat spectrum at the sensor location, but not at other locations. In order to generate more global equalization results, the equalization filter should be based on spatially averaged squared pressure. This quantity takes the average of squared pressures at different spatial locations (See Fig. 3.9). The Spatially averaged squared pressure only cuts off the resonance peaks common to all sensor locations and it will not boost the spectral dips that are unique to a single location. This yields a much more global result in the listening area than the single-point pressure equalization. However, the pitfall of the equalization scheme is that measuring the spatially averaged pressure requires a large amount of pressure field samples. This becomes impractical when the listening area is large

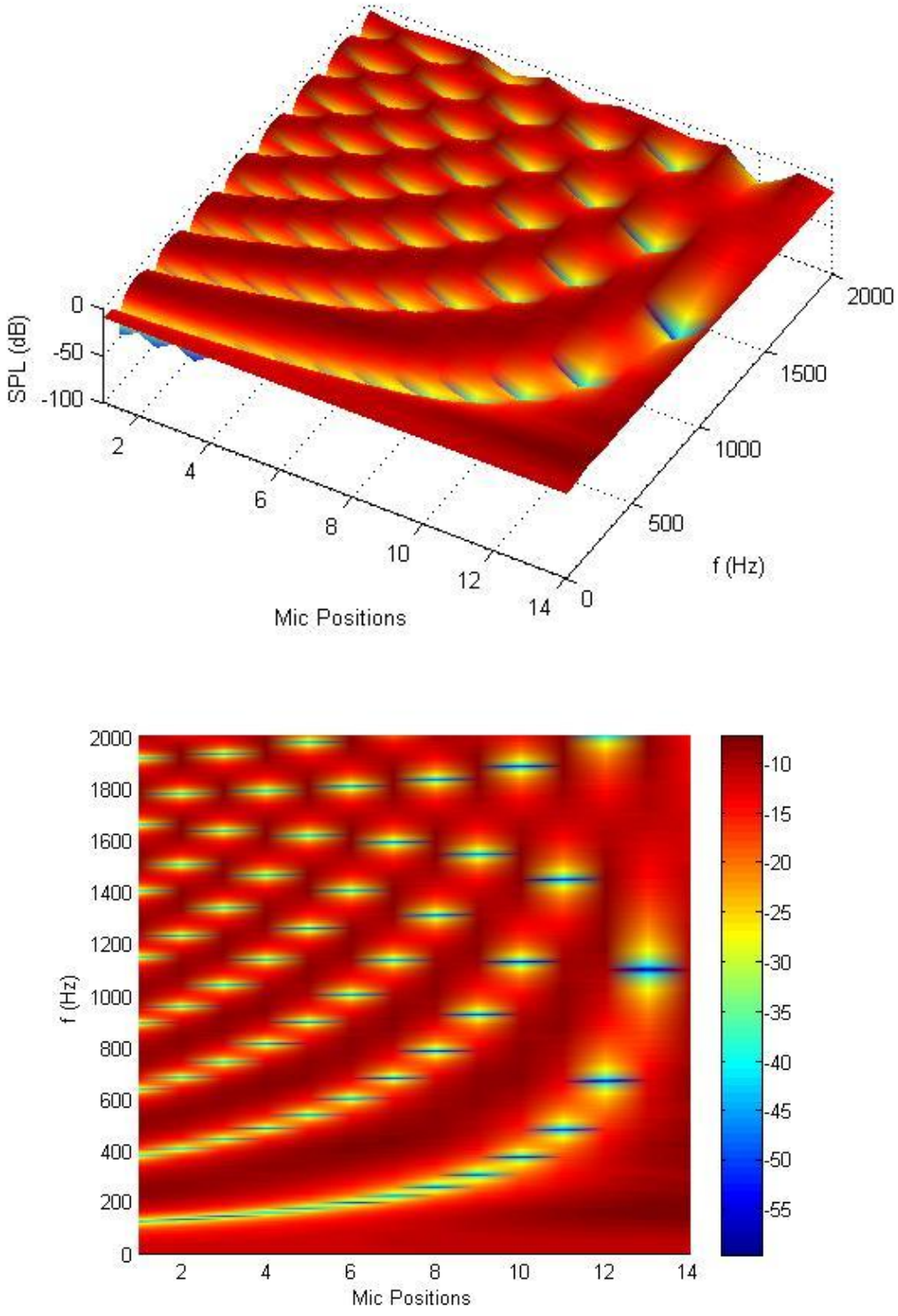

FIG. 3.9. Spatially averaged pressure equalization.

Other physics quantities that require fewer sample points and can still result in a more global result than single point pressure should be selected to derive the equalization filter. It has been shown that single point energy density in a one-dimensional tube shares similar spectral properties to that of the spatially averaged pressure. As a result, a single point energy density inverse filter gives a more global result over the whole length of the tube similar to the field equalized by the spatially averaged pressure (see Fig. 3.10):

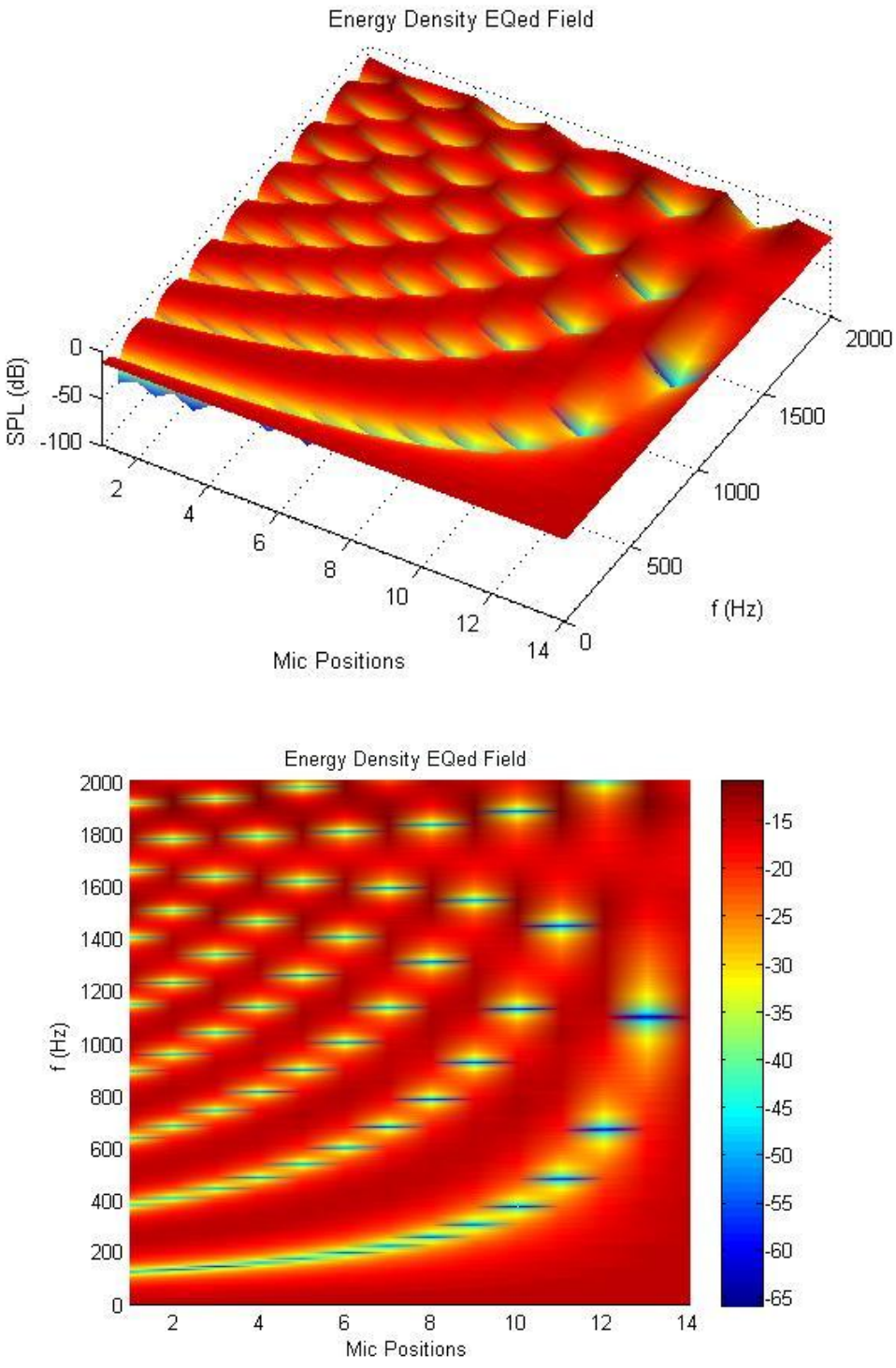

FIG. 3.10. Single-point energy density equalization.

Another approach that has been implemented to achieve a more global equalization result in the past is the smoothed pressure equalization filter. This technique reduces the difference in level between the spectral peaks and dips in order to lower the sensitive of the spectral dependence on spatial locations. As a result, the smoothed pressure will not completely correct the spectral variance at the point of equalization but it will yield smoother equalization results at other field positions. (see Fig. 3.11)

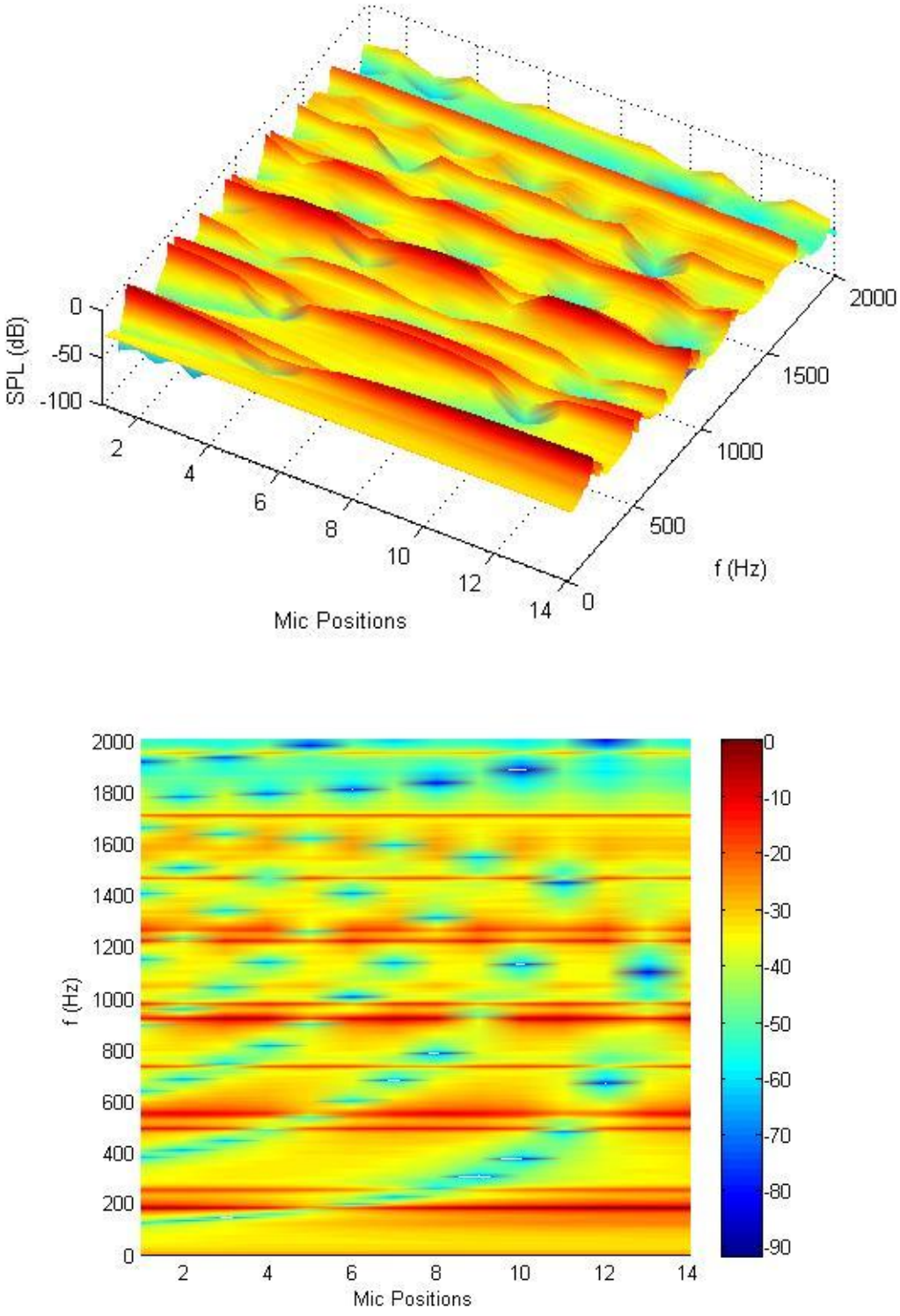

FIG. 3.11. Smoothed single-point pressure equalization.

As shown in the figure, the sensor point (location 5) does not have a flat spectrum due to the fact that the inverse point pressure does not correct the peaks and dips to their full extend after smoothing. However, this smoothed inverse pressure equalization gives better equalization results at other field locations compared to the unsmoothed inverse pressure equalization.

3.3.2.2 Time Domain Equalization

In practical applications, the source signal is filtered in the time domain first before being transmitted into the listening environment. The inverse filters derived in the frequency domain will not give a perfect deconvolution when applied in the time domain as a linear convolution. As mentioned in Section II-3, an inverse filter derived in the time domain using the least-squares method gives better results than the homomorphic methods when the linear convolution is applied. Figure 3.12 shows the deconvolution done by the single-point pressure equalization at the same location (location 5) using least-squares inversion, delayed least-squares inversion, homomorphic inversion, and weighted homomorphic inversion. As stated earlier, delayed least-squares method yields the driest deconvolution among the four schemes. Similar steps can be taken on the single point energy density equalization (see FIG. 3.12). The pressure field is equalized by the energy density sampled at location 5. Again this result shows that the delayed Least-Squares inversion gives the best deconvolution results.

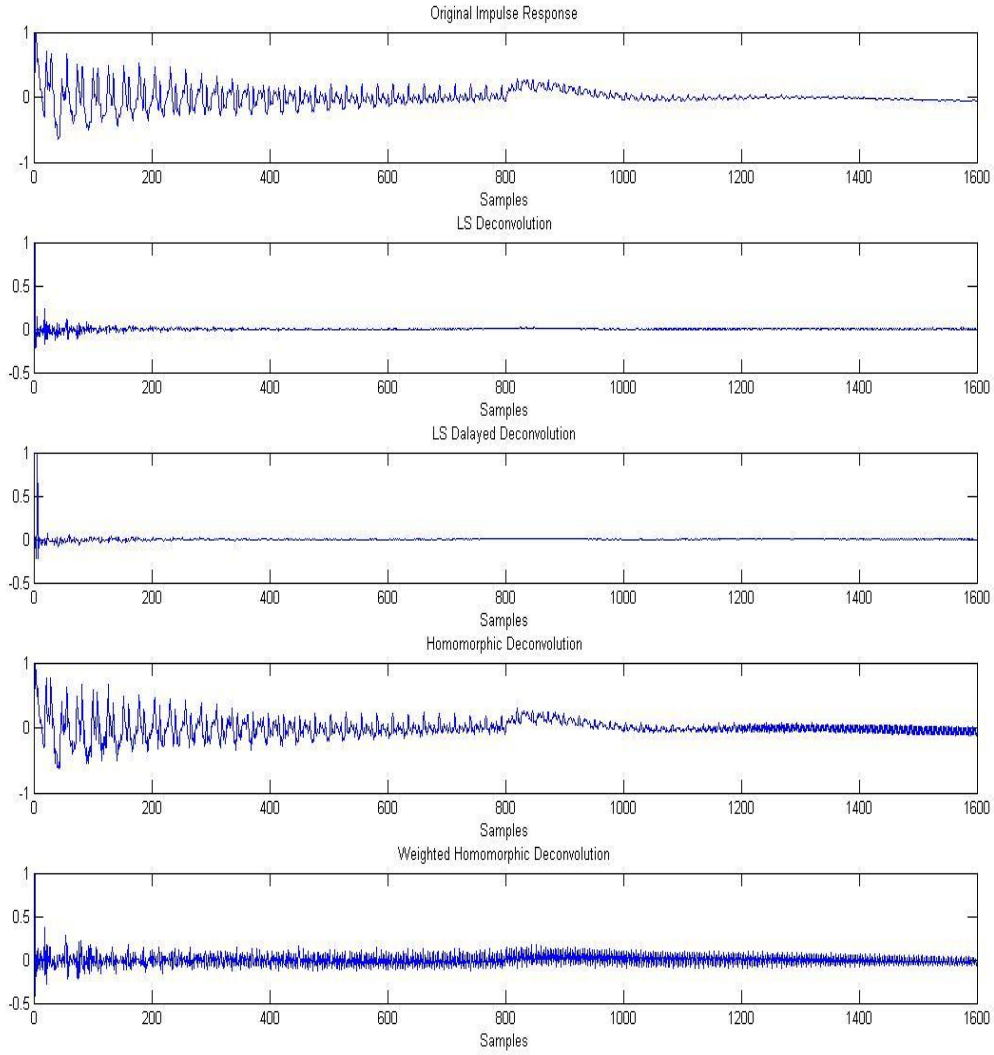

FIG. 3.12. Comparison of different equalization schemes.

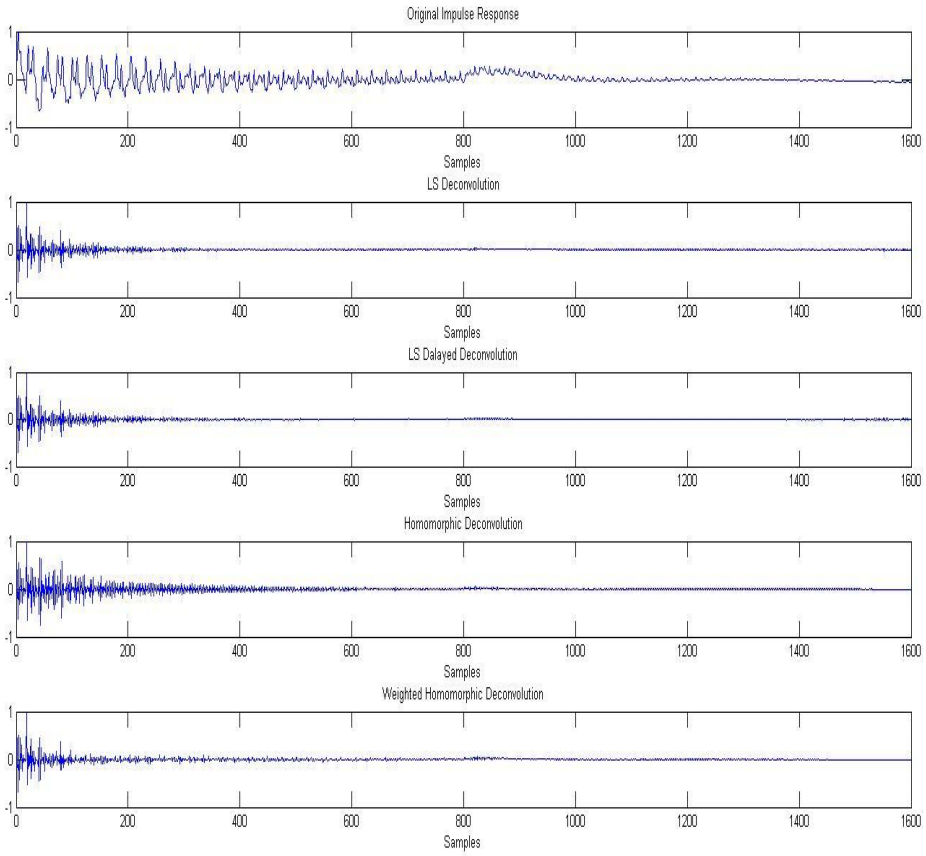

FIG. 3.13. Point energy density equalization using different equalization schemes.

3.4 Global Listening Area Equalization Coefficient

A figure of merit should be developed to reflect the uniformity of both the spectral response and the spatial response. This figure should reach its minimum value when the field is uniform in both frequency and space; it should increase as the field becomes more varied.

Because of its ability to achieve the best global equalization result, the spatially averaged pressure equalization should result in the minimum value for the figure of merit. A global

listening-area coefficient (GLAEC) can be defined as the spectral standard deviation of the spatially averaged spectrum of the field.

$$GLAEC = \frac{1}{N}\sum_{n=1}^{N}\{P_{spavg}(n)/\max[P_{spavg}(n)] - \frac{1}{N}\sum_{n=1}^{N}P_{spavg}(n)/\max[P_{spavg}(n)]\}^2, \quad \textbf{(3. 43)}$$

where $P_{spavg}(n)$ is the spatially averaged pressure,

$$P_{spavg}(n) = \sqrt{\frac{1}{M}\sum_{k=1}^{M}P(n,k)^2}, \quad \textbf{(3. 44)}$$

and N is the totally number of data points of the spatially averaged pressure, M is the total number of sensor locations. The GLAEC can be calculated after the field is equalized by the single point pressure, spatially averaged pressure smoothed single pressure and energy density. The results are shown in Fig. 3.14.

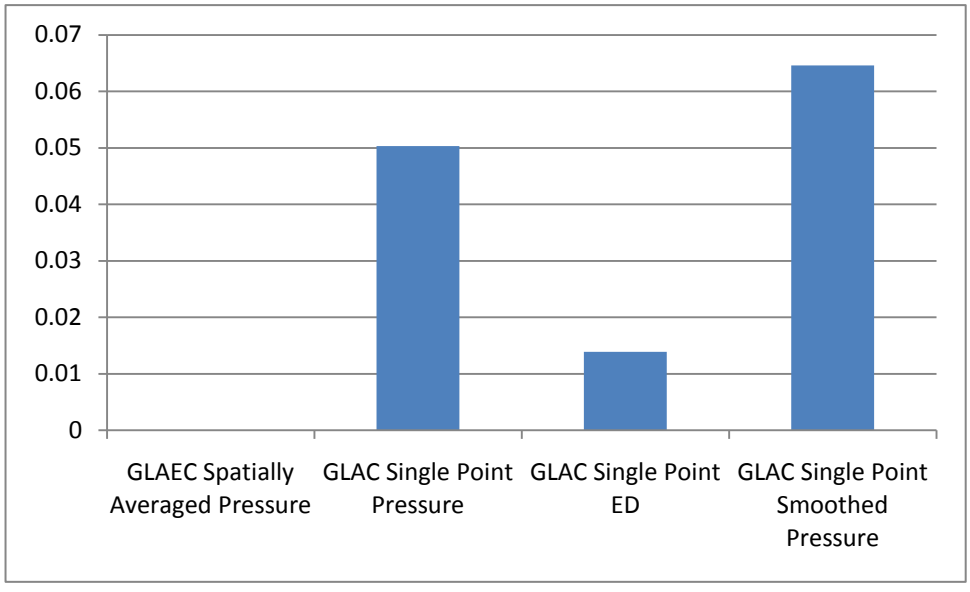

FIG. 3.14. GLAEC of different equalization schemes.

The result shows that the derived GLAEC gives 0 value for spatially averaged pressure. Energy density equalization gives the next best result over frequency and space.

3.5 Conclusion

This Chapter has discussed the theory and implementations of the four different equalization inversion schemes: homomorphic inversion, weighted homomorphic inversion, least-squares inversion and the delayed least-squares inversion. It has been shown that the delayed least-squares inversion gives the best result for the time domain deconvolution. Four different physical quantities have been used to generate the inverse equalization filters: single point pressure, spatially averaged pressure, single point smoothed pressure and single point energy density. While giving the best equalization result at the sensor location, single point pressure brings more spectral distortion to other spatial locations. Spatially averaged pressure equalization gives the most global result over the entire listening area, but it is often impractical to measure. Single-point smoothed pressure does remove some of the spatial dependency of the equalized field but its performance is still not satisfactory. Single point energy density equalization yields the closest result to that of the spatially averaged pressure equalization but it is much more practical due to the small number of sampling locations required (one probe location is sufficient for the one-dimensional sound field). Overall, the best equalization scheme is to use the delayed least-squares inversion of the single point energy density to achieve the best equalization result.

The introduction of the global listening area equalization coefficient provides a method to quantify the uniformity of the equalized pressure field. Based on this simple figure of merit, different equalization schemes can be compared to select the best approach.

References

[1] J. Mourjopoulos, P.M. Clarkson and J.K. Hammon, "A Comparative Study of Least-Squares and Homomorphic Techniques For The Inversion of Mixed Phase Signals"

[2] P.M. Clarkson, J. Mourjopoulos, and J.K. Hammon, "Spectral, Phase, and Transient Equalization for Audio Systems," J. Audio Eng. Soc., Vol 33, No. 3, 1985 March, (127-132)

[3] A.V. Oppenheim and R. W. Schaffer, *Digital Signal Processing*, (Prentice-Hall, Englewood Cliffs, NJ, 1975).

[4] S. Treitel and E.Robinson "The design of high resolution digital filters," IEEE Trans. Geosci. Electron. VGE-4, 1966, pp. 25-38

[5] S. M. Simpson. "Recursive Schemes for normal equations of Toeplitz form". Chapter 4 of Scientific Report No. 7 of Contract AF 19 (604) 7378, ARPA Project, VELA_UNIFORM, MIT, Cambridge, Mass. 1963

[6] Stephen T. Neely and Jont B. Allen, "Invertibility of a Room Impulse Response," J. Acoust. Soc. Am. 66 (1), July 1979 (165-169)

[7] Ryan Chester, *Error Sensor Strategies for Active Noise control and Active Acoustic Equalization in a Free Field,* (M. S. Thesis, Brigham Young University, 2008)

Chapter 4

One-dimensional sound field with a source on the side

4.1 Introduction

Chapter 2 has discussed the modeling of the pressure, particle velocity, and energy density field inside a one-dimensional tube with a loudspeaker at the end. This chapter explores the one-dimensional fields in a tube with a source on the side.

A simple one-dimensional sound reproduction system setup includes a signal source, amplification, a loudspeaker and a one-dimensional plane-wave tube. The cross-section of the duct is small enough to assure that all the cross-modes within the frequency range of interest are evanescent and only plane waves propagate inside of the duct away from the loudspeaker. There are two essential factors that contribute to the total coloration of the source signal at a certain location inside the duct: (1) the overall transfer function of the electro-acoustical components and (2) the transfer function between the source and the listening position inside of the duct. The first factor is not spatially dependent, while the latter depends on the location of the loudspeaker position as well as the listening position.

The following sections introduce several theoretical modeling tests for the one-dimensional field variables. They also compare the models to experimental results and show the effects of equalization.

4.2 Theoretical modeling of the one-dimensional sound field with a loudspeaker on the side

A one-dimensional pressure field can be modeled using the Helmholtz equation. The solution needs to satisfy the second-order differential equation as well as the boundary conditions. For the one-dimensional field, this solution is of closed form. The particle velocity field can be derived using Euler's equation.

A one-dimensional field can be excited in a plane wave tube with cross-sectional dimensions much smaller than the wavelength. As shown in Fig. 4.1, the ends of the duct are loaded with acoustic impedances Z_{A1} and Z_{A2}. A plane wave monopole source is placed at a desired location in the duct to excite the sound field [1].

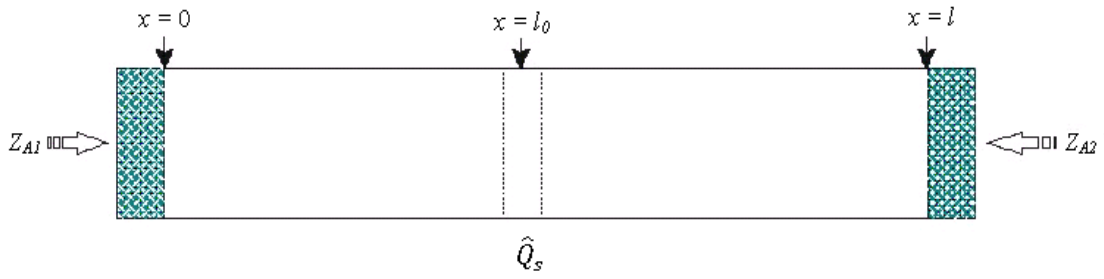

FIG. 4.1. A theoretical one dimensional tube model. The tube is terminated at *x=0* and *x=l* with acoustic impedances Z_{A1} and Z_{A2} respectively. The sound field is excited by a plane monopole source at $x=l_0$.

To satisfy the Helmholtz equation and its boundary conditions:

$$\nabla^2 \hat{p} + k^2 \hat{p} = 0, \tag{4. 1}$$

$$\left. \frac{\hat{p}}{S\hat{u}} \right|_{x=0} = Z_{A1}, \tag{4. 2}$$

$$\left.\frac{\hat{p}}{S\hat{u}}\right|_{x=l} = Z_{A2}, \tag{4. 3}$$

$$\left.\hat{u}\right|_{x=l_0} = \frac{\hat{Q}_s}{S}, \tag{4. 4}$$

where $\hat{p}$ is the complex pressure amplitude of the field, $\hat{u}$ is the complex particle velocity amplitude and Z_{A1} and Z_{A2} are the acoustic impedances at each end of the duct. The variable $\hat{Q}_s$ is the source strength, S is the cross-sectional area of the duct, l is the length of the tube, l_0 is the source location, and k is the wave number. There are essentially three boundary conditions associated with configuration: the pressure to volume velocity ratios need to be equal to the two end acoustic impedances, and the volume velocity of the field at the source location needs to be equal to the source strength.

4.2.1 Solution using modal expansion

The solution to this boundary-value model can be expressed in terms of the summation of an infinite number of eigenfunctions. The eigenfunctions are a complete set of orthogonal functions that satisfy the homogeneous Helmholtz equation and the two boundary conditions at each end of the tube. A solution for this eigenfunction set can be determined from the general pressure solution

$$\psi_N = \hat{p} = A_N \cos(k_N x) + B_N \sin(k_N x), \tag{4. 5}$$

And for particle velocity,

$$\hat{u} = \frac{j}{\rho_0 c}[-A_N \sin(k_N x) + B_N \cos(k_N x)], \tag{4. 6}$$

where A_N and B_N are two arbitrary constants which can be derived from the boundary conditions, k_N is the allowed wave numbers associated with the N[th] eigenfunction, ρ_0 is the ambient density of air, and c is speed of sound. In order for the field to match the boundary conditions on the two ends of the duct, the constant coefficients A_N and B_N must satisfy:

$$\left.\frac{\hat{p}}{S\hat{u}}\right|_{x=0} = \frac{\rho_0 c}{jS}\left[\frac{A_N}{B_N}\right] = Z_{A1}, \tag{4. 7}$$

$$\left.\frac{\hat{p}}{S\hat{u}}\right|_{x=l} = \frac{\rho_0 c}{jS}\left[\frac{A_N \cos(k_N l) + B_N \sin(k_N l)}{-A_N \sin(k_N l) + B_N \cos(k_N l)}\right] = Z_{A2}. \tag{4 . 8}$$

The unknown coefficients A_N and B_N can be solved from equations (4.4) and the pressure can be written as an expansion of the eigenmodes:

$$\hat{p} = j\rho_0 ck\hat{Q}_s \sum_{N=0}^{\infty} \frac{\psi_N(l_0)\psi_N(x)}{(k^2 - k_N^2)l}, \tag{4. 9}$$

Where $k_N = \frac{n\pi}{l}$, l_0 is the source location, $\psi_N(x)$ are the eigenfunctions that satisfy the Helmholtz equation and the boundary conditions.

4.2.2 Solution using Green's function:

For the one-dimensional field, there is a unique closed form solution. The Green's function can be used in this situation to solve the second order differential equation. Instead of treating the source as one of the boundary conditions, a delta function can be introduced to the right side of the homogeneous Helmholtz equation to represent the source:

$$\nabla^2 \hat{p} + k^2 \hat{p} = -4\pi k^2 \hat{Q}_s \delta(k(x-l_0)) = -4\pi k \hat{Q}_s \delta(x-l_0), \tag{4. 10}$$

$$\left.\frac{\hat{p}}{S\hat{u}}\right|_{x=0} = Z_{A1}, \tag{4. 11}$$

$$\left.\frac{\hat{p}}{S\hat{u}}\right|_{x=l} = Z_{A2}. \tag{4. 12}$$

The Green's function is the solution to the non-homogeneous Helmholtz equation:

$$\nabla^2 G + k^2 G = -\delta(x-\xi) \tag{4. 13}$$

where x is the field position and ξ is the position variable along the duct which varies from 0 to l. The pressure can be calculated from the integration of the Green's function:

$$\hat{p}(x) = \int_0^l G(x,\xi)[-4\pi\delta(\xi - l_0)]d\xi \tag{4. 14}$$

Assume $\hat{p}_1(x)$ is a solution which satisfies the left side boundary condition, and $\hat{p}_2(x)$ is a solution which satisfies the right side B.C. The Green's function can be written in terms of these 2 functions:

$$G(x,\xi) = \begin{cases} c_1 p_1(x); & 0 \le x < l_0 \\ c_2 p_2(x); & l_0 \le x \le l \end{cases} \tag{4. 15}$$

At location ξ, the Green's function needs to satisfy the boundary condition:

$$c_2 \hat{p}_2(\xi) - c_1 \hat{p}_1(\xi) = 0, \tag{4. 16}$$

$$c_2 \hat{p}_2'(\xi) - c_1 \hat{p}_1'(\xi) = -1. \tag{4. 17}$$

In order to have a nontrivial solution,

$$\begin{vmatrix} \hat{p}_1(\xi) & \hat{p}_2(\xi) \\ \hat{p}_1'(\xi) & \hat{p}_2'(\xi) \end{vmatrix} \neq 0 \tag{4. 18}$$

Solving equations (4.15) through (4.18),

$$G(x,\xi)=\begin{cases}\dfrac{-1}{[\hat{p}_1'(\xi)\hat{p}_2(\xi)-\hat{p}_1(\xi)\hat{p}_2'(\xi)}\hat{p}_1(x)\hat{p}_2(\xi); & 0\le x<\xi\\ \dfrac{-1}{[\hat{p}_1'(\xi)\hat{p}_2(\xi)-\hat{p}_1(\xi)\hat{p}_2'(\xi)}\hat{p}_1(\xi)\hat{p}_2(x); & \xi\le x<l\end{cases} \tag{4. 19}$$

where $\hat{p}_1'(\xi)=\dfrac{d}{dx}\hat{p}_1(x)\Big|_{x=\xi}$, $\hat{p}_2'(\xi)=\dfrac{d}{dx}\hat{p}_2(x)\Big|_{x=\xi}$

The pressure solution can be derived by integrating the Green's function using equation (4.14):

$$\hat{p}(x)=\begin{cases}\dfrac{4\pi}{[\hat{p}_1'(l_0)\hat{p}_2(l_0)-\hat{p}_1(l_0)\hat{p}_2'(l_0)}\hat{p}_2(l_0)\hat{p}_1(x); & 0\le x<l_0\\ \dfrac{4\pi}{[\hat{p}_1'(l_0)\hat{p}_2(l_0)-\hat{p}_1(l_0)\hat{p}_2'(l_0)}\hat{p}_1(l_0)\hat{p}_2(x); & l_0\le x<l\end{cases} \tag{4. 20}$$

To obtain the final solution, $\hat{p}_1(x)$ and $\hat{p}_2(x)$ must be determined from the homogeneous equations

$$\begin{cases}\nabla^2\hat{p}_1+k^2\hat{p}_1=0\\ \left.\dfrac{\hat{p}_1}{S\hat{u}_1}\right|_{x=0}=Z_{A1}\end{cases} \tag{4. 21}$$

and

$$\begin{cases}\nabla^2\hat{p}_2+k^2\hat{p}_2=0\\ \left.\dfrac{\hat{p}_2}{s\hat{u}_2}\right|_{x=l}=Z_{A2}\end{cases} \tag{4. 22}$$

Assume the solution

$$\hat{p}_1=A\sin(kx)+B\cos(kx), \tag{4. 23}$$

where coefficients A and B are two arbitrary coefficients yet to be determined. At the boundary x = 0, the solution needs to satisfy the boundary condition:

$$\frac{\hat{p}_1}{\hat{u}_1 S}=Z_{A1} \tag{4. 24}$$

Coefficients A and B can be solved from equations (4.23) and (4.24):

$$\frac{B}{A} = \frac{jZ_{A1}}{\frac{\rho_0 c}{S}}, \tag{4. 25}$$

$$\hat{p}_1 = A[\sin(kx) + \frac{jZ_{A1}}{\rho_0 c / s}\cos(kx)]. \tag{4. 26}$$

Similarly, $\hat{p}_2$ can be found using the boundary condition at $x = l$

$$p_2 = A[\sin(kx) + \frac{\frac{Z_{A2}\, j}{\rho_0 c / S}\cos(kl) - \sin(kl)}{\frac{Z_{A2}\, j}{\rho_0 c / S}\sin(kl) + \cos(kl)}\cos(kx)] \tag{4. 27}$$

A closed form solution of the pressure field can be derived by substituting $\hat{p}_1$ and $\hat{p}_2$ back into equation (4.20).

When $0 \le x < l_0$,

$$\hat{p}(x,f)=\frac{4\pi kA}{\left[k\cos(kl_0)-\frac{jZ_{A1}}{\rho_0 c/S}k\sin(kl_0)\right]\left[\sin(kl_0)+\frac{\frac{Z_{A2}j}{\rho_0 c/S}\cos(kl)-\sin(kl)}{\frac{Z_{A2}j}{\rho_0 c/S}\sin(kl)+\cos(kl)}\cos(kl_0)\right]}\frac{p_2(l_0)p_1(x)}{\left[\sin(kl_0)+\frac{jZ_{A1}}{\rho_0 c/S}\cos(kl_0)\right]\left[k\cos(kl_0)-k\frac{\frac{Z_{A2}j}{\rho_0 c/S}\cos(kl)-\sin(kl)}{\frac{Z_{A2}j}{\rho_0 c/S}\sin(kl)+\cos(kl)}\sin(kl_0)\right]}$$

$$=\frac{4\pi}{\left\{\frac{-jZ_{A1}}{\rho_0 c/S}+\frac{\frac{Z_{A2}j}{\rho_0 c/S}\cos(kl)-\sin(kl)}{\frac{Z_{A2}j}{\rho_0 c/S}\sin(kl)+\cos(kl)}\right\}}\left\{\sin(kl_0)+\frac{\frac{Z_{A2}j}{\rho_0 c/S}\cos(kl)-\sin(kl)}{\frac{Z_{A2}j}{\rho_0 c/S}\sin(kl)+\cos(kl)}\cos(kl_0)\right\}\left\{\sin(kx)+\frac{jZ_{A1}}{\rho_0 c/S}\cos(kx)\right\} \quad \textbf{(4. 28)}$$

When $l_0 \le x < l$,

$$\hat{p}(x,f)=\frac{4\pi A}{\left\{\frac{-jZ_{A1}}{\rho_0 c/S}+\frac{\frac{Z_{A2}j}{\rho_0 c/S}\cos(kl)-\sin(kl)}{\frac{Z_{A2}j}{\rho_0 c/S}\sin(kl)+\cos(kl)}\right\}}\left\{\sin(kl_0)+\frac{jZ_{A1}}{\rho_0 c/S}\cos(kl_0)\right\}\left\{\sin(kx)+\frac{\frac{Z_{A2}j}{\rho_0 c/S}\cos(kl)-\sin(kl)}{\frac{Z_{A2}j}{\rho_0 c/S}\sin(kl)+\cos(kl)}\cos(kx)\right\} \quad \textbf{(4. 29)}$$

The boundary impedances can also be written in terms of the termination phasors.

$$Z_{A2}=\frac{1+e^{-2\Phi_2}}{1-e^{-2\Phi_2}}\rho_0 c/S. \quad \textbf{(4. 30)}$$

If Z_{A1} is defined as the ratio of pressure and "left traveling" wave velocity at $x=0$, then

$$Z_{A1}=-\frac{1+e^{-2\Phi_1}}{1-e^{-2\Phi_1}}\rho_0 c/S=\frac{1+e^{+2\Phi_1}}{1-e^{+2\Phi_1}}\rho_0 c/S, \quad \textbf{(4. 31)}$$

where Φ_1 and Φ_2 are related the to the boundary reflection coefficients: $R_1 = e^{-2\Phi_1}$ and $R_2 = e^{-2\Phi_2}$.Using the solution derived in equation (4.20), when $0 \le x < l_0$, and multiplying $[(1-e^{2\Phi_1})(1-e^{-2\Phi_2})\frac{Z_{A2}\, j}{\rho_0 c / s}\sin(kl) + \cos(kl)]$ by both the denominator and the numerator and substituting Z_{A1} using equation (4.23) yields

$$\hat{p}(x,f) = \frac{4\pi}{\left\{ j(1+e^{2\Phi_1})(j(e^{-2\Phi_2}+1)\sin(kl) + (1-e^{-2\Phi_2})\cos(kl)) + j(e^{-2\Phi_2}+1)(1-e^{2\Phi_1})\cos(kl) - (1-e^{2\Phi_1})(1-e^{-2\Phi_2})\sin(kl) \right\}}$$

$$* \left\{ (e^{-2\Phi_2}+1)\sin(kl) + (1-e^{-2\Phi_2})\cos(kl))\sin(kl_0) + (j(e^{-2\Phi_2}+1)\cos(kl) - (1-e^{-2\Phi_2})\sin(kl))\sin(kl_0))\cos(kl_0) \right\}$$

$$* \left\{ \sin(kx)(1-e^{2\Phi_1}) + j(1+e^{2\Phi_1}\cos(kx) \right\}$$

(4. 32)

Expanding the sine and cosine terms using the Euler identity,

$$\sin x = \frac{e^{jx} - e^{-jx}}{2j}, \qquad \textbf{(4. 33)}$$

$$\cos x = \frac{e^{jx} + e^{-jx}}{2}, \qquad \textbf{(4. 34)}$$

the pressure field can be written as

$$\hat{p}(x,f) = \frac{4\pi}{j(1-e^{-2\Phi_1-2\Phi_2-2jkL})}(e^{-jk(l_0-x)} + e^{-jk(l_0+x)}e^{-2\Phi_1} + e^{jk(l_0+x)}e^{-2jkL-2\Phi_2} + e^{jk(l_0-x)}e^{-2jkL-2\Phi_1-2\Phi_2}),$$

(4. 35)

when $l_0 \le x < l$. Because of the symmetry between x and l_0 in equation (4.1) and (4.2), the pressure field in the range $0 \le x < l_0$ can be derived by simply switching the positions of x and l_0 in the above solution:

$$\hat{p}(x,f) = \frac{4\pi}{j(1-e^{-2\Phi_1-2\Phi_2-2jkL})}(e^{-jk(x-l_0)} + e^{-jk(x+l_0)}e^{-2\Phi_1} + e^{jk(x+l_0)}e^{-2jkL-2\Phi_2} + e^{jk(x-l_0)}e^{-2jkL-2\Phi_1-2\Phi_2}),$$

(4. 36)

when $0 \le x < l_0$. Combining these 2 solutions, the general solution for $0 \le x < l$ can be written as:

$$\hat{p}(x, f) = \frac{4\pi}{j(1 - e^{-2\Phi_1 - 2\Phi_2 - 2jkL})}(e^{-jk|(l_0 - x)|} + e^{-jk(l_0 + x)}e^{-2\Phi_1} + e^{jk(l_0 + x)}e^{-2jkL - 2\Phi_2} + e^{jk|(l_0 - x)|}e^{-2jkL - 2\Phi_1 - 2\Phi_2}) \quad \textbf{(4. 37)}$$

This is the pressure inside the one dimensional duct with a sound source located at position l_0. It is a function of both frequency and location.

4.2.3 Solution using equivalent circuit

The linear one-dimensional sound system can also be modeled using an plane-wave equivalent circuit. A series of T-networks can be used to accurately model the impedance tube below the cut-off frequency of the first cross mode (see Fig. 2.2).

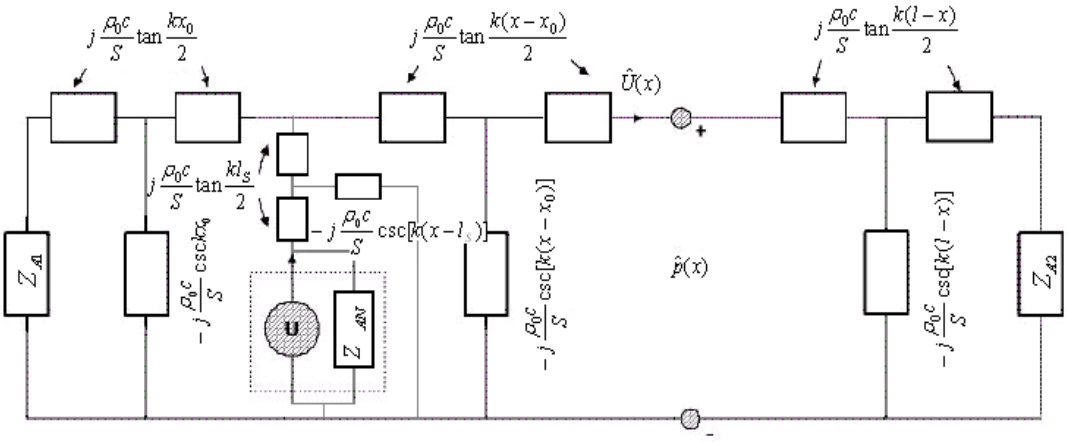

FIG. 4.2. Equivalent circuit model of the one dimensional source-on-the-side configuration.

The non-ideal source can be modeled using a Norton-equivalent circuit involving an ideal volume velocity source with an impedance element in parallel. There is a short tube with length

l_s that connects this source to the main section of the tube. This is the distance from the equivalent depth of the speaker cone to the center of the main tube. The potential $\hat{p}(x)$ represents the pressure at field location x. A T-network connects this pressure probe point and the end impedance Z_{A2}. It represents the l - x long duct segment between the right termination and the field location x. Similarly, two T-networks of length x_0 and x - x_0 respectively represent the duct between the left end impedance Z_b and the source as well as the source and the probe point.

Using the impedance translational theorem [2] and Thevenin's theorem, the elements on the two sides of the probe point can be simplified and reduced to as few equivalent elements as possible. First the impedances Z_{A1} and Z_{A2} can be translated through the l - x duct section using the impedance translational theorem. This results in the two impedances Z_{AT1} and Z_{AT2} (see Fig. 4.3).

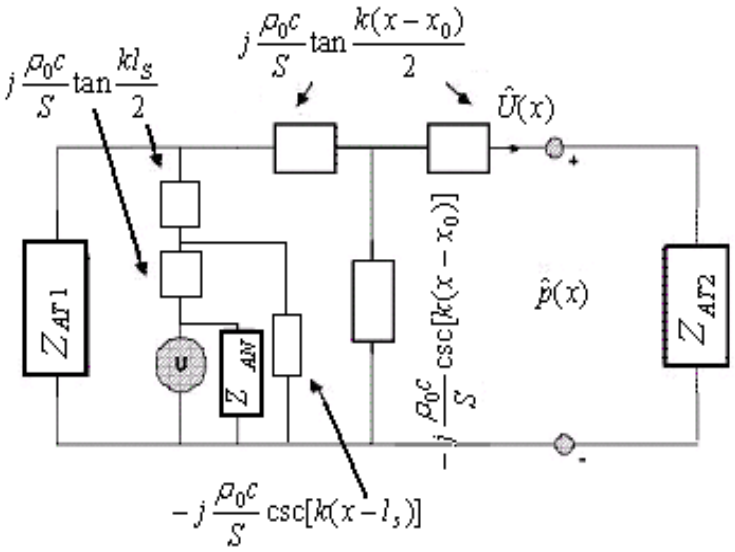

FIG. 4.3. The equivalent circuit after the impedance translation.

As shown in Fig. 4.4, the elements on the left side of the probe point *x* can be reduced to a simple voltage source and a series impedance using Thevenin's theorem.

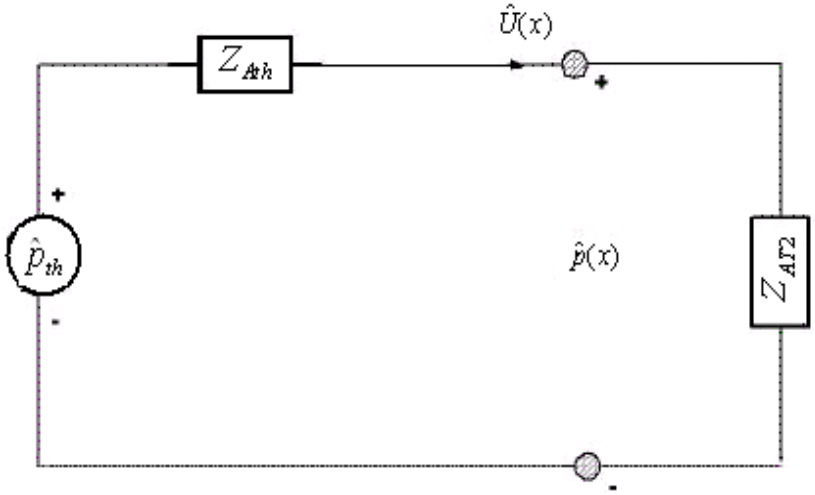

FIG. 4.4. The simplified equivalent circuit.

The potential $\hat{p}(x)$ and flow $\hat{U}(x)$ can be simply found using:

$$\hat{p}(x) = \hat{p}_{th} \cdot \frac{Z_{At_2}}{Z_{Ath} + Z_{AT2}} \tag{4. 38}$$

$$\hat{u}(x) = \frac{\hat{p}_{th}}{(Z_{Ath} + Z_{AT2})} \tag{4. 39}$$

where, $\hat{p}_{th}$ and $\hat{Z}_{ATH}$ are the Thevenin equivalent pressure and impedance derived in the appendix.

4.3 Numerical comparison

In order to compare the two different models that are based on the second order differential equation and the equivalent circuit, the solutions can be evaluated numerically. A plane-wave tube with length 109.8 cm is used for both models. A source is placed at 27.4 cm

from the left side of the tube. The pressure fields are sampled at 51 cm from the left side of the tube. As shown in Figs. 4.5 and 4.6**,** the two models yield nearly identical results for the pressure and particle velocity fields.

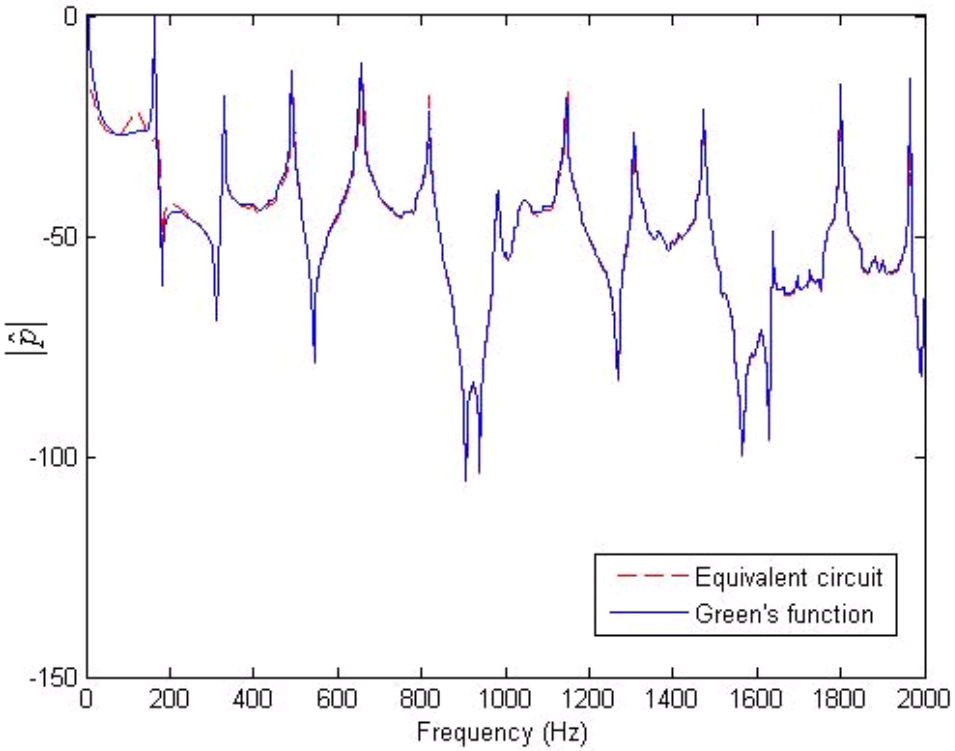

FIG. 4.5. Pressure field comparison at 57.4 cm (equivalent circuit solution vs. Green's function solution).

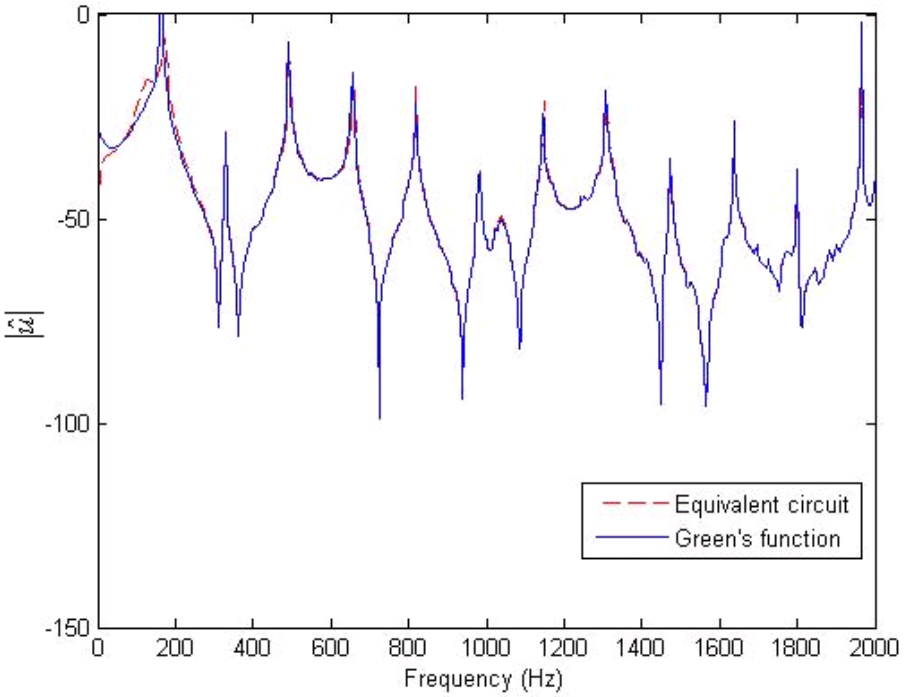

FIG. 4.5. Particle velocity comparison at 57.4 cm (equivalent circuit solution vs. Green's function solution).

The derivation using the equivalent circuit is much simpler. It also greatly simplifies the process of modeling the source. However the application of the equivalent circuit is restricted to the one-dimensional sound field.

An experimental setup was used for measurements to be taken to further validate the modeled field. A one dimensional tube with length 109.78 cm was sealed with two stainless steel plates at each end. A side branch was connected to the main tube and centered at 27.39 cm from end left side of the tube. A loudspeaker was attached to the end of the side branch. The pressure field was measured with a type 1 prepolarized microphone at 92.4 cm from the left side of the tube. In Fig 4.7, the measured data is compared to the modeled pressure field at the same location.

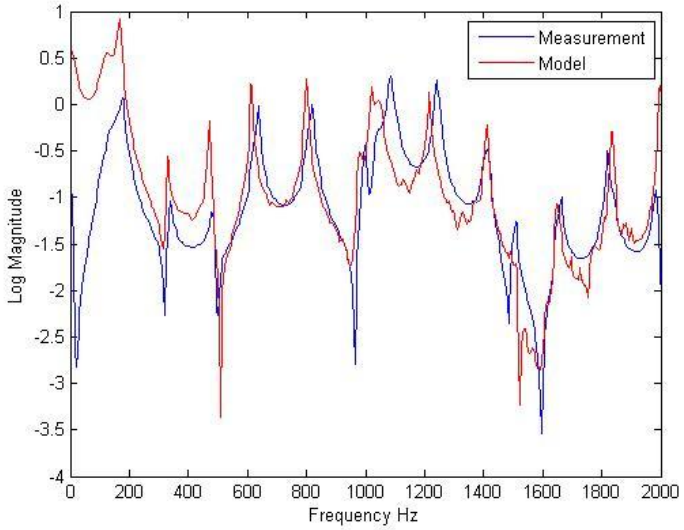

FIG. 4.6. Comparison of measured pressure and modeled pressure at 92.4 cm.

4.4 Equalization Implementation

As discussed in the previous chapter, the sound field can be equalized based on single-point pressure, smoothed single point pressure, spatially averaged mean-square pressure, or energy density. For each physical quantity, four different algorithms can be applied to calculate the inverse filter: homomorphic inversion, weighted homomorphic inversion, least-squares inversion, and delayed least-squares inversion. The same algorithms can be implemented in equalizing the pressure field for the loudspeaker on the side configuration.

4.4.1 Homomorphic inversion

This algorithm is used in the frequency domain for a direct inversion of the minimum-phase part of the original response. Figure 4.8 through 4.11 show equalization of the pressure field along the tube based on the inversion of a single point pressure, smoothed single point pressure, single point energy density and spatially averaged pressure.

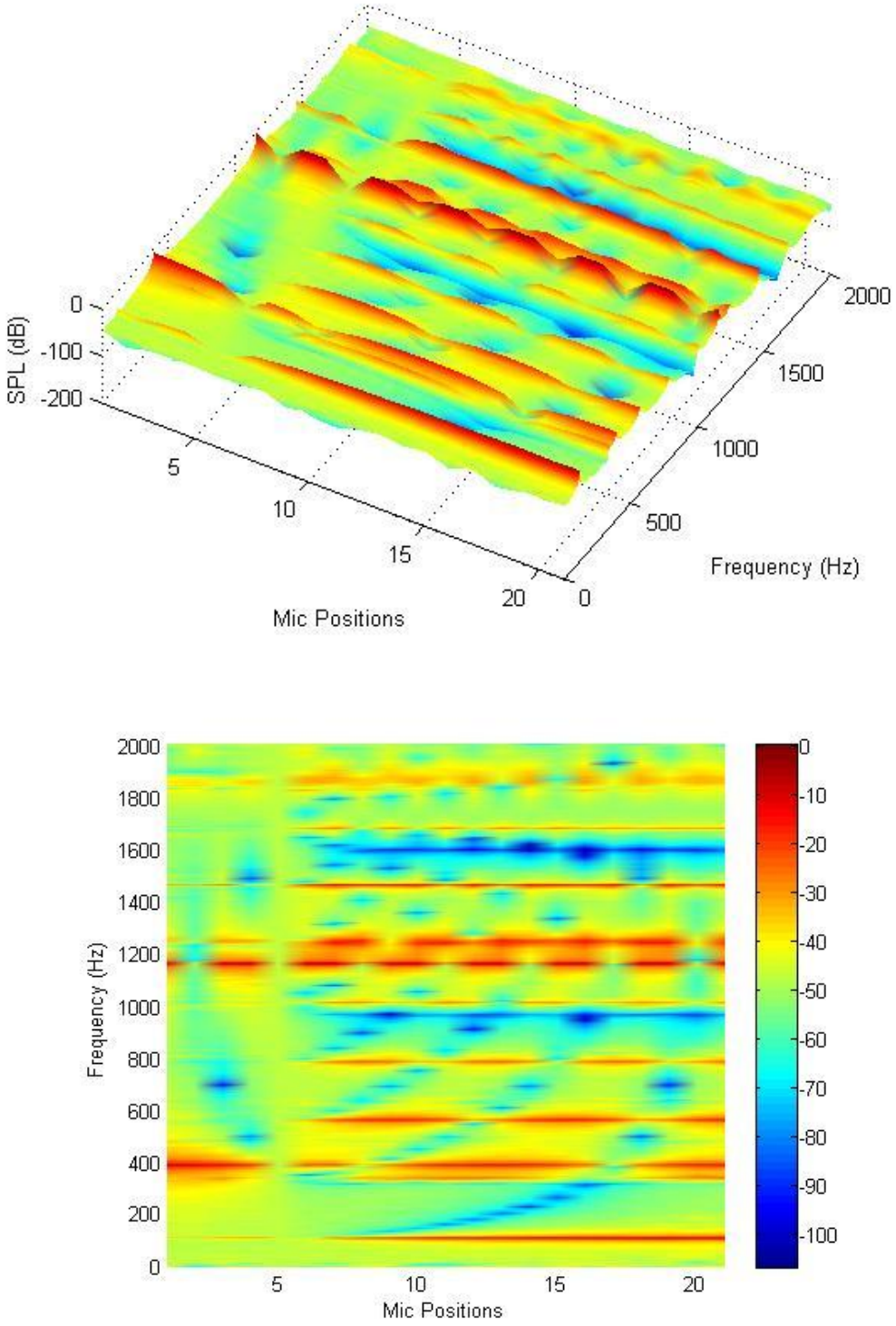

FIG. 4.7. Single point pressure EQ.

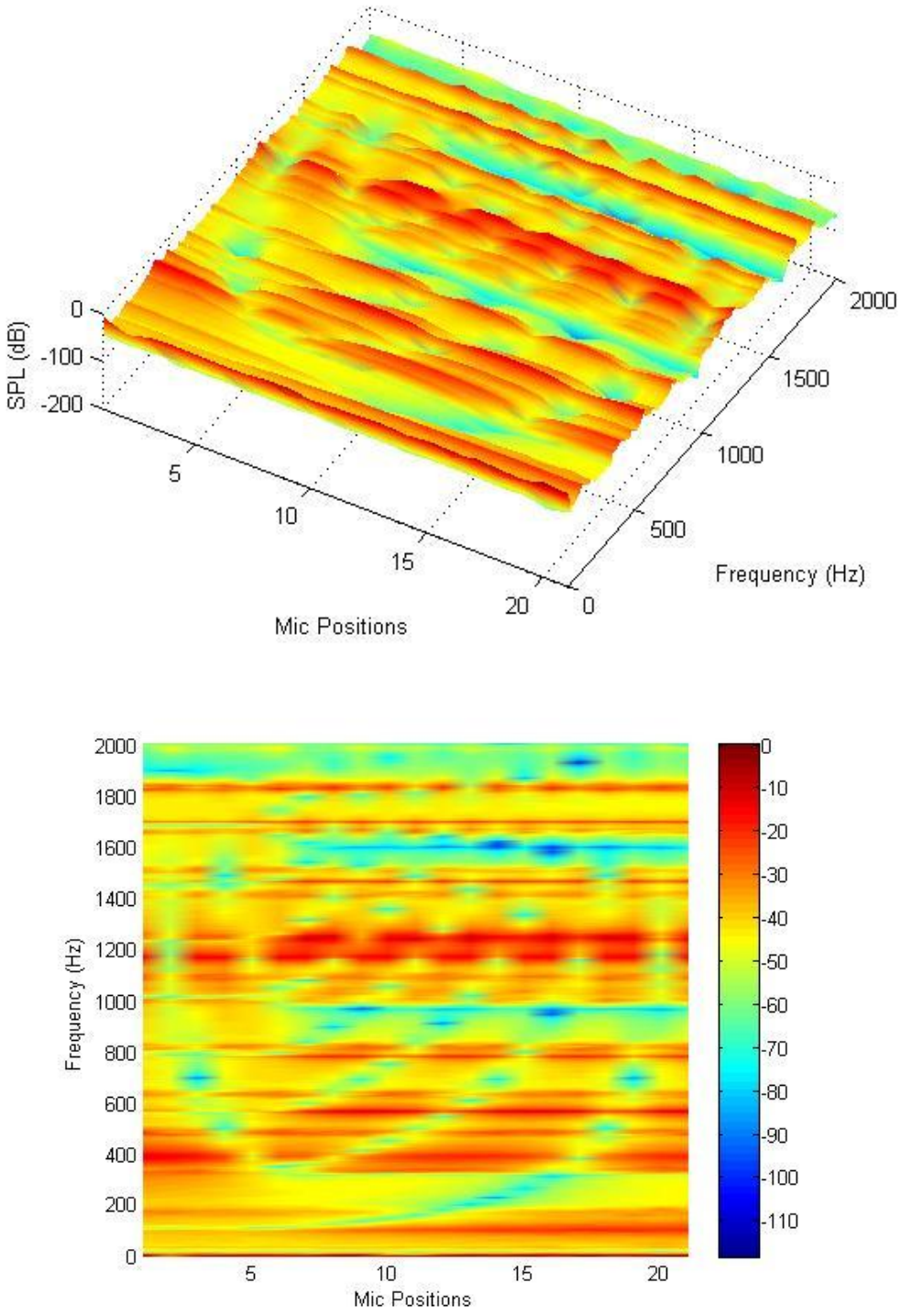

FIG. 4. 8. Single point smoothed pressure EQ.

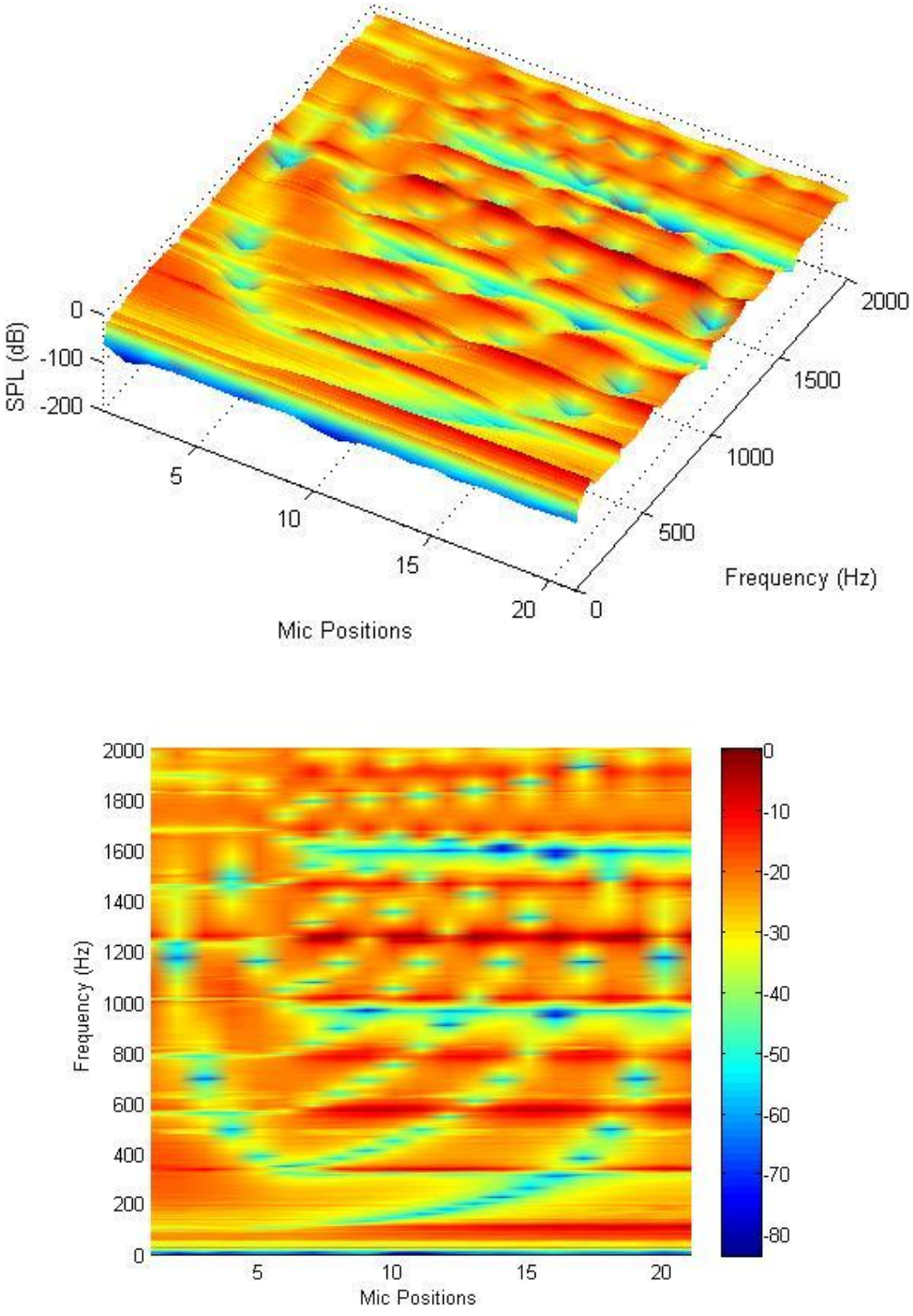

FIG. 4.9. Single point ED EQ.

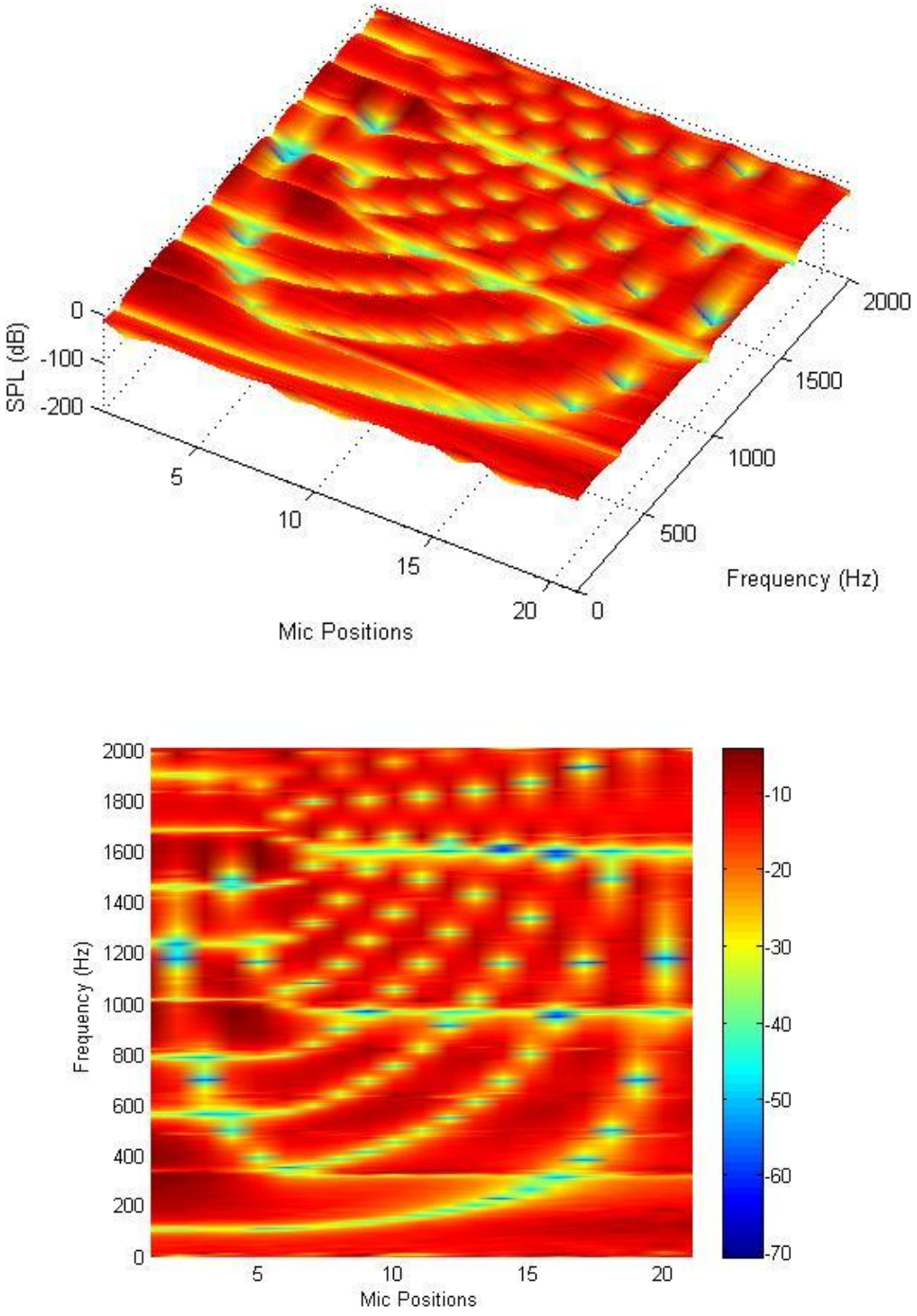

FIG. 4.10. Spatially averaged pressure EQ.

Comparing the four physical quantities used for equalization, single-point pressure equalization yields the flattest spectrum at the point of equalization. However, due to the spatial variation of the spectrum, single-point pressure equalization can not correct the frequency responses at other locations. Often, the flatness of the spectrum at random field locations is worsened by boosting the spectral dips that are unique to the point of equalization. Smoothed pressure equalization reduces the spatial dependency of the sampled pressure by lowering the differences between spectral dips and spectral peaks. Therefore this may method yield a more global equalization result. Spatially averaged mean-square pressure gives the best result for all positions along the duct. This is because it only boosts the spectral dips that are common to all spatial positions. Single point energy density equalization generates a similar result. This is due to the fact that the spectral peaks and dips of energy density line up with those of the spatially averaged pressure in the one dimensional field. The difference between the energy density equalization and the spatially averaged pressure equalization is the result of the fact that for the speaker-on-the-side configuration, the speaker location produces spectral dips at different frequencies for the sound field to the left of the loudspeaker and to the right of the loudspeaker. The energy density to the left of the loudspeaker will pick up different dips than the energy density to the right of the loudspeaker. After the inversion, an equalization filter based on the energy density sampled at the left branch will make boosts at the dip frequencies that are not common to both sides of the loudspeakers. Spatially averaged pressure is more immune to such problems because it evens out the dips that do not occur at common frequencies between the left and the right side of the speaker.

4.4.2 Weighted Homomorphic Inversion

As stated before in the previous chapter, delayed homomorphic inversion moves the zeros further away from the unit circle. Therefore, the added weighting gives a better inversion after the linear deconvolution is performed in the time domain. As the weighting coefficient increases, the deconvolution should converge closer to the ideal single impulse. Figure 4.12 shows that as the weighting factor λ increases, the error between the deconvolved signal and an ideal impulse response becomes smaller.

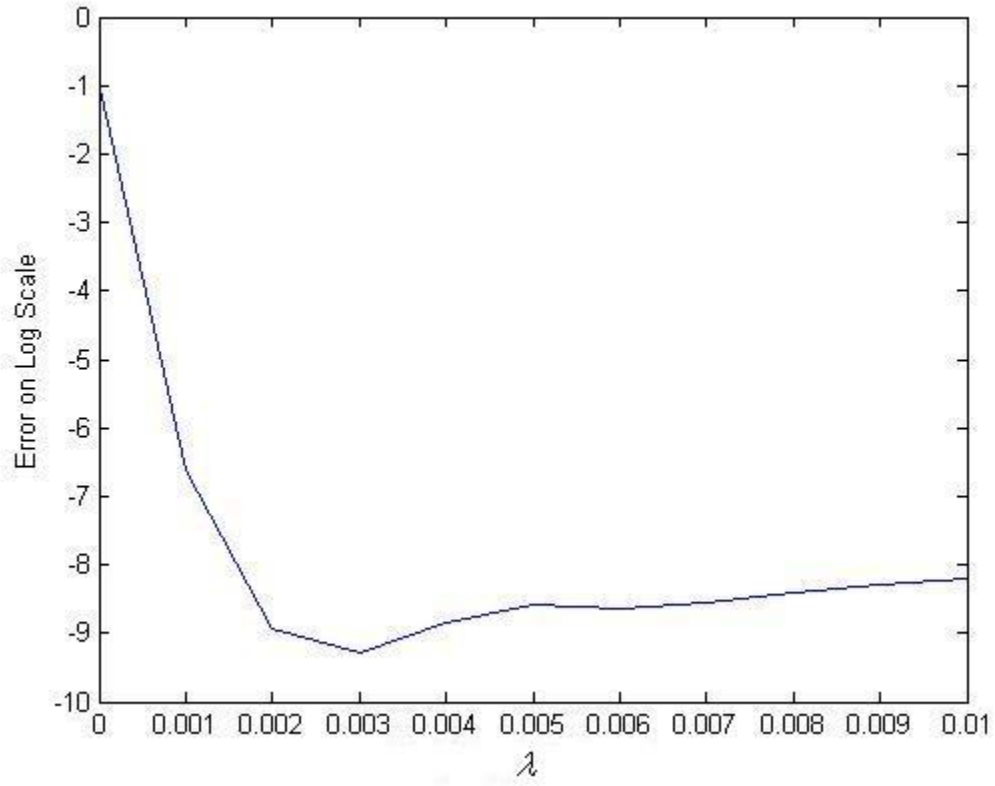

FIG. 4.11. Error signal as a function of weighting coefficient.

4.4.3 Least-squares inversion

The least-squares inversion should yield the closest deconvolution to an ideal impulse response. This is due to the fact that the error signal between the deconvlution and the ideal single impulse response is mathematically minimized through the algorithm. As a result, the deconvolution result gives a dryer impulse than those of the homomorphic or weighted homomorphic inversions (FIG 4.12).

4.4.4 Delayed least-squares inversion

An improved inversion algorithm based on the regular least-squares inversion follows from the use of delay. The ideal single impulse response is delayed several samples before being subtracted by the deconvolution. The delay value is chosen by using the Simpson sidewards recursion in order to minimize the error between the deconvolution and the delayed ideal single impulse response. This error signal should decrease as the number of delays increases (see FIG 4.13).

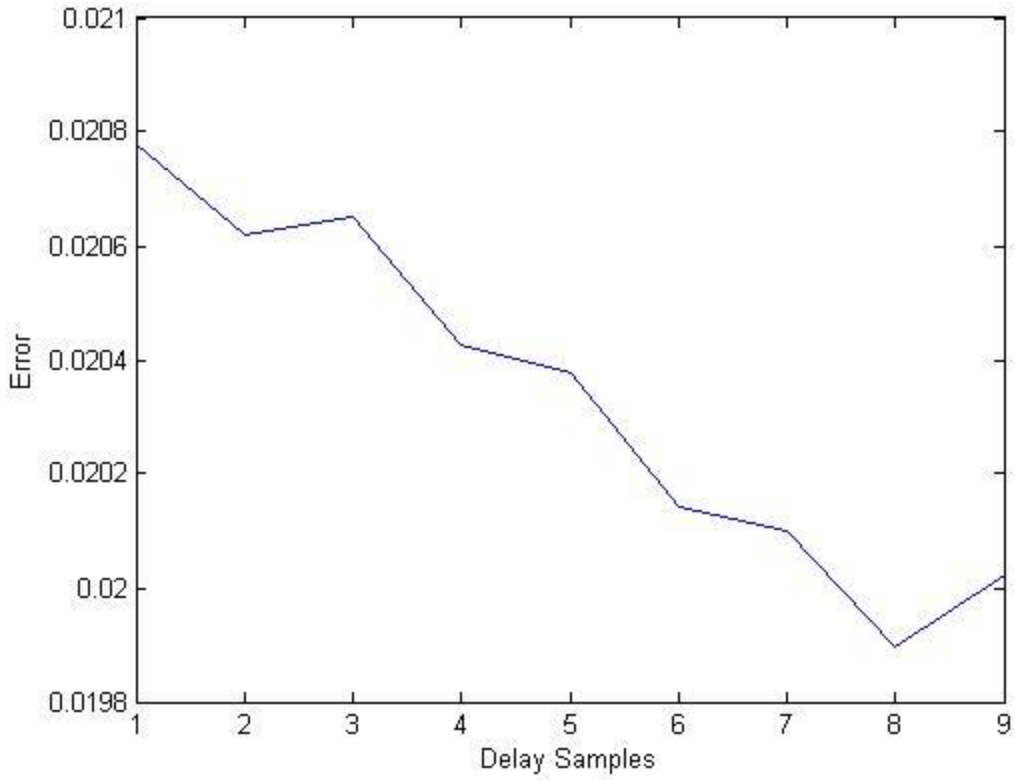

FIG. 4.12. Error signal as a function of sample of delays.

4.4.5 Comparison of the four inversion algorithms.

The deconvolution results using these four inversion algorithms can be compared. As predicted, the delayed least-squares inversion gives the driest deconvolution. The undelayed least-squares inversion shows improvement over the two homomorphic inversion algorithms. The weighted homomorphic inversion generates drier result even though it yields exactly the same spectral magnitude equalization as the regular homomorphic inversion. The weighted homomorphic inversion improves the phase equalization over the regular homomorphic inversion in the frequency domain. This results in a better dereverberation in the time domain.

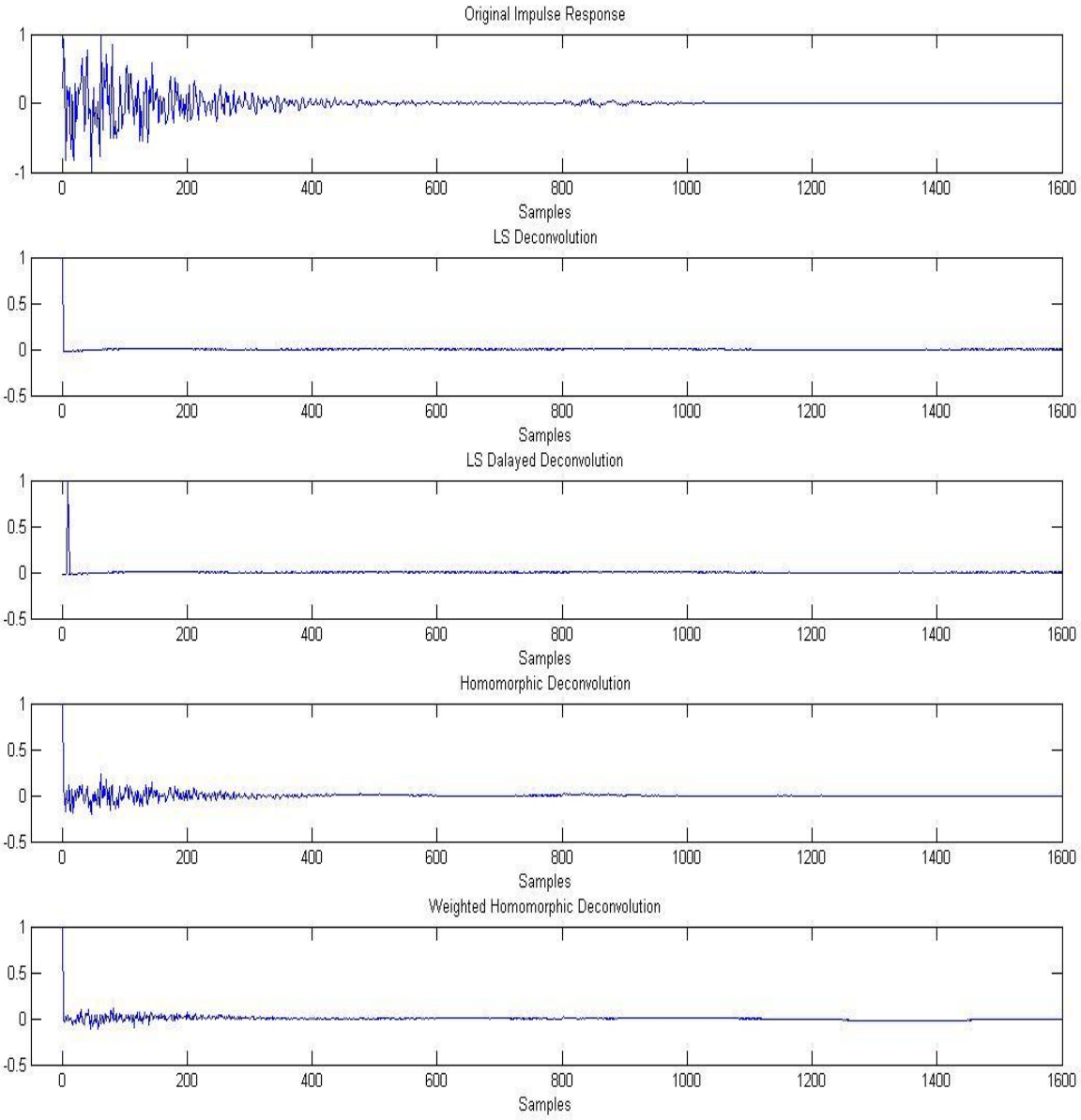

FIG. 4.13. Comparison of the four inversion schemes.

Here the source the sound field is equalized at the source location (27.39 cm to the end of the tube) using the inverse filter based on the single point pressure at the same position. From Fig. 4.14, it can be shown that the delayed least-squares method gives the driest deconvolution. This

is the preferred method for the inversion. As shown in section 4.4.1, energy density is the best physical quantity to generate a global equalization result over the listen area with the least amount of spatial averages needed. Using the delayed least-squares inversion, Fig. 4.15 shows the deconvolution results of the equalized pressure field at the point of equalization sensor (27.39 cm to the end of the tube) and an arbitrarily chosen location (42.39 cm to the end of the tube.)

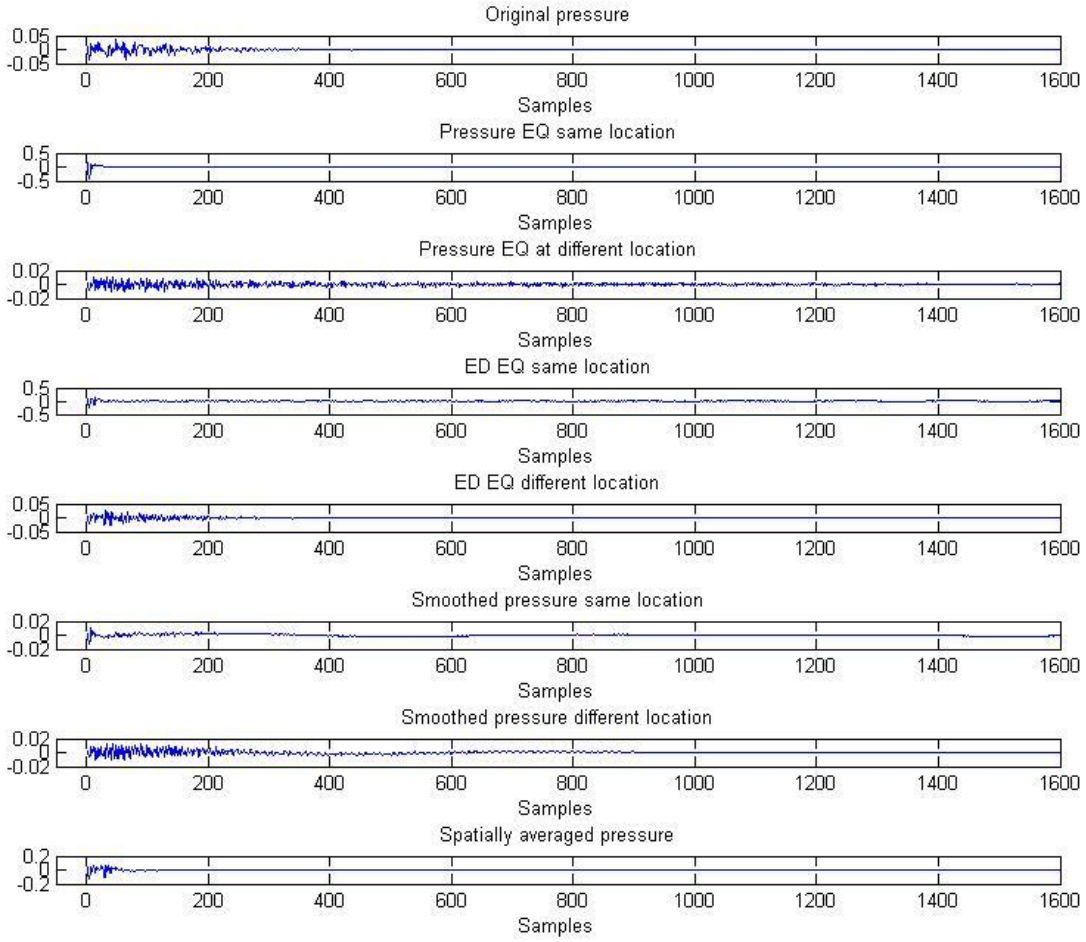

FIG. 4.14. Deconvolution results of pressure field equalization based on different physical quantities.

It can be shown from the deconvolution plots that although the single point pressure equalization generates a perfectly dry signal at the position of the equalization sensor, it elongated the ringing at other locations. This fact is also shown in the frequency domain equalization plot (see Fig. 4.8.). When generating a flat spectrum at the point of equalization sensor, more resonances are brought in to the spectrum at other points of equalization. Smoothed pressure equalization reduces the unintended artifacts from the equalization at locations other than the equalization sensor location and generates a more global equalization result. Spatially averaged pressure equalization gives the best equalization result across the field positions but it requires a large amount of spatial averaging to measure this physical quantity. Single energy density equalization yields a drier equalization result than the smoothed pressure equalization either at the sensor location or at other field locations.

4.5 Conclusion

In this chapter, three different theoretical models were discussed and compared. Modal expansion is a straight-forward way to model the sound field. It also applies in one, two, or three-dimensional modeling. However, in numerical computation, it is impractical to have an infinite summation of terms. Truncating the higher-order terms usually affects the accuracy of the model. The closed-form solutions derived from the Green's function or the equivalent circuits give the most concise results. They can be directly implemented for numerical modeling with no loss of accuracy due to the truncation of terms. The equivalent circuit provides a much simpler approach to solve the differential equation. It is shown numerically that the closed-form solutions derived from the Green's function and the equivalent circuit yield essentially identical

results. However, both of these solutions are limited to the one-dimensional system and cannot be readily applied to two or three dimensions.

Four different inversion schemes were implemented and compared: homomorphic inversion, weighted homomorphic inversion, least-squares inversion, and delayed least-squares inversion. The delayed least-squares inversion yields the best result in deconvolution. This algorithm was applied to the pressure field equalization based on four physical quantities: single point pressure equalization, smoothed pressure equalization, spatially averaged pressure equalization, and energy density equalization. While spatially averaged pressure equalization gives the best result over the whole listening area, the amount of spatial averages to measure this physical quantity makes it impractical to implement. Single point energy density equalization has been shown to yield a more global equalization result than the single point pressure and smoothed pressure equalization. Due to the small number of sample locations required to measure the energy density (only one location was needed in the one-dimensional field), this method was much easier to implement than the spatially averaged pressure equalization. However, it still maintained a global equalization result for a "listening region" with the loudspeaker on the side of the tube.

References

[1] P. A. Nelson, S. J. Elliott, *Active Control of Sound,* (Academic Press ,June 24, 1993).

[2] L. E. Kinsler, A. R. Frey, A. B. Coppens, and J. V. Sanders, *Fundamentals of Acoustics,* 4th ed., (Wiley, New York, 2000).

Chapter 5

Three-Dimensional Sound Field Modeling and Equalization

5.1 Introduction

A three dimensional sound field can be established in any enclosure with dimensions are large enough that modes of interest are not evanescent along any dimension. The characteristics of the acoustic energy content depend heavily upon the conditions of the boundaries. When the boundaries are acoustically rigid, the reverberant field dominates the direct field. And when the boundaries are anechoic, the direct field predominates. These are the two extreme conditions and most rooms fall between the fully reverberant and fully anechoic conditions. Without the content of the reverberant field, the anechoic field preserves the spectrum of the original source without the added coloration from the room. On the other hand, spectral colorations are present in a fully reverberant field due to the strong reverberant content. Under such circumstances, sound field equalization is required in order to restore the original spectrum of the direct sound field or desired audio signal.

There are a number of ways to accurately model the steady state three-dimensional sound field. The boundary conditions of the room have a great impact on the final solution of the pressure field. Due to the steady nature of the fully diffused field, the boundary conditions can be modeled using the average absorption coefficients. This chapter will introduce and compare different ways of accurately modeling the sound field in a three-dimensional room.

5.2 Reverberation time measurement

In a diffuse field, all directions of propagation contribute equal sound intensities. Under this assumption, the average energy sampled in a sufficiently large volume should have an even distribution across the field. A transient field needs adequate time lapse until such uniformity can be achieved. A common assumption is that this lapse is reached when the hundredth reflected wave arrives at a field position. A main character to describe the diffuse field is the reverberation time. Statistically, after the sound source is turned off, the running time average of the squared pressure or energy density follows an exponential decay curve:

$$\overline{w}(t) = \overline{w}(0)e^{-t/\tau}, \tag{5. 1}$$

where $\overline{w}(t)$ is the energy density at time t and τ is the characteristic decay time, which is related to the volume of the room V and the average absorption A_s of the boundaries:

$$\tau = \frac{4V}{cA_s}. \tag{5. 2}$$

In this expression, c is the speed of sound. The time it takes for the energy density to drop 60 dB is the reverberation time T_{60}, such that

$$\frac{\overline{w}(t)}{\overline{w}(0)} = e^{-t/T_{60}} = \frac{1}{10^6} \tag{5. 3}$$

For a fully diffuse field, the reverberation time is related to the volume V and the absorption coefficient α_i of the *ith* surface:

$$T_{60} = \frac{.0161V}{\sum_i \alpha_i A_i}. \tag{5. 4}$$

Typical absorption coefficients of the boundary materials of the enclosure are frequency dependent. As a result, the reverberation time should also be a function of frequency. M.R. Schroeder [1] has suggested an integration method to directly calculate the reverberation time of a given enclosure from its measured steady state impulse response function. Ideally, the time variant energy content of a decaying field after a noise source is turned off should be obtained from numerous measured impulse response functions with random noise excitations. Such practice becomes impractical when the large number of impulse response measurements is required for the averaging process. However, a time integration of a single impulse response function can be utilized to substitute for the averaging of numerous impulse response functions. The equivalence of these two methods can be sufficiently validated when the excitation signal is fully stochastic. For example, suppose a band filtered "tone burst" $n_{\Delta f}(t)$ of the desired frequency range Δf is radiated into the enclosure. This band filtered tone burst should be random to assure the stochasticity of the process. This requires the autocovariance function of the input noise to be proportional to a Dirac delta function,

$$E\{[n_{\Delta f}(t_1)-\mu][n_{\Delta f}(t_2)-\mu]\} = N\delta(t_1-t_2), \tag{5. 5}$$

where *N* is the power of the noise in the given bandwidth, and μ is the expectation value of the input noise $n_{\Delta f}(t)$. Because of the random nature of this input noise, $\mu = 0$. This leads to the simplification of Eq. (5.5):

$$E\{[n_{\Delta f}(t_1)][n_{\Delta f}(t_2)]\} = N\delta(t_1-t_2). \tag{5. 6}$$

The instantaneous power at time t of the measured signal is the multiplication of the convolutions between the noise signal $n_{\Delta f}(t)$ and the impedance response $h(t)$ of the system:

$$x^2(t) = \int_{-\infty}^{0} dt_1 \int_{-\infty}^{0} dt_2 n_{\Delta f}(t_1) n_{\Delta f}(t_2) h(t-t_1) h(t-t_2) \tag{5. 7}$$

Taking the expected value (ensemble average over different samples of the power spectrum) of both sides of the equation and using Eq. (5.6), the average signal power can be expressed as:

$$\begin{aligned} E[x^2(t)] &= \int_{-\infty}^{0} dt_1 \int_{-\infty}^{0} dt_2 E[n_{\Delta f}(t_1) n_{\Delta f}(t_2)] h(t-t_1) h(t-t_2) \\ &= \int_{-\infty}^{0} dt_1 \int_{-\infty}^{0} dt_2 N\delta(t_1 - t_2) h(t-t_1) h(t-t_2) \\ &= N \int_{-\infty}^{0} dt_1 h^2(t-t_1) \\ &= N \int_{t}^{\infty} h^2(t_1) dt_1 \end{aligned} \tag{5. 8}$$

The integration thus eliminates the need for the ensemble average. A single impulse response function measured at any given location inside the enclosure is all that is needed to obtain the average power. Similar to the ensemble average, this reverser Schroeder integral smoothes out the random fluctuations of the decay curve of the impulse response function due to the contributing factors such as the initial magnitude and phase of the normal modes when the source was turned off.

In practice, a lower signal to noise ratio caused by the existing noise floor disallows the signal from decaying through the whole 60 dB range. Other issues arise when the Schroeder reverse integral curve consists of multiple decay slopes in the 60 dB range. In such cases, shorter decay times such as T30 or T10 can be extracted in place of the T60. These values estimate the time for the sound energy to drop 60 dB following the initial 30 dB or 10 dB decay.

In the experimental setup to extract the reverberation time from the measured impulse response functions inside a 5.7 x 4.3 x 2.5 m reverberation chamber, six random microphone

locations and two speaker locations were chosen according to the ISO standard 354:2003 [2]. This generates twelve speaker-to-microphone configurations. A dodecahedron source was chosen to cover the 50 Hz to 20 kHz frequency range and a subwoofer was used to cover the 25 to 50 Hz range to ensure that adequate sound power was injected into the enclosure in the low frequency range. The reverberation time T30 was determined from the Schroeder reverse integral of the impulse response functions. All twelve locations were averaged according to the ISO standard 354:2003. These impulse response functions were filtered using third-octave-band filters in post processing. Each T30 was extracted within the individual third-octave band and all twelve configurations were averaged for each T30 measurement. The reverberation times measured for the chamber are listed in Table 5-1.

Table 5-1: Reverberation Time Measurement

Frequency (Hz)	***T30 (ms)***	*Frequency (Hz)*	T30 (ms)
25	2940	800	3662
31.5	3130	1000	3734
40	2907	1250	3587
50	2572	1600	3353
63	2822	2000	30334
80	3108	2500	2637
100	2378	3150	2266
125	3677	4000	1932
160	3265	5000	1656
200	3545	6300	1329
250	3453	8000	1009
315	3730	10000	795
400	3465	12500	580
500	3390	16000	448
630	3680	20000	397

These measured T30 values can be built into the three dimensional model to more accurately simulate the pressure field.

5.3 Absorption modeling

The reverberation time reflects the loss in a system. This loss is the result of the boundary conditions that are absorptive as well as the air absorption in the system. In most cases, the air absorption is much less than the boundary absorptions. For a rectangular room the normal specific acoustic boundary impedance Z_s can be represented through the complex wave number $\tilde{k}$ in each of the three dimensions. Suppose the normalized unitless impedance of the two walls perpendicular to the x direction is

$$\zeta_x = \frac{Z_{sx}}{\rho_0 c}. \tag{5. 9}$$

From the Euler's equation along the *x* direction, the *x* dependent factor of pressure is related to the impedance by the expression

$$j\tilde{k}_x \hat{p}_x = -\zeta_x \frac{\partial \hat{p}_x}{\partial x} \tag{5. 10}$$

Applying this equation to both of the boundaries, a relationship between the complex wave number $\tilde{k}_x$ and the boundary unitless impedance ζ_x can be derived [3] [4]:

$$e^{j\tilde{k}_x l_x} = \pm \frac{k - \tilde{k}_x \zeta_x}{k + \tilde{k}_x \zeta_x}, \tag{5. 11}$$

where l_x is the length of the enclosure along the *x* dimension. There is not an analytical solution to this equation, but approximations can be made under certain circumstances. For the

reverberation chamber, the boundary impedance may be considered a large real number $\zeta_x = \xi_x$. The right side of Eq. (5.11) can be then simplified as follows

$$\begin{aligned} e^{j\tilde{k}_x l_x} &= \pm\frac{k-\tilde{k}_x\xi_x}{k+\tilde{k}_x\xi_x} \\ &= \mp\frac{1-\dfrac{k}{\tilde{k}_x\xi_x}}{1+\dfrac{k}{\tilde{k}_x\xi_x}} \\ &\approx \mp\left(1-\frac{k}{\tilde{k}_x\xi_x}\right)^2 \approx \mp\left(1-\frac{2k}{\tilde{k}_x\xi_x}\right). \end{aligned} \tag{5. 12}$$

The imaginary part of the complex wave number $\tilde{k}_x$ is much smaller than the real part due to the small amount of absorption present. Considering the fact that $e^{jk_{x,R}l_x} = e^{jn_x\pi} = \mp 1$, Eq. (5.12) can be further simplified to

$$\mp e^{-k_{x,I}l_x} \approx \mp\left(1-\frac{2k}{k_{x,R}\xi_x}\right). \tag{5. 13}$$

Using a Taylor series expansion about zero on the left side of the equation yields

$$\begin{aligned} &1-k_{x,I}l_x \approx \left(1-\frac{2k}{k_{x,R}\xi_x}\right), \\ &k_{x,I}k_{x,R} = \frac{2k}{\xi_x l_x}; \qquad\qquad if\ k_{x,R} \neq 0, \end{aligned} \tag{5. 14}$$

When $k_{x,R} = 0$, Eq. (5.12) can be simplified to

$$\begin{aligned} e^{j\tilde{k}_x l_x} &\approx \mp\left(1-\frac{2k}{\tilde{k}_x\xi_x}\right), \\ e^{-k_{x,I}l_x} &= \mp\left(1-\frac{2k}{jk_{x,I}\xi_x}\right). \end{aligned} \tag{5. 15}$$

Using a Taylor series expansion on the left side and discarding the negative sign on the left yields

$$
\begin{aligned}
e^{j\tilde{k}_x l_x} &\approx \mp\left(1-\frac{2k}{\tilde{k}_x \xi_x}\right), \\
1-k_{x,I} l_x &= \left(1-\frac{2k}{jk_{x,I}\xi_x}\right), \\
{k_{x,I}}^2 &= -j\frac{2k}{\xi_x l_x}.
\end{aligned}
\tag{5. 16}
$$

This is the relationship between the real part and the imaginary part of the wave number along the *x* direction. Similar relations can be derived for the *y* and *z* directions. This shows that the absorption of the boundary conditions can be built into the complex wave number. For the three-dimensional field, the complex wave number is the square root of the summation of the squared complex wave numbers in each direction:

$$
\begin{aligned}
\tilde{k}_N &= \sqrt{\tilde{k}_x^{\,2} + \tilde{k}_y^{\,2} + \tilde{k}_z^{\,2}} \\
&= [({k^2}_{x,R} + {k^2}_{y,R} + {k^2}_{z,R}) + j2(k_{x,R}k_{x,I} + k_{y,R}k_{y,I} + k_{z,R}k_{z,I}) - ({k^2}_{x,I} + {k^2}_{y,I} + {k^2}_{z,I})]^{1/2}
\end{aligned}
\tag{5. 17}
$$

For the reverberation chamber, since the imaginary part of the wave number is small, the last term in Eq. (5.17) can be ignored. If k_N is defined as

$$
k_N = \sqrt{({k^2}_{x,R} + {k^2}_{y,R} + {k^2}_{z,R})}, \tag{5. 18}
$$

Eq. (5.17) can be simplified as follows:

$$
\tilde{k}_N \approx k_N\left[1 + j\frac{2}{{k_N}^2}(k_{x,R}k_{x,I} + k_{y,R}k_{y,I} + k_{z,R}k_{z,I})\right]^{1/2} \tag{5. 19}
$$

Since the second term is much smaller than 1 when the imaginary part of the wave numbers are of small magnitude, a Taylor expansion can be used for further simplification:

$$\tilde{k}_N \approx k_N + j\frac{1}{k_N}(k_{x,R}k_{x,I} + k_{y,R}k_{y,I} + k_{z,R}k_{z,I}) \quad \textbf{(5. 20)}$$

When the real parts of the wave numbers are not equal to zero, the relation in Eq. (5.14) can be used:

$$\tilde{k}_N \approx k_N + j\frac{k}{k_N}\left(\frac{2}{\xi_x l_x} + \frac{2}{\xi_x l_x} + \frac{2}{\xi_x l_x}\right) \quad \textbf{(5. 21)}$$

When the real parts of the wave numbers are zero, Eq. (5.17) becomes

$$\begin{aligned}\tilde{k}_N &= \sqrt{\tilde{k}_x^{\,2} + \tilde{k}_y^{\,2} + \tilde{k}_z^{\,2}} \\ &= \left[(k_N^{\,2}) - (k^2{}_{x,I} + k^2{}_{y,I} + k^2{}_{z,I})\right]^{1/2}\end{aligned} \quad \textbf{(5. 22)}$$

Using relationship from Eq. (5.16) and a Taylor series expansion,

$$\begin{aligned}\tilde{k}_N &= [(k_N^{\,2}) - (k^2{}_{x,I} + k^2{}_{y,I} + k^2{}_{z,I})]^{1/2} \\ &= k_N + j\frac{k}{k_N}\left(\frac{1}{\xi_x l_x} + \frac{1}{\xi_y l_y} + \frac{1}{\xi_z l_z}\right).\end{aligned} \quad \textbf{(5. 23)}$$

From Eq. (5.21) and (5.23), a generalized form of the complex wave number can be reached:

$$\begin{aligned}\tilde{k}_N &= k_N + j\frac{k}{k_N}\left(\frac{\varepsilon_{n_x}}{\xi_x l_x} + \frac{\varepsilon_{n_y}}{\xi_y l_y} + \frac{\varepsilon_{n_z}}{\xi_z l_z}\right); \\ \varepsilon_i &= \begin{cases} 1 & k_{i,R} = 0 \\ 2 & k_{i,R} \neq 0 \end{cases}\end{aligned} \quad \textbf{(5. 24)}$$

This form incorporates the loss from the boundary conditions into the complex wave number so it can be incorporated into the three-dimensional pressure field model to describe the boundary conditions.

5.4 Reverberant Pressure field modeling

5.4.1 Eigenfunctions for a rectangular room

Similar to the one-dimensional sound field, the three-dimensional pressure field is governed by the Helmholtz equation. With a point source located in the three-dimensional enclosure, the pressure field satisfies the non-homogeneous Helmholtz equation. The solution can be derived from the eigenfunction expansion. For a rectangular room with rigid walls and dimensions L_x, L_y, and L_z, the eigenfunctions ψ can be easily derived from the homogeneous Helmholtz equation:

$$\nabla^2\psi + k^2\psi = 0. \tag{5. 25}$$

Due to the linearity of the gradient operator ∇, the solution can be expressed as the multiplication of three independent solutions in each dimension:

$$\psi = X(x)Y(y)Z(z). \tag{5. 26}$$

The solution can be substituted back into Eq. (5.25). Dividing the result through by $X(x)Y(y)Z(z)$ then yields

$$\frac{1}{X}\frac{d^2X}{dx^2} + \frac{1}{Y}\frac{d^2Y}{dy^2} + \frac{1}{Z}\frac{d^2Z}{dz^2} + k^2\psi = 0 \tag{5. 27}$$

Using separation of variables, Eq (5.27) can be separated into three individual differential equations:

$$\begin{aligned} \frac{1}{X}\frac{d^2X}{dx^2} &= -k_x{}^2, \\ \frac{1}{Y}\frac{d^2Y}{dy^2} &= -k_y{}^2, \\ \frac{1}{Z}\frac{d^2Z}{dz^2} &= -k_z{}^2, \end{aligned} \tag{5. 28}$$

where $k_x^2 + k_y^2 + k_z^2 = k^2$. To satisfy the rigid boundary conditions located at $x = 0$ and $x = L_x$, the solution for the factor in *x* is

$$X(x) = \cos(k_x x). \tag{5. 29}$$

The wave number k_x along the *x* direction is a discrete quantity depending on the length of the room in the *x* direction alone:

$$k_x = \frac{n_x \pi}{L_x}; \quad n_x = 0,1,2,... \tag{5. 30}$$

Similar results can be reached for the factors in the *y* dimension and *z* dimension. The final eigenfunction solution then becomes

$$\psi_N = \cos\left(\frac{n_x \pi}{L_x}\right)\cos\left(\frac{n_y \pi}{L_y}\right)\cos\left(\frac{n_z \pi}{L_z}\right) \tag{5. 31}$$

where N is the three dimensional index represented as follows

$$\begin{aligned} N &= n_x, n_y, n_z \\ n_x &= 0,1,2,... \\ n_y &= 0,1,2,... \\ n_z &= 0,1,2,... \end{aligned} \tag{5. 32}$$

The eigenfunctions form a complete orthogonal set over the volume of the enclosure:

$$\int_0^{L_x}\int_0^{L_y}\int_0^{L_z} \psi_N^2 \, dxdydz = \frac{L_x L_y L_z}{\varepsilon_{n_x}\varepsilon_{n_y}\varepsilon_{n_z}} \tag{5. 33}$$

where

$$\varepsilon_i = \begin{cases} 1; & i = 0 \\ 2; & i \neq 0 \end{cases} \tag{5. 34}$$

And

$$\int_0^{L_x}\int_0^{L_y}\int_0^{L_z}\psi_N\psi_M\,dxdydz=0 \qquad N\neq M \tag{5. 35}$$

5.4.2 Green's Function

When a source is present in the rectangular enclosure, a delta function containing the parameters of the source location can be introduced on the right side of the Helmholtz equation:

$$\nabla^2\hat{p}+k^2\hat{p}=-j\rho_0 ck\hat{Q}_s\delta(\vec{r}-\vec{r}_0)=-j\rho_0 ck\hat{Q}_s\delta(x-x_0)\delta(y-y_0)\delta(z-z_0), \tag{5. 36}$$

where $\vec{r}=(x_0,y_0,z_0)$ is the source location, $\hat{Q}_s$ is the complex source strength, ρ_0 is the density of air and c is the speed of sound. In order to solve this inhomogeneous equation, a Green's function can be introduced. This Green's function must satisfy the same Helmholtz equation

$$\nabla^2 G(\vec{r}\mid\vec{r}_0)+k^2G(r\mid r_0)=-4\pi\delta(\vec{r}-\vec{r}_0). \tag{5. 37}$$

The ectors $\vec{r}$ and $\vec{r}_0$ are the field and the source positions respectively. This Green's function can be expanded using the eigenfunctions for rigid boundary conditions:

$$G(\vec{r}\mid\vec{r}_0)=\sum_{N=0}^{\infty}A_N\psi_N(\vec{r}) \tag{5. 38}$$

Using Eq. (5.38), Eq. (5.37) can be reduced to

$$\sum_{N=0}^{\infty}A_N(k^2-k_N{}^2)\psi_N(\vec{r})=-4\pi\delta(\vec{r}-\vec{r}_0). \tag{5. 39}$$

Multiplying both sides of Eq. (5.39) by $\psi_{N'}(\vec{r})$, integrating both sides over the volume of the enclosure, and using the orthogonality relationship in Eq. (5.34)-(5.35) yields

$$\sum_{N=0}^{\infty} A_N (k^2 - k_N{}^2) \iiint_V \psi_{N'}(\vec{r}) \psi_N(\vec{r}) dV = -4\pi \iiint_V \psi_{N'}(\vec{r}) \delta(\vec{r} - \vec{r}_0) dV,$$

$$A_N = \frac{-4\pi \psi_N(\vec{r}_0)}{(k^2 - k_N{}^2) V \Lambda_N}. \tag{5. 40}$$

Substituting this coefficient back into Eq. (5.38), the Green's function can be represented in terms of the eigenfunctions:

$$G(\vec{r} \mid \vec{r}_0) = -4\pi \sum_{N=0}^{\infty} \frac{\psi_N(\vec{r}_0)}{(k^2 - k_N{}^2) V \Lambda_N} \psi_N(\vec{r}) \tag{5. 41}$$

From Eq. (5.36) and (5.37), the solution of the pressure field can be derived by simply multiplying the Green's function by a factor of $\frac{j\rho_0 ck}{4\pi} \hat{Q}_s$. This factor is equivalent to the source monopole amplitude $\hat{A}$.

$$p = -4\pi \hat{A} \sum_{N=0}^{\infty} \frac{\psi_N(\vec{r}_0)}{(k^2 - k_N{}^2) V \Lambda_N} \psi_N(\vec{r}) \tag{5. 42}$$

With the introduction of losses, the wave number k_N becomes a complex number $\tilde{k}_N$, as derived in Sec. 5.3. The imaginary part is directly related to the boundary conditions, where most of the losses come from. The sound power output of a source is proportional to $\left|\hat{A}\right|^2$.

5.4.3 Source power measurement

For the three-dimensional experimental setup, a dodecahedron source was chosen because of its relatively uniform radiation. To estimate its sound power spectrum, the source was placed in an anechoic chamber centered beneath a half-circle microphone array with 13 microphones spread of 15 degree increments. The array could rotate at 15 degree azimuthal

increments to cover a hemispherer. The system thus allowed the acquisition of 169 pressure measurements over the hemisphere. The source wass turned upside down to measure the radiation from the lower hemisphere. The sound power spectrum was estimated from averaged power spectra of all 338 microphone positions (see Fig. 5.1).

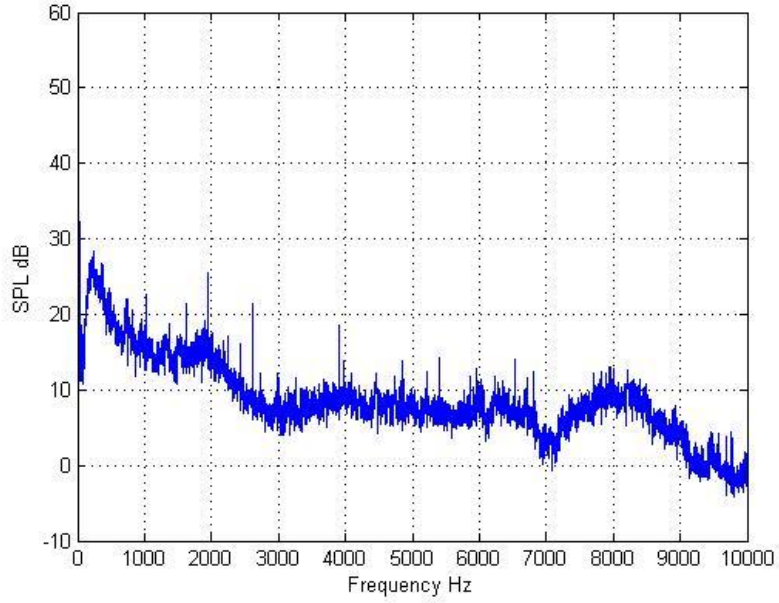

FIG. 5.1. Dodecahedron Averaged Sound Power.

5.4.4 Sound Field Modeling

A reverberation chamber with the dimension 5.7 m x 4.3 m x 2.5 m is modeled using the formulations derived in 5.4.2. The wave number k_N in Eq. (5.41) becomes complex because of the absorption from the boundaries of the chamber. The imaginary part of the wave number can be computed from the boundary impedances of the chamber according to Eq. (5.23). The boundary impedances of the reverberation chamber walls are similar, very large, and related to the absorption coefficients through the simple relationship:

$$\begin{aligned} \alpha_x &\approx 8/\xi_x \,, \\ \alpha_y &\approx 8/\xi_y \,, \\ \alpha_z &\approx 8/\xi_z \,. \end{aligned} \tag{5. 43}$$

Because of their similarity, the absorption coefficient may be considered uniform on these surfaces. An average absorption coefficient can be used to calculate the loss inside the chamber, and through the reverberation time T_{60} and Sabine's equation:

$$\langle \alpha \rangle_s = \frac{0.161V}{AT_{60}}, \tag{5. 44}$$

where A is the total surface area of the walls. The pressure field can be derived from Eq. (5.41), (5.42) and (5.23):

$$\hat{p} = -4\pi\hat{A}\sum_{N=0}^{\infty} \frac{\psi_N(\vec{r}_0)}{\left\{k^2 - \left[k_N + j\frac{k\alpha}{8k_N V}\left(\frac{\varepsilon_{n_x}}{l_x} + \frac{\varepsilon_{n_y}}{l_y} + \frac{\varepsilon_{n_z}}{l_z}\right)\right]^2\right\} V\Lambda_N} \psi_N(\vec{r}); \tag{5. 45}$$

$$\varepsilon_i = \begin{cases} 1 & k_{i,R} = 0 \\ 2 & k_{i,R} \neq 0 \end{cases}$$

The modulus of the monopole amplitude $\left|\hat{A}\right|$ can be directly calculated from taking the square root of the power spectra discussed in Sec. 5.4.3. Essentially any complete set of eigenfunctions can be chosen for the expansion. However, the eigenfunctions derived in Eq. (5.29) have a fast convergence because the reverberation chamber boundaries are close to being rigid. The velocity vector field $\hat{\vec{v}}$ can be derived from Euler's equation:

$$\hat{\vec{v}} = -j\frac{4\pi\hat{A}}{\omega\rho_0}\sum_{N=0}^{\infty}\frac{\psi_N(\vec{r}_0)}{\left\{k^2-\left[k_N+j\frac{k\alpha}{8k_N V}\left(\frac{\varepsilon_{n_x}}{l_x}+\frac{\varepsilon_{n_y}}{l_y}+\frac{\varepsilon_{n_z}}{l_z}\right)\right]^2\right\}V\Lambda}\nabla\psi_N(\vec{r});$$

(5. 46)

$$\varepsilon_i=\begin{cases}1 & k_{i,R}=0\\ 2 & k_{i,R}\neq 0\end{cases}$$

The time-averaged energy density is the summation of the time-averaged potential energy density and time-averaged kinetic energy density:

$$\begin{aligned}
<w(\vec{r})>_t &= <w_p(\vec{r})>_t + <w_k(\vec{r})>_t \\
&= \frac{1}{4\rho_0 c^2}|\hat{p}(\vec{r})|^2 + \frac{1}{4\rho_0\omega^2}\nabla\hat{p}(\vec{r})\cdot\nabla\hat{p}(\vec{r}) \\
&= \frac{4\pi^2|\hat{A}|^2}{\rho_0 c^2}\left\{\sum_{N=0}^{\infty}\frac{\psi_N(\vec{r}_0)\psi_N(\vec{r})}{\left\{k^2-\left[k_N+j\frac{k\alpha}{8k_N V}\left(\frac{\varepsilon_{n_x}}{l_x}+\frac{\varepsilon_{n_y}}{l_y}+\frac{\varepsilon_{n_z}}{l_z}\right)\right]^2\right\}V\Lambda}\right\}^2 \\
&+\frac{4\pi^2|\hat{A}|^2}{\rho_0\omega^2}\left(\sum_{N=0}^{\infty}\frac{\psi_N(\vec{r}_0)\frac{\partial\psi_N(\vec{r})}{\partial x}}{\left\{k^2-\left[k_N+j\frac{k\alpha}{8k_N V}\left(\frac{\varepsilon_{n_x}}{l_x}+\frac{\varepsilon_{n_y}}{l_y}+\frac{\varepsilon_{n_z}}{l_z}\right)\right]^2\right\}V\Lambda}\right)^2 \\
&+\frac{4\pi^2|\hat{A}|^2}{\rho_0\omega^2}\left(\sum_{N=0}^{\infty}\frac{\psi_N(\vec{r}_0)\frac{\partial\psi_N(\vec{r})}{\partial y}}{\left\{k^2-\left[k_N+j\frac{k\alpha}{8k_N V}\left(\frac{\varepsilon_{n_x}}{l_x}+\frac{\varepsilon_{n_y}}{l_y}+\frac{\varepsilon_{n_z}}{l_z}\right)\right]^2\right\}V\Lambda}\right)^2 \\
&+\frac{4\pi^2|\hat{A}|^2}{\rho_0\omega^2}\left(\sum_{N=0}^{\infty}\frac{\psi_N(\vec{r}_0)\frac{\partial\psi_N(\vec{r})}{\partial z}}{\left\{k^2-\left[k_N+j\frac{k\alpha}{8k_N V}\left(\frac{\varepsilon_{n_x}}{l_x}+\frac{\varepsilon_{n_y}}{l_y}+\frac{\varepsilon_{n_z}}{l_z}\right)\right]^2\right\}V\Lambda}\right)^2
\end{aligned}$$

(5. 47)

For the reverberation chamber, the set of eigenfunctions derived under rigid boundaries Eq. (5.29) is preferred for fast convergence.

5.4.5 Numerical and experimental comparison

In order to test the validity of the model, a set of measurement was taken inside the reverberation chamber with the dimension 5.7 m x 4.3 m x 2.5 m. An arbitrary lower corner of the chamber was chosen as the coordinate system origin. A dodecahedron source was placed at the location (1.1 m, 1.09 m, 1.72 m) and an energy density sensor was placed at location (2.98 m, 2.37 m, 0.88 m). The reverberation time T30 was first measured as described in Sec. 5.2. and used in place of T60 due to the limitation of the measurable decay range. The average absorption coefficient can be derived from the reverberation time as described in Eq. (5.44).

For the numerical model, a 20 kHz sampling frequency was used. A total number of $l_n f_s/c$ modes were used in each Cartesian direction, where l_n is the length of the chamber in a given direction, f_s is the sampling frequency, and c is the speed of sound. This assures the modal expansion is are fully populated up to $f_s/2$. The estimated sound power spectrum of the dodecahedron source was numerically resampled to the correct sampling frequency f_s. The modulus of the pressure amplitude of the source was derived by taking the square root of the spectrum and incorporated into Eq. (5.45) for the pressure field model.

The pressure field at location (2.98 m, 2.37 m, 0.88 m) is measured using an EASERA system with the energy density sensor, which includes three pairs of phase matched microphones with a pair of microphones aligned along each Cartesian coordinate. A swept sine signal with 48000 Hz sampling rate and 5.46 s length was fed into the an amplifier to drive the source. The length of the signal was chosen so that the pressure field could reach a steady state response.

The impulse responses measured by the six microphones from the energy density probe could be transferred into the frequency domain through the Fourier Transform. The resulting frequency response functions were averaged in order to calculate the average pressure response at the center of the energy density probe. The gradient of the pressure field could also be calculated by subtracting the frequency responses from the pair of microphones along any axis and dividing the subtraction by the distance between the pair of microphones. Figure 5.2 shows the comparison of the modeled pressure and measured pressure at location (2.98 m, 2.37 m, 0.88 m).

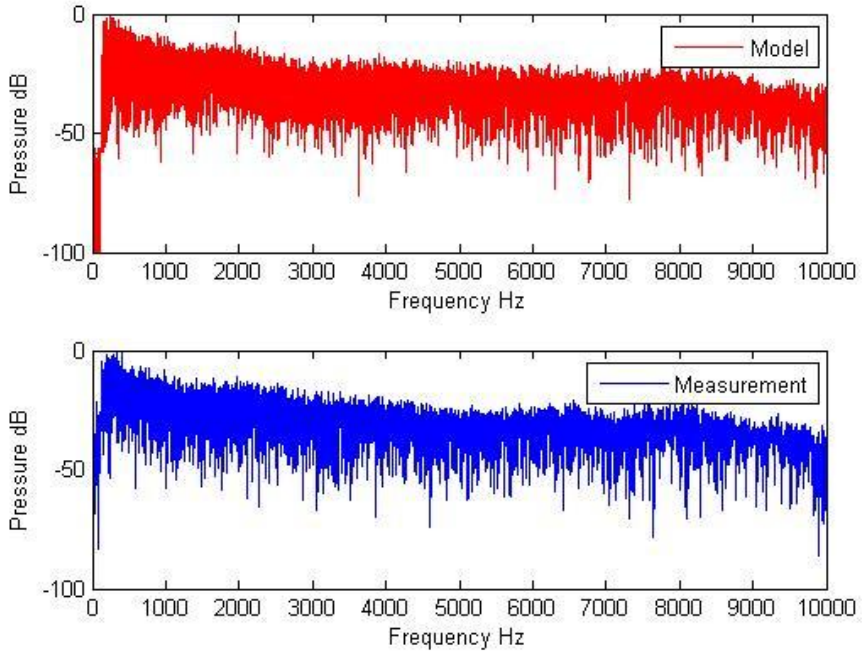

FIG. 5.2. Measured Pressure and modeled pressure frequency responses comparison.

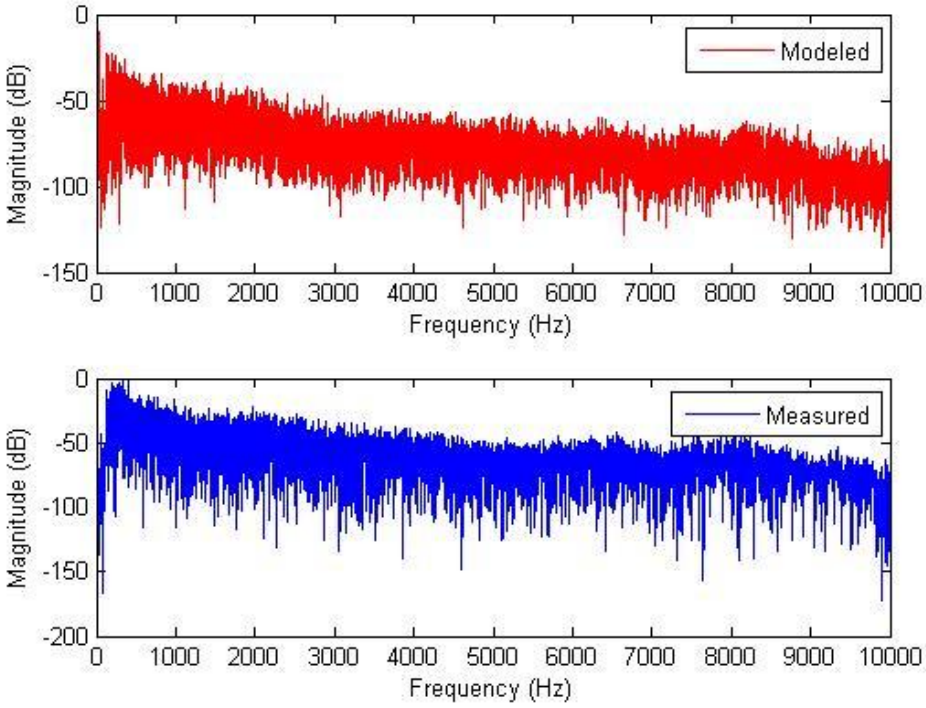

FIG. 5.3. Measured ED and modeled ED frequency responses comparison.

The modeled data and experimental measurements show very similar results. Several factors contribute to the discrepancies. First, the dodecahedron source was not omnidirectional at all frequencies [5]. The source becomes more directional as the frequency increases. Second, some discrepancies may have resulted from the inexact measurement of the source and probe. A third factor is the breakdown of the theoretical model under higher absorptive boundary conditions. From Table 5.1, it can be seen that above 8 kHz, the reverberation time drops down to 1 second. This is associated with an absorption coefficient around .10 for the boundaries and air. When the absorption coefficient is relatively high, the last term in the denominator of Eq. (5.45) is

dependent on the integration of the cross terms of the eigenfunctions [6]. This will result in a slightly larger denominator in the equation (5.45).

5.5 Three dimensional sound field equalization

Direct invertion of the point pressure in a three dimensional field will introduce a series of problems. Due to the complexity of a reverberant field, the immense number of poles and zeros of the inverse filter will result in an impractically long length for the equalization filter [7]. Ringing effects will be introduced from the equalization. A third octave band smoothing is preferred under this context to shorten the original pressure or energy density impulse response in the time domain. The smoothed inverse filter can be modeled with smaller amount of poles and zeros.

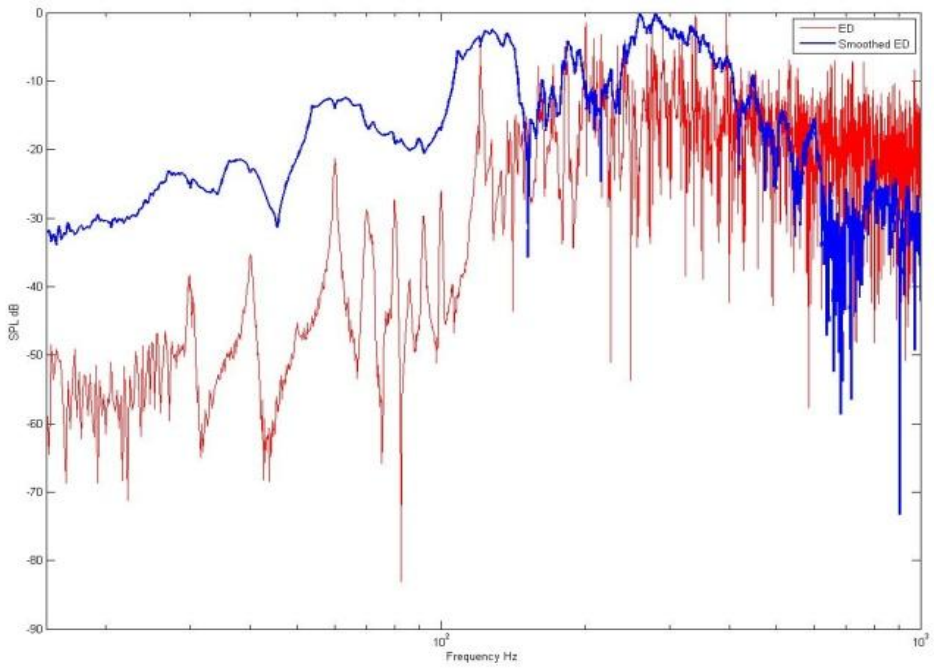

FIG. 5.4. Third octave band smoothing of the energy density spectrum.

As shown in FIG 5.4, third octave band smoothing was used on the energy density measurement to produce a contour of the measurement energy density.

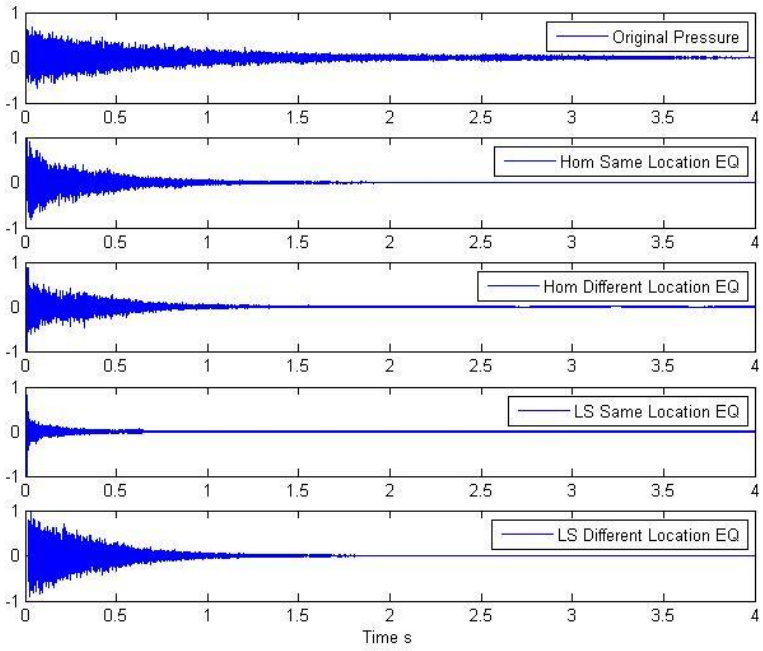

FIG. 5.5. Comparison of the energy density equalization schemes.

FIG 5.5 shows the equalization results using different equalization methods described in the previous chapters. The first diagram shows the original pressure field without any equalization. The second diagram shows the homogeneous equalization at the same location of the pressure measurement. Since this equalization is performed in the frequency domain, the linear convolution in the time domain does not generate a dry enough deconvolution. The equalization at a different location shown in the third diagram gives roughly the same result. As shown in the previous chapters, the least-squares method gives the best deconvolution results in the time domain due to the algorithm that minimizes the error between the deconvolution result to an ideal single impulse. At a different equalization location, this method gives a less satisfying result because of the spatial dependence of the inverse equalization filter.

When the complex smoothing is applied on the energy density equalization, similar approach can be applied.

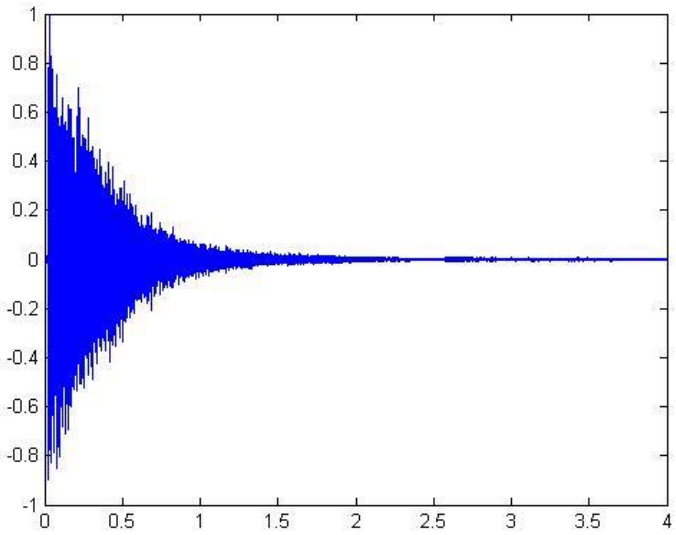

FIG. 5.6. Energy density equalization.

References

[1] M. R. Schroeder, "New Method of Measuring Reverberation Time," J. Acoust. Soc. Am., Vol 37, Issue 6, June 1965, (1187-1188).

[2] ISO 354:2003. Acoustics-Measurement of sound absorption in a reverberation room. (International Organization for Standardization, Geneva).

[3] A.D. Pierce, *Acoustic: An Introduction to Its Physical Principles and Applications* (Acoustical Society of America, New York, 1989).

[4] H. Kuttruff, *Room Acoustics* (Spon Press, London, 2000).

[5] Timothy W. Leishman, Sarah Rollins and Heather M. Smith, "An experimental evaluation of regular polyhedron loudspeakers as omnidirectional source of sound," J. Acoust. Soc. Am., Vol 120, NO. 3, September 2006, (1411-1422).

[6] Phillip M. Morse, K. Uno Ingard, *Theoretical Acoustics*, (Princeton University Press).

[7] Ahfir Maamar, Izzet Kale and Berkani Daoud, "Equalization based on iterative simple complex smoothing of acoustic impulse responses", ICASSP 2006 Proceedings, IEEE, (109-112)

Chapter 6

Conclusions

This dissertation has presented a theoretical and experimental exploration of equalization schemes for loudspeakers and enclosed sound fields. It has focused on both one-dimensional and three-dimensional sound fields. It included methods of modeling simple sound systems in these environments, including a finite-impedance source and a physical field exposed to different boundary conditions. A new method of equalization based on energy density was introduced to achieve improved global equalization results. A method for quantifying the global efficiency of equalization schemes was also introduced and demonstrated.

The dissertation introduced a new method to measure source impedance. It utilizes only a simple impedance-tube measurement to determine the loudspeaker enclosure impedance. The practicality of this in situ process shows significant benefits because it derives the actual impedance behind the loudspeaker cone from a single measurement in front of the cone. The necessity of physical disassembly of the loudspeaker enclosure in order to measure the enclosure impedance is thus eliminated. The accuracy of the enclosure impedance measurement is also improved because the circuitous paths through and around the driver assembly within the enclosure are fully represented. The simple measurement with a one-dimensional impedance tube further removes the need of an anechoic chamber. The method enhances the loudspeaker cabinet model from current standards, which typically use only basic lumped-element approaches. It has shown a greater degree of accuracy and can be utilized in most applications.

Yet, further research is needed to produce theoretical models that more accurately model loudspeaker enclosures with drivers present and in operation.

The one-dimensional pressure fields for a loudspeaker on the end of a tube, a loudspeaker on the side of a tube, and the three-dimensional pressure field for single point-source were theoretically modeled and investigated. Experimental measurements were found to substantiate the models. For the one-dimensional fields, both an equivalent circuit approach and an analytical approach based on differential equations were used in the modeling. Consistent results were generated in both cases. The measured loudspeaker enclosure impedance was incorporated into the models to better match actual system conditions. For the three-dimensional field, an eigenfunction expansion was used for modeling. A method of representing the absorption in an experimental reverberation chamber field was explored. The spectrum of the field pressure due to a point source was modeled and found to be similar to that measured at the same location.

Equalization methods based on energy density were compared to traditional single-point pressure equalization methods. Standard inversion algorithms, such as the homomorphic inversion, least-squares inversion, and complex smoothing were used to derive the equalization filters. That based on energy density gave more spatially uniform equalization results, greatly reducing the number of samples required to achieve a desired equalization result over a defined listening area.

A figure of merit called the global listening area equalization coefficient (GLAEC) was introduced to evaluate the spatial and spectral uniformity of the equalized fields. It showed a certain degree of consistency when evaluating the uniformity of the fields but it did not weigh the spatial uniformity and the spectral uniformity equally because it first calculated the spatially

averaged squared pressure after equalization then performed the standard deviation on that spatially averaged squared pressure.

As with all research, new ideas, concepts, and suggestions have arisen for future exploration in the areas of modeling and equalization of enclosed sound fields. Two suggestions merit mention here. First, a more accurate theoretical model for the loudspeaker enclosure impedance is still needed. Whether the impedance can be adequately represented by judiciously chosen lumped elements still remains in question. Second, as energy density is not uniform for one-dimensional fields when a loudspeaker is on the side of a tube, or in three-dimensional fields, other physical quantities (or combinations of quantities) that are more spatially uniform are desired for equalization filter design. Additional exploration of energy-based or other sound field quantities for this purpose is encouraged.

Appendix: Derivation of the Thevenin's equivalent circuit

Given the circuit in Fig. A.1, we wish to obtain the Thevenin equivalent circuit.

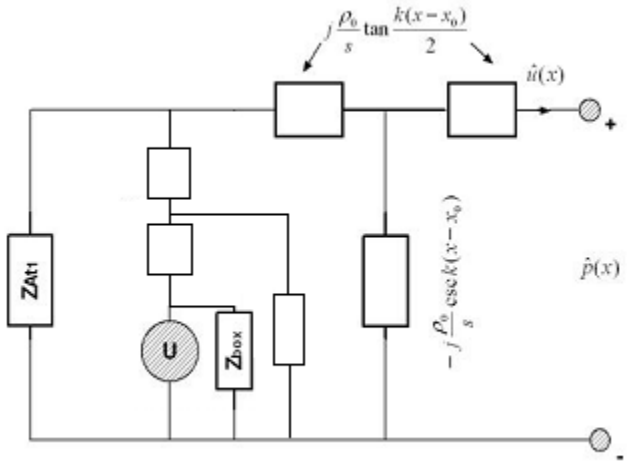

FIG. A.1. Equivalent circuit to the left side of the loudspeaker.

To begin with, Z_{ATH} is the impedance of this circuit with the volume velocity source replaced by an open circuit. The impedance blocks can be combined in six steps:

$$Z_{A1} = \frac{j\rho_0 c}{S}\tan(kl_s/2) + Z_{AN} \qquad \textbf{(A. 1)}$$

$$Z_{A2} = \frac{Z_{A1}\dfrac{-j\rho_0 c}{S}\csc(kl_s)}{\dfrac{-j\rho_0 c}{S}\csc(kl_s) + Z_{A1}} \qquad \textbf{(A. 2)}$$

$$Z_3 = Z_2 + \frac{j\rho_0 c}{S}\tan(kl_s/2) \qquad \textbf{(A. 3)}$$

$$Z_{A4} = \frac{Z_{A3}Z_{AT1}}{Z_{Z3} + Z_{AT1}} + \frac{j\rho_0 c}{S}\tan[k(x-x_0)/2] \qquad \textbf{(A. 4)}$$

$$Z_{A4} = \frac{Z_{A3} Z_{AT1}}{Z_{A3} + Z_{AT1}} + \frac{j\rho_0 c}{S} \tan[k(x - x_0)/2] \quad \textbf{(A. 5)}$$

$$Z_{A5} = \frac{-Z_{A4} \frac{j\rho_0 c}{S} \csc[k(x - x_0)]}{\frac{-j\rho_0 c}{S} \csc[k(x - x_0)] + Z_{A4}} \quad \textbf{(A. 6)}$$

$$Z_{th} = Z_{A5} + \frac{j\rho_0 c}{S} \tan[k(x - x_0)/2] \quad \textbf{(A. 7)}$$

From Thevenin's Theorem, $\hat{p}_{th}$ is the open circuit potential. The impedances can be grouped first:

$$Z_{A6} = \frac{j\rho_0 c}{S} \tan[k(x - x_0)/2] - \frac{j\rho_0 c}{S} \csc[k(x - x_0)] \quad \textbf{(A. 8)}$$

$$Z_{A7} = \frac{Z_{A6} Z_{AT1}}{Z_{A6} + Z_{AT1}} \quad \textbf{(A. 9)}$$

$$Z_{A8} = Z_{A7} + \frac{j\rho_0 c}{S} \tan(kl_s/2) \quad \textbf{(A. 10)}$$

$$Z_{A9} = \frac{-Z_{A8} \frac{j\rho_0 c}{S} \csc(kl_s)}{\frac{-j\rho_0 c}{S} \csc(kl_s) + Z_{A8}} \quad \textbf{(A. 11)}$$

$$Z_{A10} = Z_{A9} + \frac{j\rho_0 c}{S} \tan(kl_s/2) \quad \textbf{(A. 12)}$$

By using the current divider rule, the open circuit potential can be found in four steps:

$$\hat{U}_2 = \frac{\hat{U} Z_{AN}}{Z_{AN} + Z_{A10}} \quad \textbf{(A. 13)}$$

$$\hat{U}_3 = \frac{\hat{U}_2 [\frac{-j\rho_0 c}{S} \csc(kl_s)]}{Z_{A8} - \frac{j\rho_0 c}{S} \csc(kl_s)} \quad \textbf{(A. 14)}$$

$$\hat{U}_4 = \frac{\hat{U}_3 Z_{AT1}}{Z_{AT1} + Z_{A6}} \quad \textbf{(A. 15)}$$

$$\hat{p}_{th} = -\hat{U}_4 \frac{j\rho_0 c}{S} \csc[k(x - x_0)] \quad \textbf{(A. 16)}$$